

The Pennsylvania State University

The Graduate School

College of Engineering

**DEVELOPMENT OF CONTROL ORIENTED ELECTRICAL
AND THERMAL MODELS OF AN ELECTRIC TRANSIT BUS
BATTERY SYSTEM**

A Thesis in

Mechanical Engineering

by

Harshad S. Kunte

© 2014 Harshad S. Kunte

Submitted in Partial Fulfillment

of the Requirements

for the Degree of

Master of Science

August 2014

The thesis of Harshad S. Kunte was reviewed and approved* by the following:

Christopher D. Rahn

Professor of Mechanical Engineering

Thesis Advisor

Hosam Fathy

Assistant Professor of Mechanical Engineering

Karen Thole

Professor of Mechanical Engineering

Head of the Department of Mechanical Engineering

*Signatures are on file in the Graduate School.

Abstract

This thesis presents the insights derived from the empirical characterization, modeling, simulation, control-design, and verification tasks performed in developing energy storage system (ESS) controls for a plug-in electric transit-bus.

The electrical and thermal behavior of a representative electric transit-bus ESS is analyzed through a system-level empirical characterization study.

Experimental data and insights derived from the study are leveraged to develop a control-oriented electrical model of the battery-system, with a provision to incorporate thermal effects. Specifically, it is an equivalent circuit model with parameters dependent on both State of Charge (SOC) and temperature. Then, an Extended Kalman Filter based SOC estimator, implementable on battery monitoring hardware, is developed based on the aforementioned electrical model (albeit, for an isothermal case). Thus, the utility of experimental characterization in developing high-accuracy models and SOC estimators is shown. Further, challenges in migrating an SOC estimator from a simulation environment to a real system, are highlighted through SIL and HIL tests, and mitigation measures are suggested.

Further, the thermal characterization study reveals strong thermal gradients, and sluggish heat-transfer dynamics within the ESS. These are found to be caused by the physical architecture of a typical transit-bus ESS. Thus, it cannot be treated as a single lumped thermal mass as is done for small and mid-size hybrid/electric vehicles. The need, process, and utility, of developing a high-fidelity thermal model for a transit-bus battery-system, is highlighted. This control-oriented model accurately predicts temperature evolution across the battery-system under external electrical and thermal load.

Lastly, the electrical and thermal models developed in the work, are coupled and utility of the coupled models in system-level simulations and trade-off studies, is demonstrated.

Table of Contents

List of Figures	vi
Acknowledgements	x
Chapter 1. Introduction.....	1
Chapter 2. Battery System Equivalent Circuit Model.....	4
2.1 Approach.....	4
2.2 Two Time-Constant Equivalent Circuit Model.....	6
2.3 Test Setup, Plan, and Data.....	8
2.4 Parameter Estimation.....	12
2.5 Variation of Equivalent Circuit Model Parameters.....	16
2.6 Final Electrical Model	20
2.7 Model Validation.....	23
Chapter 3. State of Charge Estimation.....	28
3.1 Approach – An Extended Kalman Filter.....	28
3.2 Extended Kalman Filter as an SOC Estimator.....	29
3.3 Migrating the SOC Estimator to Production Code.....	33
3.4 Simulations and Software-In-Loop Verification.....	37
3.5 Hardware-In-Loop Verification.....	43
Chapter 4. Battery System Thermal Characterization	46
4.1 Battery-System Layout.....	46
4.2 Test Setup & Plan.....	47
4.3 Pack Cycling Test.....	48
4.4 Cool-Down Test.....	53
4.5 Measuring Convective Heat Transfer Coefficient.....	57
Chapter 5. Battery System Thermal Model	61
5.1 Modeling Heat Generation.....	61
5.2 Modeling the Heat-Transfer Dynamics	63
5.3 Simulink Model and Parameter Estimation.....	67
5.4 Model Validation.....	70
Chapter 6. Conclusions	73

Bibliography.....	75
--------------------------	-----------

List of Figures

Figure 1.	An overview of the battery-system under study	1
Figure 2.	Two Time-constant Equivalent Circuit model of the battery system	7
Figure 3.	ESPEC walk-in thermal chamber [L] and AV900 Power Cycling System [R]	8
Figure 4.	A typical HPPC load and voltage response profile used during our testing	9
Figure 5.	Voltage and current data from HPPC test at 40 °C	10
Figure 6.	Comparison between voltage responses of HPPC tests conducted at 20 °C and 40 °C	11
Figure 7.	Voltage and current data from HPPC Test at -20 °C	11
Figure 8.	Open circuit voltage vs. SOC vs. temperature map of the battery system	12
Figure 9.	Simulink model of Two Time-constant Equivalent Circuit model, setup for Parameter Estimation	13
Figure 10.	Results of a sample estimation using test-data at 40 °C and 0.63 SOC	15
Figure 11.	Voltage response from 40°C HPPC Testing at 0.82 SOC	15
Figure 12.	Voltage response from -20°C HPPC testing at 0.78 SOC	16
Figure 13.	Map of series resistance in charge w.r.t. SOC and temperature	17
Figure 14.	Map of series resistance in discharge w.r.t. SOC and temperature	17
Figure 15.	Map of capacitance of RC Branch with slow time-constant w.r.t. SOC and temperature	18
Figure 16.	Map of capacitance of RC Branch with fast time-constant w.r.t. SOC and temperature	18
Figure 17.	Map of resistance of RC branch with slow time-constant w.r.t. SOC and temperature	19
Figure 18.	Map of resistance of RC branch with fast time-constant w.r.t. SOC and temperature	19
Figure 19.	Activation and Concentration Polarization Time Constants w.r.t. SOC at 40 °C	20
Figure 20.	High-level implementation of the TTECM	21
Figure 21.	Dynamic component of the TTEC model	21
Figure 22.	Terminal voltage, and response of the two RC branches to a HPPC pulse at 40 °C	22
Figure 23.	Terminal voltage, and response of the two RC branches to a HPPC pulse at 20 °C	23
Figure 24.	Validation of TTECM with HPPC test data at 40 °C	24
Figure 25.	Validation of TTECM with HPPC test data at 20 °C	24
Figure 26.	Validation of TTECM with HPPC test data at -20 °C	25

Figure 27.	Federal Urban Driving Schedule (FUDES) as a current trace corresponding to a target vehicle application	26
Figure 28.	Validation of the TTECM with FUDES	26
Figure 29.	Overview of the Simulink® implementation of the SOC Estimator	31
Figure 30.	Detailed Implementation showing Time-Update & Measurement Update stages	32
Figure 31.	Implementation of parameter maps through Simulink® Look-Up Table	32
Figure 32.	C code of the Binary Search and Linear Interpolation used by Look-Up Tables	35
Figure 33.	Distinction between SOC estimator's tunable parameters and constants, in the production C code	36
Figure 34.	Simulink® model used to conduct simulation and software-in-loop verification of the SOC estimator	38
Figure 35.	Comparison of actual voltage and SOC with that predicted by the SOC estimator operating as software-in-loop, using FUDES [Actual Initial SOC = 0.80, Initial Guess = 0.75]	39
Figure 36.	Comparison of actual voltage and SOC with that predicted by the SOC Estimator operating as software-in-loop using FUDES [Actual Initial SOC = 0.55, Initial Guess = 0.35]	40
Figure 37.	Comparison of actual voltage and SOC with the SOC estimator operating as software-in-loop using FUDES [Actual Initial SOC = 0.45; Initial Guess = 0.25][Q = 1e-4; R = 0.052]	40
Figure 38.	Comparison of SOC Estimator performance for different values of Q and R [Q = 1e-4 R= 0.052; Q= 1e-3, R=0.12]	41
Figure 39.	Comparison of actual voltage and SOC with that predicted by SOC Estimator operating as Software-in-Loop using HPPC [Actual Initial SOC = 0.8; Initial Guess = 0.6][Q = 1e-6; R=0.009]	42
Figure 40.	Comparison of actual voltage and SOC with that predicted by SOC estimator operating as software-in-loop using HPPC [Actual Initial SOC = 0.8; Initial Guess = 0.2][Q = 1e-3; R=0.12]	42
Figure 41.	SOC estimator performance with digitized voltage and current measurements obtained over a CAN Bus i.e. HIL [Initial SOC Guess = 0.6; Q = 1e-8; R = 0.009]	44
Figure 42.	Comparison of SOC estimator performance for three different sets of Q and R values. Voltage and current measurements obtained in digitized form over a CAN Bus i.e. HIL	44
Figure 43.	Physical layout of the battery-system	47
Figure 44.	Experimental setup	48

Figure 45.	Load Profile used for Thermal Characterization Testing	49
Figure 46.	Spatial distribution of temperature rise between start and end Pack Cycling Test	50
Figure 47.	Internal temperature distribution at start and end of Pack Cycling Test	51
Figure 48.	Temperatures in different regions of the battery-system during Pack Cycling Test	52
Figure 49.	Evolution of heat-sink and cooling-plate region temperatures	53
Figure 50.	Spatial distribution of temperature drop during Cool-Down Test	54
Figure 51.	Temperature distributions at start and end of Cool Down Test	55
Figure 52.	temperatures in different regions during Pack Cool Down	56
Figure 53.	Temperature traces showing delayed on-set of cooling at Cooling-Plate	57
Figure 54.	Coolant temperature at battery pack inlet and outlet during a Pack Cycling Test	58
Figure 55.	Comparison of thermal power generated, extracted, and absorbed during Pack Cycling Test	58
Figure 56.	Heat Transfer Coefficient	60
Figure 57.	Location of heat-sources as concluded from thermal characterization	61
Figure 58.	Simulink implementation of heat-generation model	63
Figure 59.	temperature response of Module Terminal and Cooling Plate during unforced cooling	64
Figure 60.	Lumped-Node Thermal Model of a Single Module	65
Figure 61.	Battery-Pack level thermal model	66
Figure 62.	Overview of the thermal model setup for parameter estimation	67
Figure 63.	Model of heat-exchange between the 4 four regions of cooling-plate, and coolant	68
Figure 64.	Model of heat-exchange to coolant, in an internal flow with constant wall temperature	68
Figure 65.	Model of dynamics between module terminals and cooling-plate regions for each of the four modules	69
Figure 66.	Implementation of the lumped capacitance models for each module	69
Figure 67.	Sample temperature traces and Cost Function from one of the parameter estimation tasks	70
Figure 68.	Comparison of Measured and Simulated temperature Responses During Forced Cool-Down	71
Figure 69.	Comparison of measured and simulated temperature response at Module 3 during Pack Cycling	71

Figure 70.	Comparison of measured and simulated temperature response at Module 1 during Pack Cycling	72
Figure 71.	Unified electrical and thermal model used in full-vehicle simulations, control-design, etc.	73
Figure 72.	voltage and SOC results from a simulated HPPC test on the Unified Model	74
Figure 73.	temperatures of Module 1 and Module 3 from a simulated HPPC test using the Unified Model	74

Acknowledgements

I would like to thank Tim Cleary for his relentless support, encouragement, and enthusiasm, throughout the last year. This thesis is a product of my work at the Larson Institute, under his support, and would have been impossible without it.

I want to extend my thanks to Dr. Chris Rahn for his inputs as my advisor, and for the value addition that his expertise brought to my work. In addition, I want to thank Dr. Hosam Fathy, who has always been supportive and encouraging throughout my two years at Penn State. The faculty at Penn State have taught me invaluable skills required as an engineer, researcher, and professional, which will remain with me for the rest of my career.

A special thanks to Jim Kreibick! His tireless work on the lab's test-setup was the key enabler that allowed me to carry out the work presented in this thesis.

I want to acknowledge the invaluable role my parents have played in nurturing me into the individual I am today. They have backed me up in good times, and bad, and through all important decisions, including this one of coming to Penn State.

Lastly, thank you Karu, for keeping up with my workaholic ways, for the occasional reality-check, and for being there through it all.

Chapter 1. Introduction

This thesis describes the work performed at the Larson Institute, to aid the development of the energy storage system (ESS) of a plug-in electric transit-bus. The transit-bus in question is being developed by a third-party, which is the project's stake-holder. A key building block of the bus' energy storage system is the battery-system that forms the subject of this work.

The battery-system consists of eighty pouch cells of the lithium nano-structured titanate oxide (LTO) chemistry, connected in series. The cells are arranged in eight modules as shown in Figure 1. These are placed inside a metal housing. The battery-system has an on-board processor, sensors, and power-electronics required for battery management and passive balancing. The battery management system currently runs very rudimentary and heuristic algorithms for State of Charge (SOC) estimation and thermal management. The system is also equipped with cooling-plates located on the long edges of the housing. These have internal channels through which 50 percent ethylene glycol with water, can be circulated by the vehicle's on-board pump. Heat energy from the coolant can be extracted by an on-board radiator/chiller.

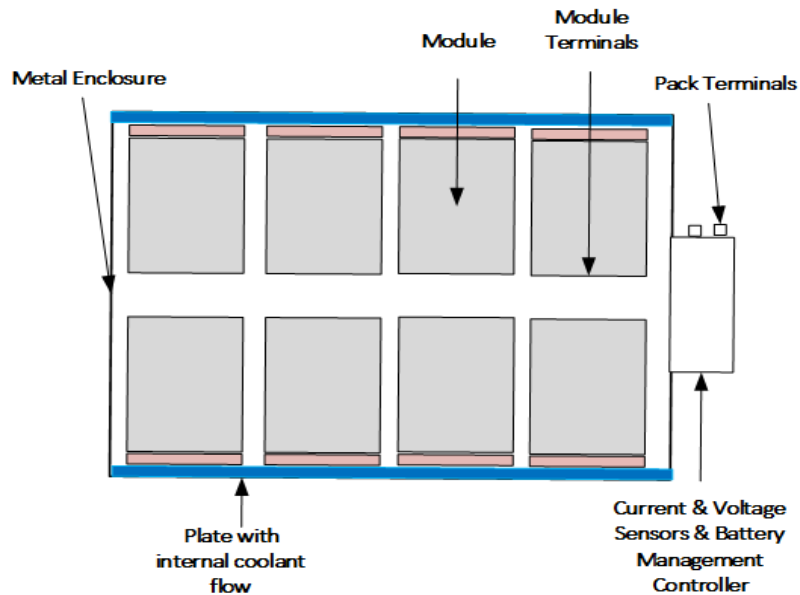


Figure 1. An overview of the battery-system under study

The Lithium nano-structured Titanate chemistry used in this application is unique and relatively new. A single pouch-cell of this type has a 50 Ah nominal capacity. It operates between 1.5 V and 2.8 V with a nominal voltage of 2.3 V. Some key benefits of this chemistry are

a pulse capability of 10C, a cycle-life of greater than 12000 at 2C charge/discharge, and an increased resilience to temperature extremes.

This cell derives its benefits from its nano-structured lithium titanate oxide anode. The anode consists of a nano-titanate spinel structure, to replace graphite. Thus, a solid electrolyte interphase (SEI) layer is not formed at the anode, resulting in reduced impedance to charge-transfer. This results in an increased charge/discharge power capability. Further, the absence of an SEI layer renders the cell more resilient to temperature changes. Unlike graphite, the spinel structure does not swell during charging. Thus, it undergoes lesser mechanical fatigue and has a higher cycle-life. Lastly, due to the absence of graphite, and no SEI formation, these cells have higher thermal stability, and fewer failure modes.

However, these benefits are obtained at the cost of additional weight due to increased density of the anode material. Further, the increased continuous and pulse-power capability results in higher heat-generation rates and rapid increases in cell-temperatures, thus requiring advanced thermal management.

These cells are most suitable in applications with high power and cycle life requirements, yet slightly relaxed volume or packaging constraints. Thus, transit-buses are an ideal application area.

The first key deliverable of this work was to completely characterize the electrical performance of this battery-system, and develop its control-oriented electrical model, to be used by the project stakeholder as part of system-level and full-vehicle simulations.

Chapter 2 starts with a detailed empirical characterization of the electrical properties and of this battery system. It then describes the development of a high-fidelity, control-oriented model of this battery system, with a provision for including thermal dynamics. The chapter concludes with a validation study of this model against experimental data.

Chapter 3 presents the development of an SOC estimator based on the battery model developed in Chapter 2. This was done to meet another project deliverable of implementing an improved SOC estimation algorithm on the battery-system. In addition, it demonstrates the utility of the above electrical model in developing and implementing estimation and control algorithms.

A second key deliverable was to characterize thermal dynamics of the system. Note that the current architecture of battery-system was developed by the project stakeholder, and was beyond the scope or control of this work.

Further, a high-fidelity, control-oriented simulation model of the system's thermal dynamics was required. This was needed to evaluate the system's performance and limits, in a simulation environment, and also as a basis for trade-off studies, and design of thermal control systems.

Chapter 4 presents a detailed empirical characterization of the thermal dynamics across the battery-system.

Chapter 5 leverages the analysis presented in Chapter 4 and prior work in the literature on thermal-models of large format lithium ion batteries, to develop a high-fidelity simulation model of the temperature dynamics across the battery system. This model is coupled with the electrical model to provide unified simulation capability.

Note that this thesis does not present any work on characterization or modeling of individual cells. Instead, it chooses to address system-level modeling, simulation, and control challenges.

Chapter 2. Battery System Equivalent Circuit Model

2.1 Approach

The first deliverable of this work was the development of a high-fidelity electrical model of the battery system described previously. A wide range of practical considerations were made in deciding the best modeling approach.

Specifically, the goal was to develop a system-level battery model that would accurately simulate the battery's response across its entire electrical and thermal operating envelope, including extreme limits of C-rate, State of Charge (SOC), and temperature. Further, the model would have to function as part of a larger, full-vehicle model, and be used in validation of battery management algorithms. To this end, the model needed to be sufficiently simple, executable at least in real-time, on standard desk-top computers, and in standard systems-modeling environments like Simulink®. Keeping in mind the larger objectives of the project, it was important to keep this model tractable, to form a basis for developing estimation and control algorithms that could be deployed on automotive systems.

Lastly, while working with the project's stakeholders, it quickly became clear that battery original equipment manufacturers (OEMs) aggressively protected information about the electrochemical processes and parameters of the batteries, and did not readily share these with customers. Consequently, a generalized modeling approach was required.

Several control-oriented models were considered. Most control-oriented models of different lithium-ion (li-ion) chemistries, used in the literature, fall into one of three general categories.

The Single Particle Model is a simple and widely used approach. It represents the anode and cathode as single particles but does not model the electrolyte/solution phase. This renders it inaccurate at high C rates which are expected in automotive applications, and even more so with the lithium nano-structured titanate battery chemistry used in this work.

The Doyle Fuller Newman (DFN) model developed by Doyle et al. [1] is by far the most accurate, first-principles electrochemistry based model of a li-ion battery. However, there are two key reasons for it being unsuitable in this case. Firstly, it models the Solid Electrolyte Interphase (SEI) layer on the anode of a typical li-ion battery. However, the nano-structured lithium titanate spinel used in the anode of this battery system does not form an SEI layer, as stated earlier. Secondly, it is challenging to simulate the DFN model in real-time, as part of a system-level or full-vehicle simulations.

The third general category of control-oriented models is equivalent-circuits, based on empirical data. The literature contains a variety of different equivalent-circuit configurations used for different Li-ion chemistries. He et al. [2] provide a review of the common equivalent-circuit battery models (ECMs). Each have their benefits and disadvantages, and can be tailored based on the target applications. A typical criticism of ECMs is the need of extensive experimental data. However, extensive experimental data is this work's key strength. Furthermore, ECMs offer the combined benefit of simplicity and accuracy across a wide-operating range, contingent on accuracy of parameter maps. They also have traditionally been the best approach for implementing battery models as part of full-vehicle simulations in Simulink or similar environments. A series of publications in the recent past by Huria et al. [3] [4] and Jackey et al. [5] [6], point to this trend. Hence, the ECM approach was an attractive option.

A survey reveals that ECMs with one or two time-constants and a series resistance, are most common. However a single time-constant cannot capture differences in transient response of the relaxation and pulse load phases, thus reducing fidelity. The literature points to this weakness [3].

Recent work by Huria et al. [6] also discusses a three-time constant ECM with parameters dependent on SOC and temperature, and implemented in Simscape®. The paper demonstrates that as the number of resistor-capacitor (RC) branches in the model increase, the accuracy of simulating the relaxation response, also increases. However, even a three time-constant model significantly complicates the parameter estimation problem because two of the three time-constants are very close together. Further, it increases complexity of downstream applications like SOC estimators and their implementation. The paper by Huria et al. only demonstrates the model development process for a narrow region of the operating envelope and it was infeasible to use it across the entire operating envelope targeted by this work.

Thus, the two-time constant ECM was chosen. It is intermediate in accuracy between the two models discussed above, does not significantly complicate the parameter estimation task, and is sufficiently tractable to use as a basis for developing an SOC estimator.

Initial analysis of the test data indicated a sluggishness in the battery-system's thermal dynamics and response to thermal control-actions. As a result, temperature changes during cycling of the system were very stark. Further, the data quickly revealed noticeable changes in the battery's response even between 20 °C and 25 °C. As a result, this work accounts for variations in two-time constant ECM's parameters w.r.t. SOC and temperature. This chapter describes the model, its development, and validation.

2.2 Two Time-Constant Equivalent Circuit Model

The Two Time-Constant Equivalent Circuit Model (TTECM) is an ideal voltage source, connected to a series resistance and two RC branches.

When the TTECM is cast as a battery model, the ideal voltage source represents the battery's open circuit voltage (V_{oc}). It is typically a function of SOC and temperature. The series resistance (R_o) reproduces the static component i.e. the jump in terminal voltage ($V_{terminal}$) when a battery is subjected to non-zero electrical load. The two RC branches reproduce the dynamic component of the battery's response under load. The two branches typically have time-constants an order of magnitude apart. Different time-constants enable accurate reproduction of different transients seen during pulse load and relaxation, and give the model its name. Note that the TTECM is a third-order model. Specifically, voltages of the two capacitors (U_f and U_s) and the V_{oc} (or SOC) are the three states. The following are the general state and output equations for the TTECM.

$$\dot{U}_f = -\frac{U_f}{R_f C_f} + \frac{I_L}{C_f}$$

$$\dot{U}_s = -\frac{U_s}{R_s C_s} + \frac{I_L}{C_s}$$

$$S\dot{O}C = -\frac{I_L}{Cap}$$

$$V_{terminal} = V_{oc} - U_f - U_s - I_L R_o$$

A Physical Interpretation - Dual Polarization

One approach to interpreting the TTECM is to understand which components of a battery's electrochemical processes are captured by different elements of the model. Ion/Charge transfer dynamics within a li-ion battery are primarily driven by potential and concentration gradients. These manifest as activation and concentration polarizations result in a voltage drop across battery terminals. Saha et al. [7] provide a detailed description of the activation and concentration polarization phenomena in their work on li-ion battery capacity depletion.

Activation Polarization

Activation polarization is the voltage drop due to various factors that retard charge-transfer kinetics within the battery. The most dominant contributor to this polarization is the work required to overcome the impedance to charge-transfer that is presented by the electrode-electrolyte interface [7]. These dynamics are typically very fast and have a significant

magnitude in comparison to concentration polarization. The fast RC branch of the TTECM (i.e. U_f) reproduces this component of the battery's response.

Concentration Polarization

The voltage drop that manifests due to concentration gradient driven mass-transfer dynamics within the cell is referred to as Concentration polarization. As a battery is charged/discharged, an internal potential drop builds up due to a concentration gradient setup within the electrolyte. However, this build up is both gradual, and has a small magnitude in comparison to the Activation polarization [7]. Furthermore, as current is cut-off, diffusion slowly causes this voltage drop to wear-off resulting in the slow "relaxation" response. The slower RC branch of the TTECM (i.e. U_s) reproduces this component of the battery's dynamics.

Both polarization phenomena discussed above are affected by both SOC and temperature of the battery. Thus, in the interest of model fidelity, this work captures variation in TTECM parameters w.r.t. SOC and temperature. Parameters are not constants, but complex functions of SOC, thus rendering the model non-linear. Further, from a pure electrical model standpoint, it is time-variant owing to changes in temperature over time. Figure 2 shows the schematic of the model used in the remainder of the work.

The remainder of this chapter details the test-plan, experiments, data-analysis, model development, and validation of the TTECM of our battery-system.

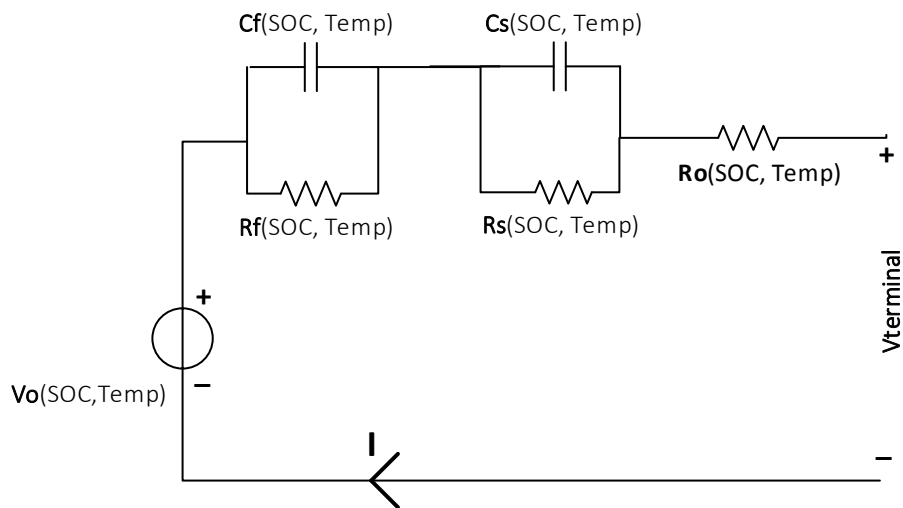


Figure 2. Two Time-constant Equivalent Circuit model of the battery system

2.3 Test Setup, Plan, and Data

Test Setup

Two unique capabilities at BATTERY at the Larson Institute, are the Aerovironment AV900 power cycling system, and the ESPEC walk-in environmental chamber. Specifically, the AV900 has continuous voltage limits of 900 V and current limits of 1000 A, with a peak continuous power of 250 kW [8], and is rarely found in academic research settings. The system can be programmed to exercise battery packs with a variety of load profiles, with a peak frequency of 5 Hz. This uniquely positions our lab to execute tests on the complete battery-system, as opposed to individual cells or small test-batches.

The ESPEC walk-in environmental chamber has a temperature range of -65 °C to 85 °C [9]. It can house, and effectively regulate temperatures of a fully assembled automotive-scale battery system.

Figure 3 shows the lab's power cycling system and thermal chamber. This work leverages these unique capabilities in developing a high-fidelity TTECM of the battery-system.



Figure 3. ESPEC walk-in thermal chamber [L] and AV900 Power Cycling System [R]

The test setup involved the complete automotive battery-system connected to the AV900, and placed inside the thermal chamber. Current and terminal voltage measurements are made using current and voltage transducers placed near the battery pack terminals. The cooling system of

the battery pack is connected across a pump and heat-exchanger to enable heat extraction from the pack in cases of aggressive loading.

Test Plan

From a battery characterization and parameter estimation perspective, the primary test of interest was the Hybrid Pulse Power Characterization (HPPC) test, performed as described by the Idaho National Lab's Battery Test Manual for Plug-In Hybrid Electric Vehicles [10]. In our experiments, a single HPPC load profile consists of a 10 sec, 375 A discharge followed by a 10 sec, 375 A charge. This is followed by a 50 A discharge till the SOC drops by 10 percent, finally followed by an approximately 20 min rest period.

Figure 4 illustrates this load profile with a description of the expected voltage response. The HPPC load profile is ideal from a parameter estimation stand-point. The high C-rate adequately capture effects of the series resistance as well as the faster RC branch. The 50 A discharge region allows characterization of the slower RC branch. The long rest period captures the prolonged relaxation phase that the battery goes through as it returns to its open circuit voltage, after current cut-off. Further, since the characterization is to be done at different temperatures, maintaining a uniform temperature throughout a single test is critical. The long rest period allows sufficient time for the thermal chamber to bring battery-system back to the temperature set-point, before electrical load is applied again.

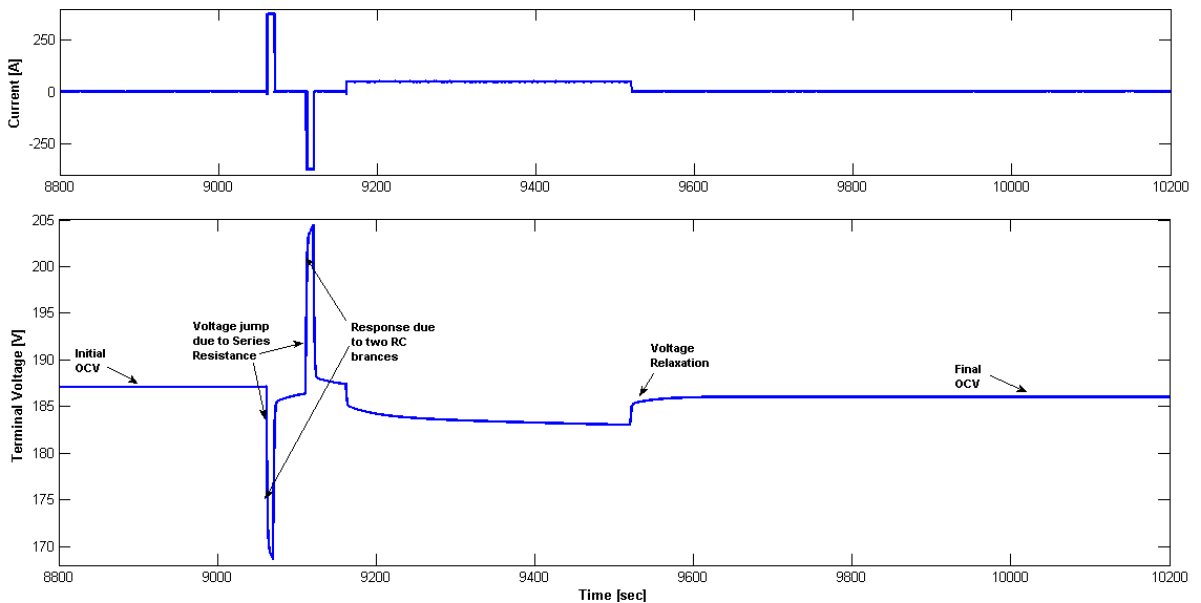


Figure 4. A typical HPPC load and voltage response profile used during our testing

This load profile is repeated at SOC intervals of 10 percent, across the entire operating range of the battery-system. Thus, a complete HPPC test lasts for approximately 20,000 s.

In order to capture the behavior of the battery-system at different temperatures across its operating range, the above described test is conducted at -20 °C, 0 °C, 20 °C and 40 °C. Before testing at any of these temperature set-points, the entire thermal chamber is brought to the required temperature set-point and the pack is allowed to soak in it for approximately 24 hours before commencing the test.

Summary of Test Data

The figure below shows the load profile and voltage response for the HPPC test conducted on the battery system at 40 °C, which is the upper limit of the cell chemistry's recommended operating range. A change in the response characteristics is clearly noticeable at lower SOCs, with voltage drop for 50 A discharge pulses appearing much steeper.

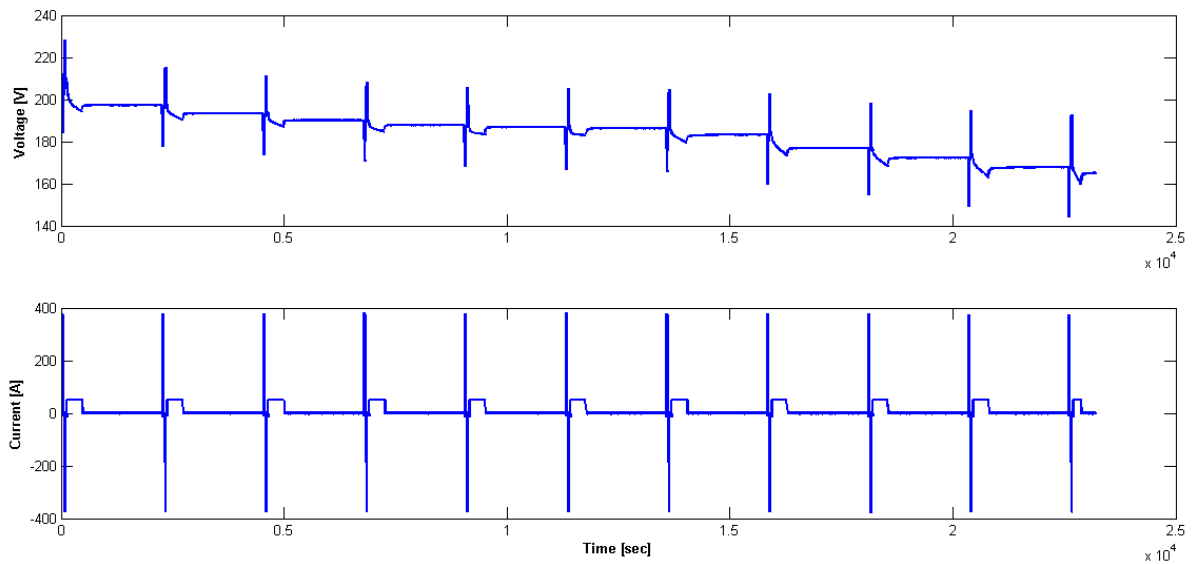


Figure 5. Voltage and current data from HPPC test at 40 °C

The figure below is a comparison of the battery system's voltage response at both 20 °C and 40 °C. It can be seen that voltage response profiles are slightly different with the test at 20 °C showing marginally higher voltage jumps for the same current load. This is typically indicative of slightly higher Series resistance at 20 °C. It is expected that the battery's parameters will not vary significantly between 20 °C and 40 °C, yet a clear difference in the responses is visible. This highlights the need to characterize the system's response across its temperature range.

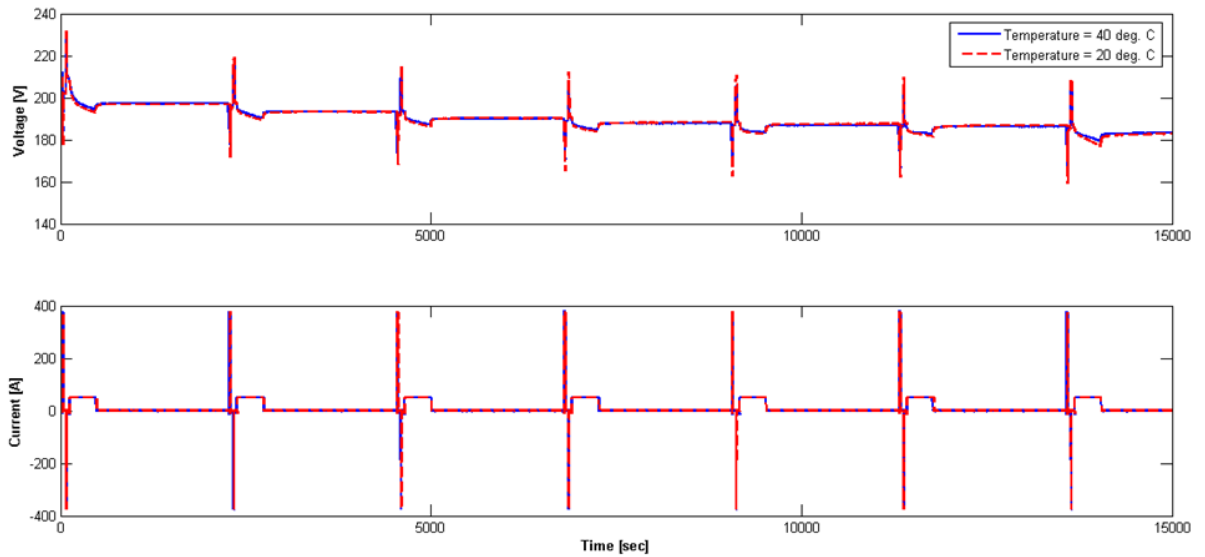


Figure 6. Comparison between voltage responses of HPPC tests conducted at 20 °C and 40 °C

The following figure shows the voltage response for a HPPC test conducted at -20 °C. The response is starkly different from those at higher temperatures, as expected. It is noteworthy that large voltage jumps are seen even for 30 A pulses. This is indicative of a Series resistance that is an order of magnitude higher than at 20 °C and 40 °C. Further, the shape of the response indicates starkly different behavior of the two RC branches of a potential ECM, compared to that at 20 °C and 40 °C.

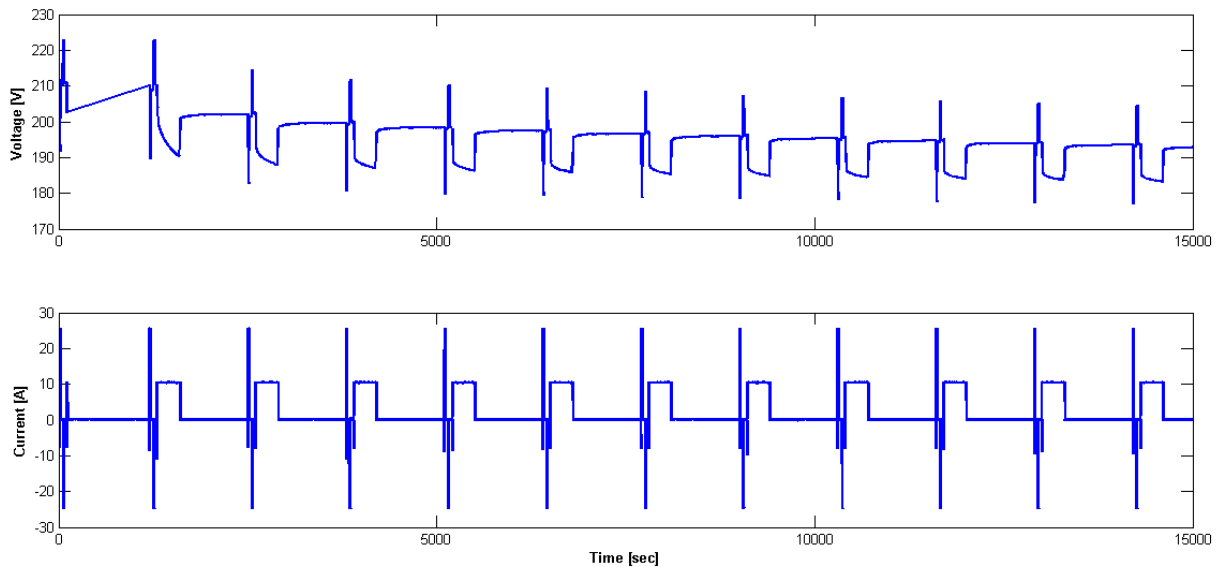


Figure 7. Voltage and current data from HPPC Test at -20 °C

Open Circuit voltage Map

As described above, the HPPC tests allow a long relaxation time between cycles, enabling the battery to return to its true OCV at the current SOC. Further, each HPPC test is started at full charge, and a constant C-rate discharge is applied for a fixed amount of time, between each step. Thus, it is possible to determine the SOC by current counting, and corresponding OCV for each step. This process was used to develop an OCV vs. SOC vs. temperature map for the battery system. This map is shown in Figure 8 below. Note that the sample points have been interpolated using 2-D Cubic Spline interpolation to obtain the continuously differentiable surface plot seen in the map below.

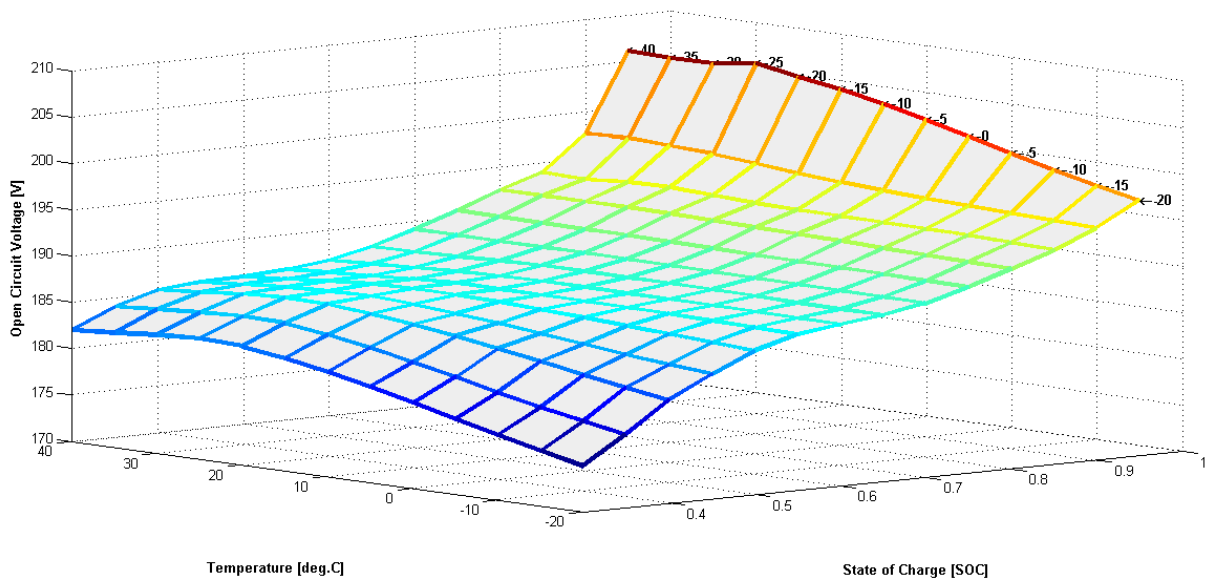


Figure 8. Open circuit voltage vs. SOC vs. temperature map of the battery system

2.4 Parameter Estimation

As described earlier, the TTECM is chosen to model and simulate the dynamics of the complete battery-system. In order to add the required fidelity to the model, the variation of the model's parameters w.r.t. both SOC and temperature is needed to be captured.

This was achieved by estimating the TTECM's parameters at each temperature and SOC set-point at which the above described HPPC tests were conducted. For each set-point, data from a single corresponding HPPC voltage response profile was used. Values estimated using such a profile were assumed to correspond to SOC and temperature at the start of that profile. Forty such data-sets were used to run parameter estimation tasks. The values obtained from these were used to create maps of each parameter. The following section describes the estimation task in detail.

Setup of the Parameter Estimation Problem

The final deliverable of model-development phase of the project was a TTECM of the battery-system, to be plugged in to a full-vehicle Simulink® model for simulations and control design. Thus, even the parameter estimation problem was set-up in Simulink® to maintain consistency. Figure 9 below shows the Simulink® implementation of the TTECM.

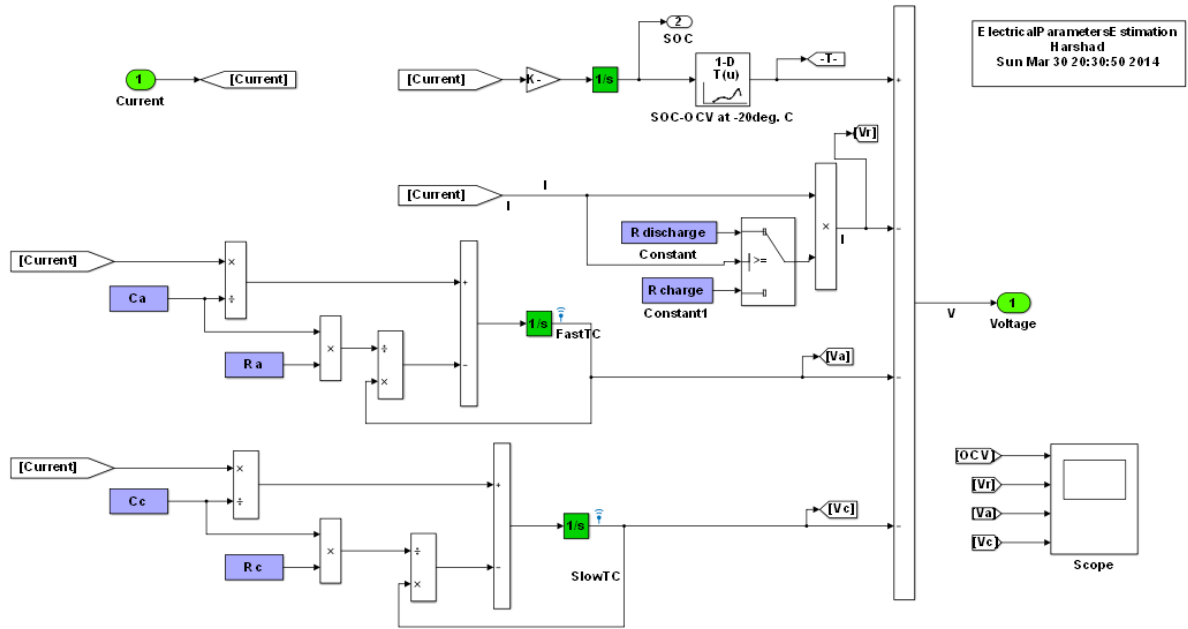


Figure 9. Simulink model of Two Time-constant Equivalent Circuit model, setup for Parameter Estimation

The blocks highlighted in green are current input, terminal voltage output, SOC, and the voltages across capacitors in the two RC branches. The six blocks highlighted in blue are the model parameters to be estimated.

The parameter estimation task is setup as an optimization problem. Specifically, it is a Non-Linear Least-Squares minimization. The Simulink Design Optimization Toolbox is used to automate the process to the extent possible.

The three states are initialized at start of each estimation task. Since each task starts at zero load, the initial value of the voltage trace is used to compute the SOC using the OCV vs. SOC vs. temperature plot shown in Figure 8, voltages of the two capacitors are initialized to zero as is expected after the battery-system is allowed to relax for a long time-period.

To assist the minimization problem, the initial guesses for series resistance in charge/discharge are obtained from the voltage response data by approximating the near-instantaneous voltage

jump when a current pulse is just applied. Initial guesses of parameters for the two RC branches are made by approximating time-constants of different sections of the voltage response, with the knowledge that the two time-constants are at least an order of magnitude apart. Further, constraints of strict positivity, and finiteness, are imposed on each parameter.

The Cost Function to be minimized is the Sum Squared Error between the simulated and measured terminal voltage responses. This is measure of accuracy of the simulated response, and serves as an appropriate objective (or cost) function.

$$Cost = \left(\sum_{k=tstart}^{k=tend} \|V_{meas}(k) - V_{sim}(k)\|_2 \right)$$

The equality constraints or dynamic model associated with this problem, i.e. the TTECMS is non-linear. Thus setting up this parameter estimation problem as a Non-Linear Least Squares optimization problem is the appropriate approach. The following is the final problem formulation:

$$\min_x \left(\sum_{k=tstart}^{k=tend} \|V_{meas}(k, X) - V_{sim}(k, X)\|_2 \right)$$

$$0 < X < \infty$$

$$V_{sim} = TTECM(k, X)$$

An implementation of the Trust-Region approach for solving the constrained non-linear optimization problem, is built into Simulink's *lsqnonlin* function [11]. Recent work in the literature demonstrates that this is a robust approach for solving the constrained minimization problem for parameter estimation of battery ECMs [6] [3].

The optimization process had a Termination Criterion of less than 0.1 percent change in the cost function between iterations.

Figure 10 shows a summary of a sample estimation task for a HPPC profile at 40 °C and 0.63 SOC. The simulated response closely matches the measured response in all parts of the profile, including high C-rate pulses and the slow relaxation phase. A maximum residual of 2.7 percent can be seen, and is attributed primarily to the discretized form of the data from the battery system's voltage transducer. The estimation takes 19 iterations to converge.

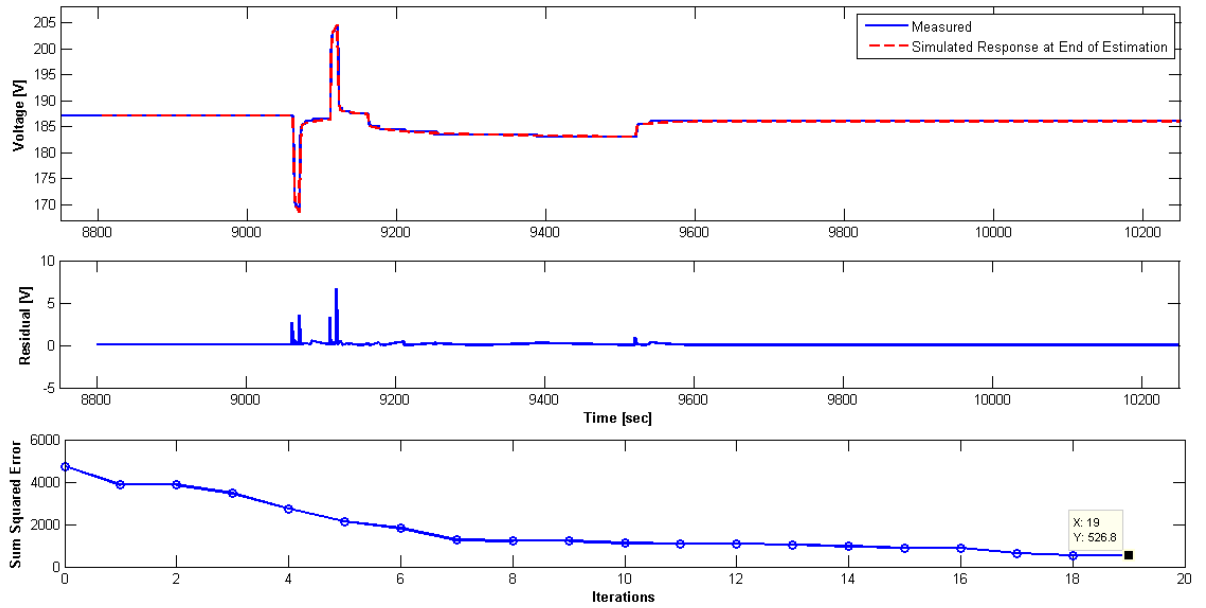


Figure 10. Results of a sample estimation using test-data at 40 °C and 0.63 SOC

A similar estimation problem was solved for each SOC and temperature set-point at which HPPC data was available. Figure 11 below compares the measured and simulated response for a HPPC profile at 40 °C and 0.82 SOC and shows a close match with residuals under 1 percent.

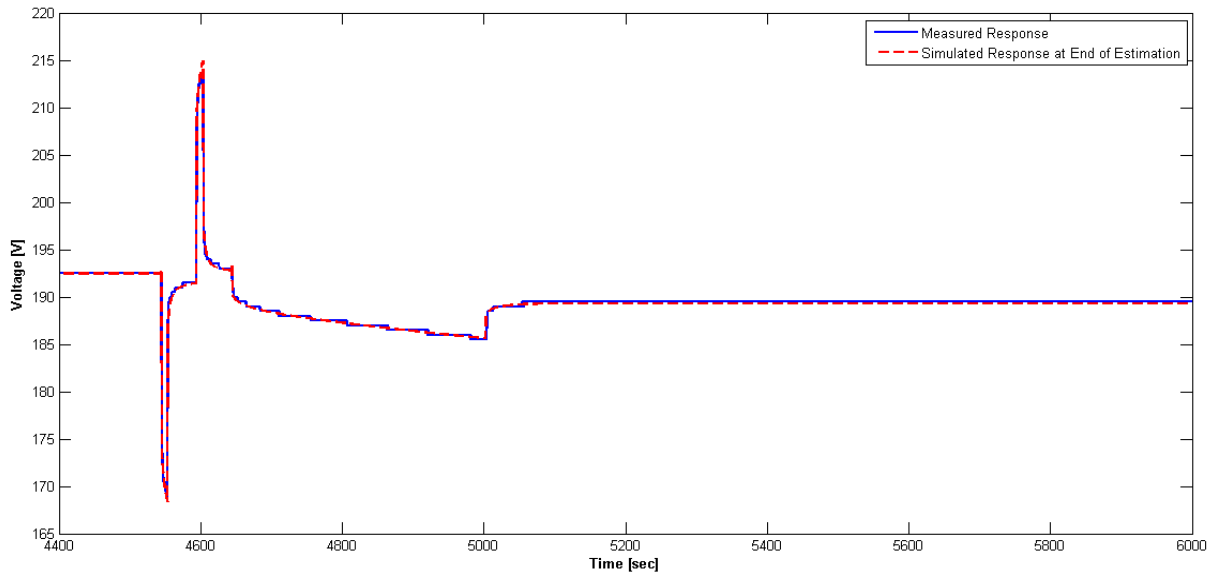


Figure 11. Voltage response from 40°C HPPC Testing at 0.82 SOC

Similarly, Figure 22 shows a comparison of measured and simulated voltage response at -20 °C

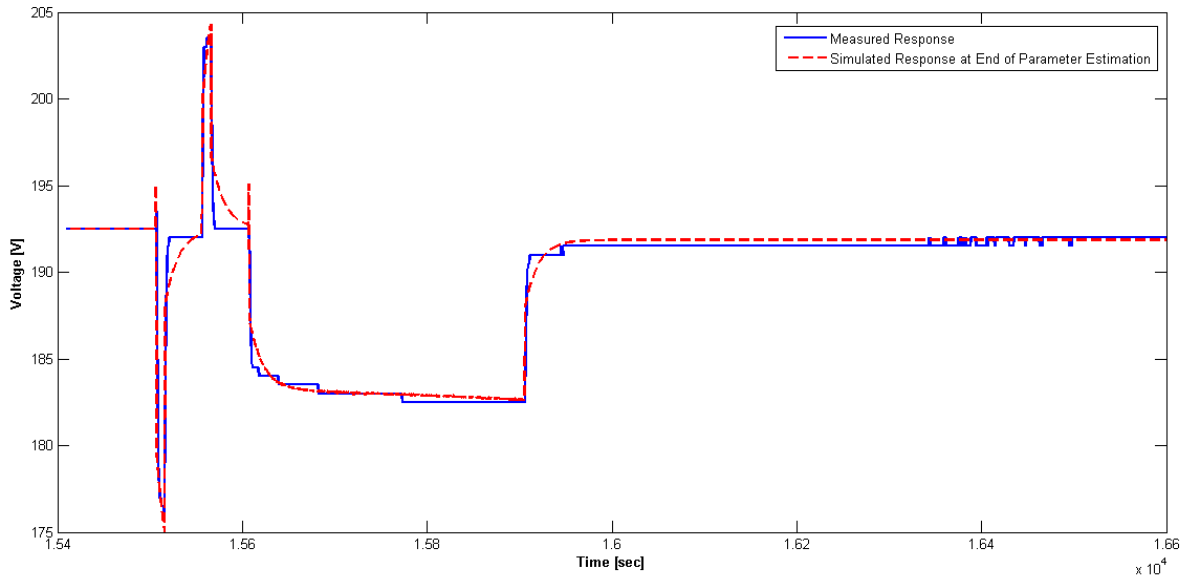


Figure 12. Voltage response from -20°C HPPC testing at 0.78 SOC

2.5 Variation of Equivalent Circuit Model Parameters

The following section summarizes the results of parameter estimation. 2-D Surface Maps of each of the 6 parameters of the TTECM w.r.t. SOC and temperature, are shown in the following. The trends in each parameter, at a fixed temperature, are consistent with results described in several cited articles from the literature [6] [3].

These maps were generated using the results from the parameter estimation as sample-points. A 2-D Cubic Spline interpolation was performed on these sample points to generate continuously differentiable surface plots. Continuous differentiability of the surfaces for each parameter was essential to accurately capturing the nature of parameter variation with SOC and temperature. It was also important from the point of view using this model down-stream for estimation and control design.

Series Resistances

Figure 13 and Figure 14 are maps of Series resistance in Charge and Discharge w.r.t. SOC and temperature. Note the steep increase in the Series resistance with decrease in temperature. Series resistances rise from approximately 0.04Ω at 40°C to approximately 0.7Ω at -20°C . This explains the starkly different characteristics of the HPPC response at -20°C seen in Figure 7.

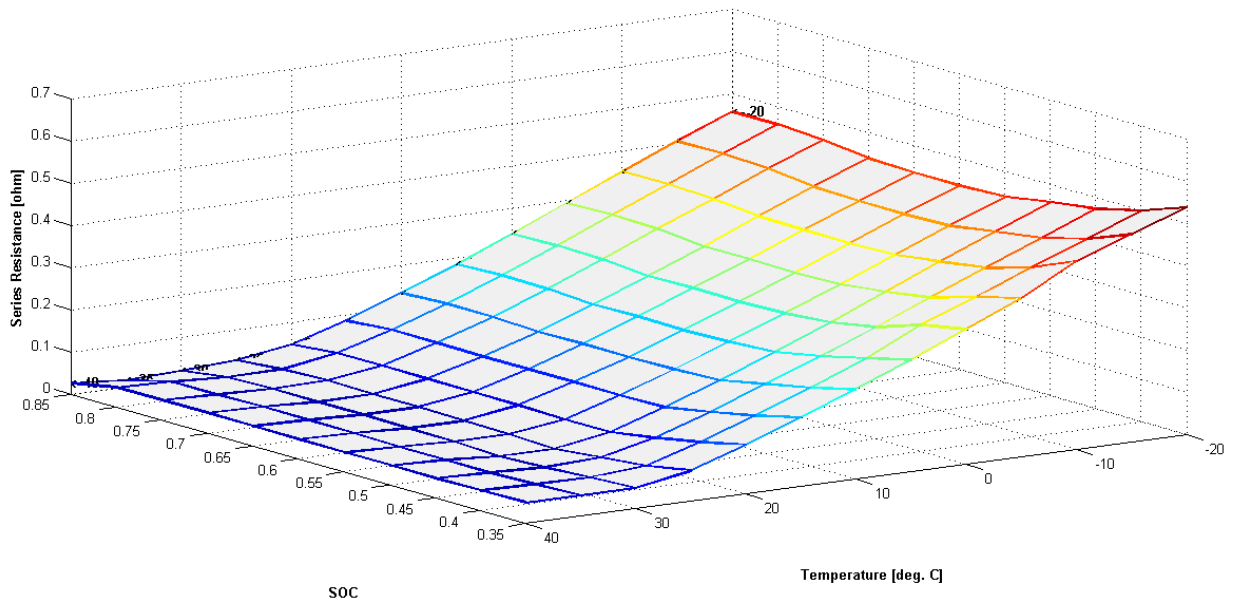


Figure 13. Map of series resistance in charge w.r.t. SOC and temperature

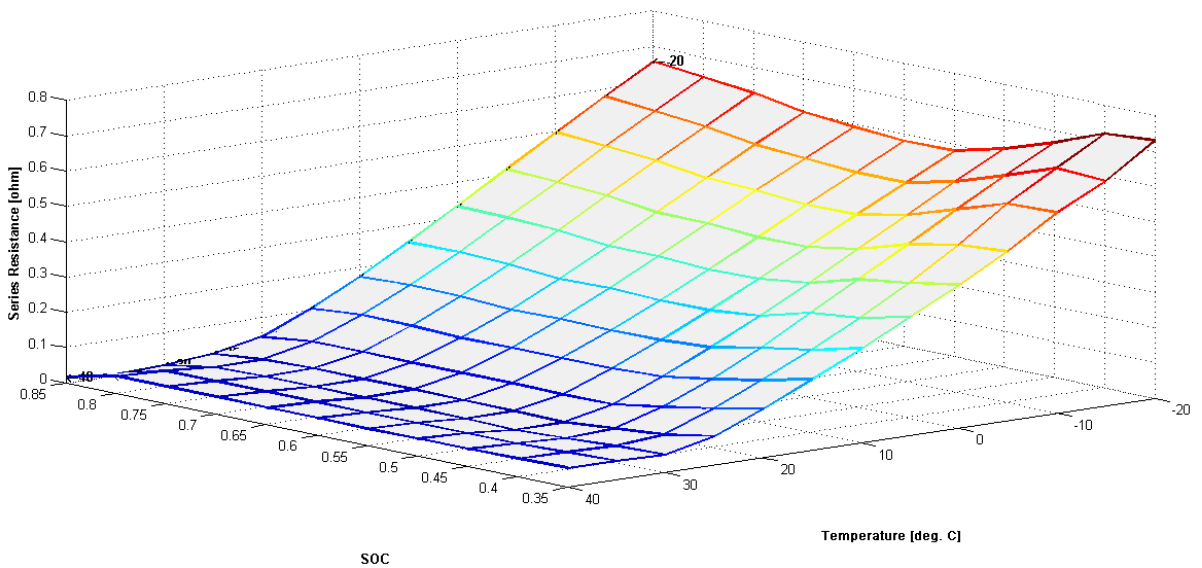


Figure 14. Map of series resistance in discharge w.r.t. SOC and temperature

Capacitance of Two RC Branches

Figure 15 and Figure 16 show maps of capacitance of capacitors in the slow and fast RC branches of the model respectively. Both capacitance maps show a general increase as temperature rises to 40 °C, as expected. Further, the capacitance associated with the slower time-constant is an order of magnitude larger than that associated with the faster time-constant. Lastly, both capacitances show noticeable variations with SOC, and the nature of these variations is temperature dependent.

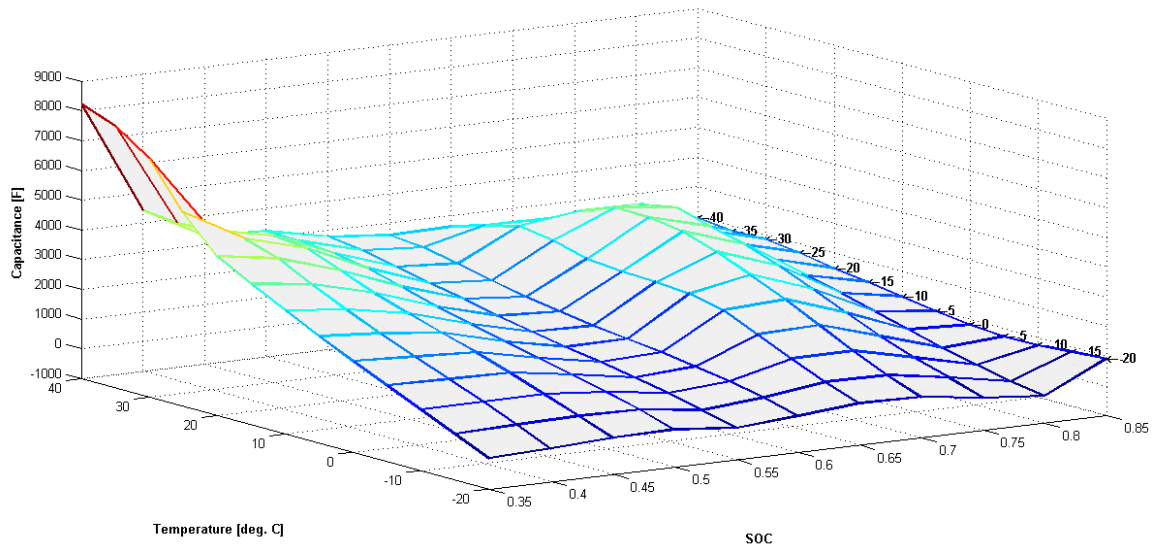


Figure 15. Map of capacitance of RC Branch with slow time-constant w.r.t. SOC and temperature

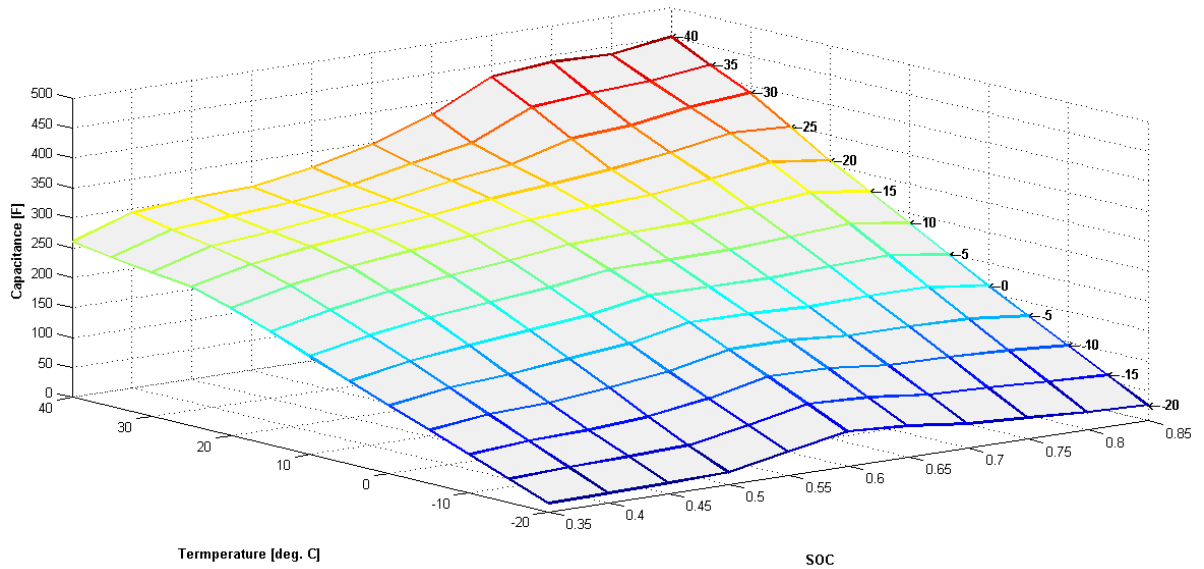


Figure 16. Map of capacitance of RC Branch with fast time-constant w.r.t. SOC and temperature

Resistance of 2 RC Branches

Figure 17 and Figure 18 show maps of resistance of the two RC branches w.r.t. SOC and temperature. These maps show trends very similar to that of the series resistance, showing significant increase in resistance at lower temperatures. The increase is particularly steep below approximately 10 °C.

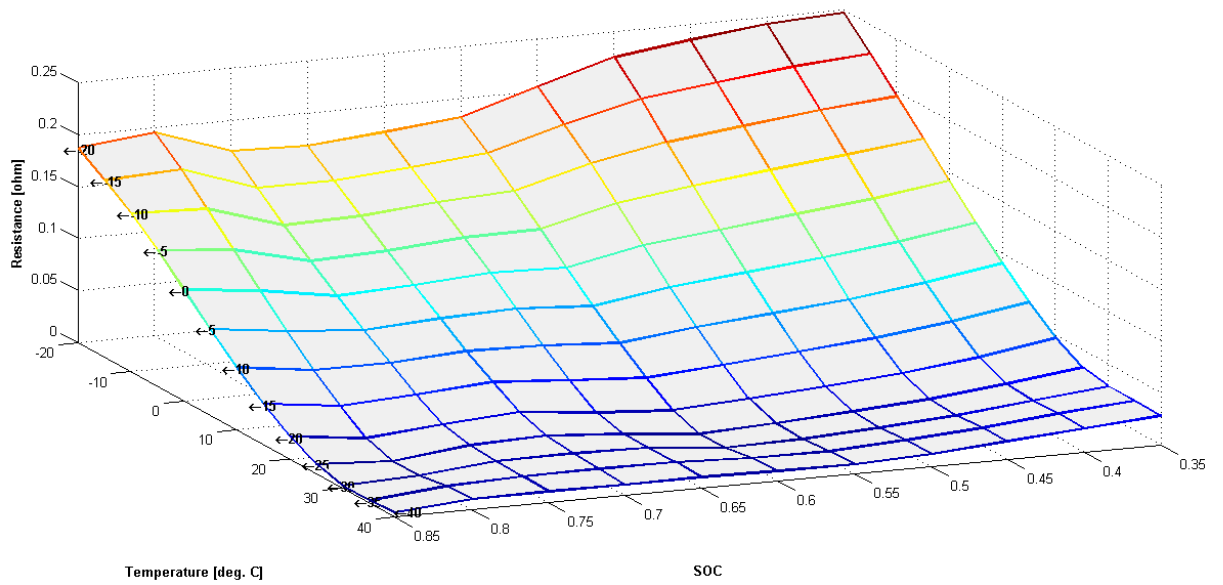


Figure 17. Map of resistance of RC branch with slow time-constant w.r.t. SOC and temperature

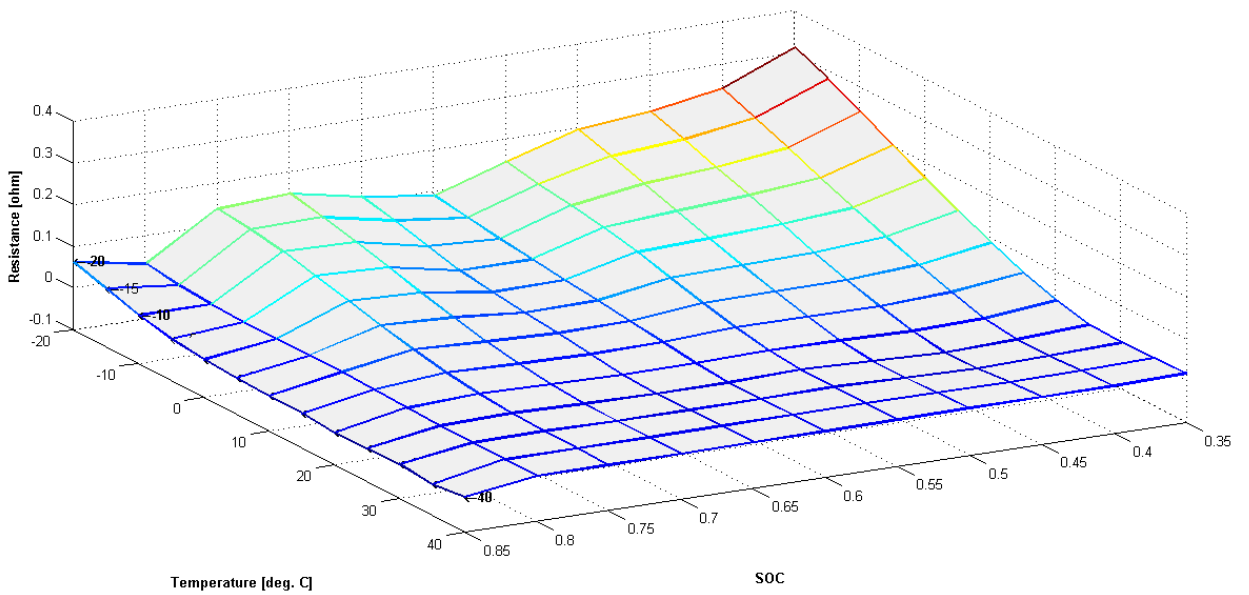


Figure 18. Map of resistance of RC branch with fast time-constant w.r.t. SOC and temperature

Comparison of Time-constant of the Two RC Branches

Figure 19 compares the time-constants of the two RC branches, w.r.t. SOC at 40 °C. The slower time-constant is approximately two orders of magnitude higher than the faster time-constants at lower SOC, and is an order of magnitude higher at slightly higher SOC.

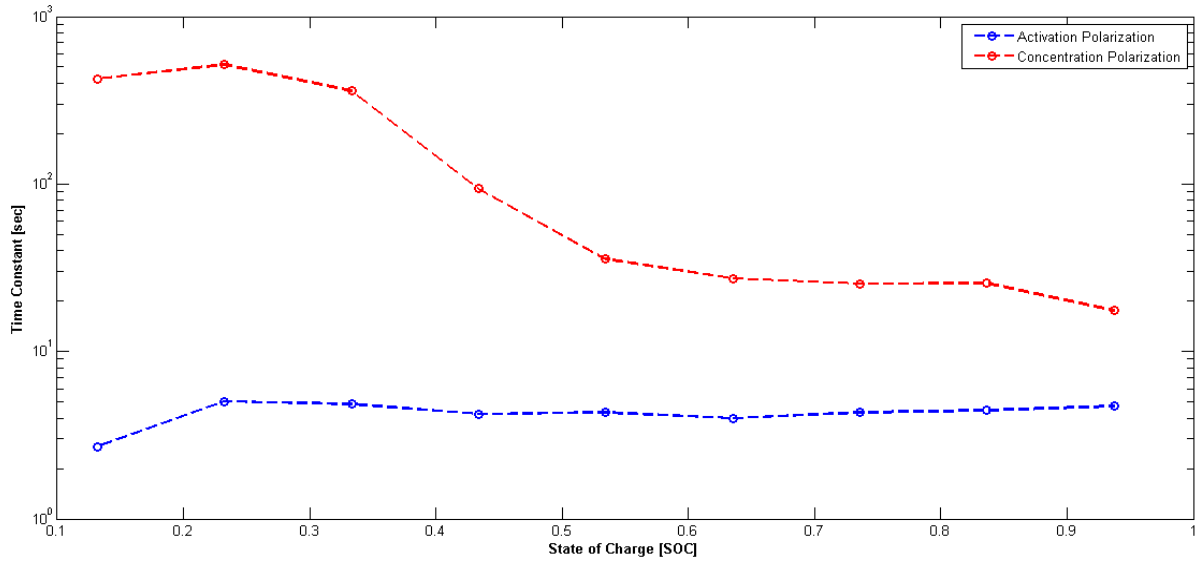


Figure 19. Activation and Concentration Polarization Time Constants w.r.t. SOC at 40 °C

2.6 Final Electrical Model

The following is a snapshot of Simulink implementation of the final TTECM. The three Look-Up Tables seen in Figure 20 are maps of open circuit voltage, series resistance in charge, and Series resistance in Discharge, w.r.t. SOC and temperature. Current and battery-system's bulk temperature are inputs. As illustrated later in this thesis, the temperature signal can be obtained thermal-dynamics model of the battery system. For this phase of the project however, only isothermal simulations were conducted by programmatically forcing a constant temperature. The model outputs terminal voltage, and SOC as outputs, along with values of series resistances.

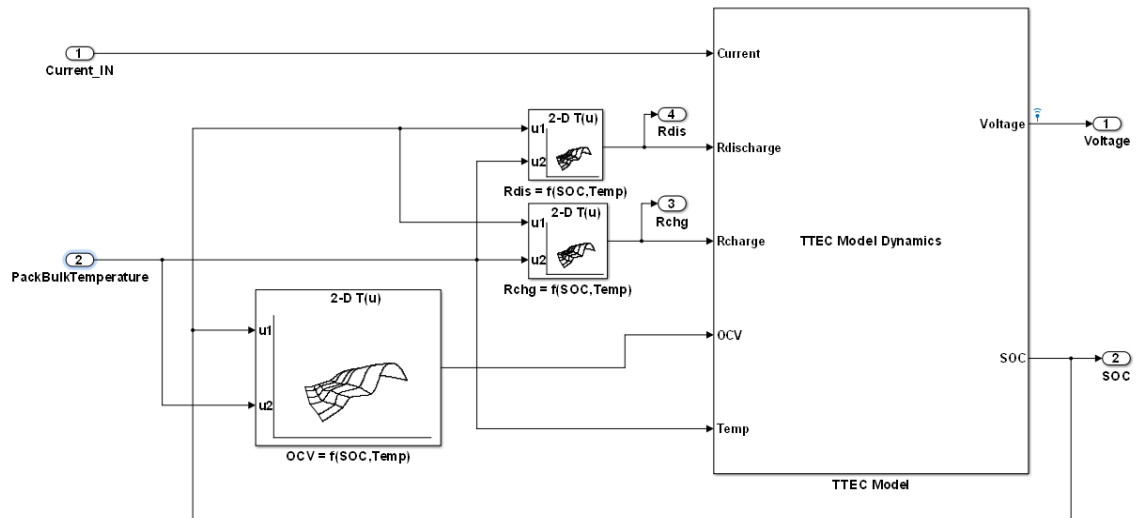


Figure 20. High-level implementation of the TTECM

Figure 21 is a snapshot of implementation of the TTECM's dynamic component, specifically, the two RC branches. It also contains a simple integrator representing SOC. Note that the blocks highlighted in blue are the model's parameter maps implemented as 2-D Look-Up Tables.

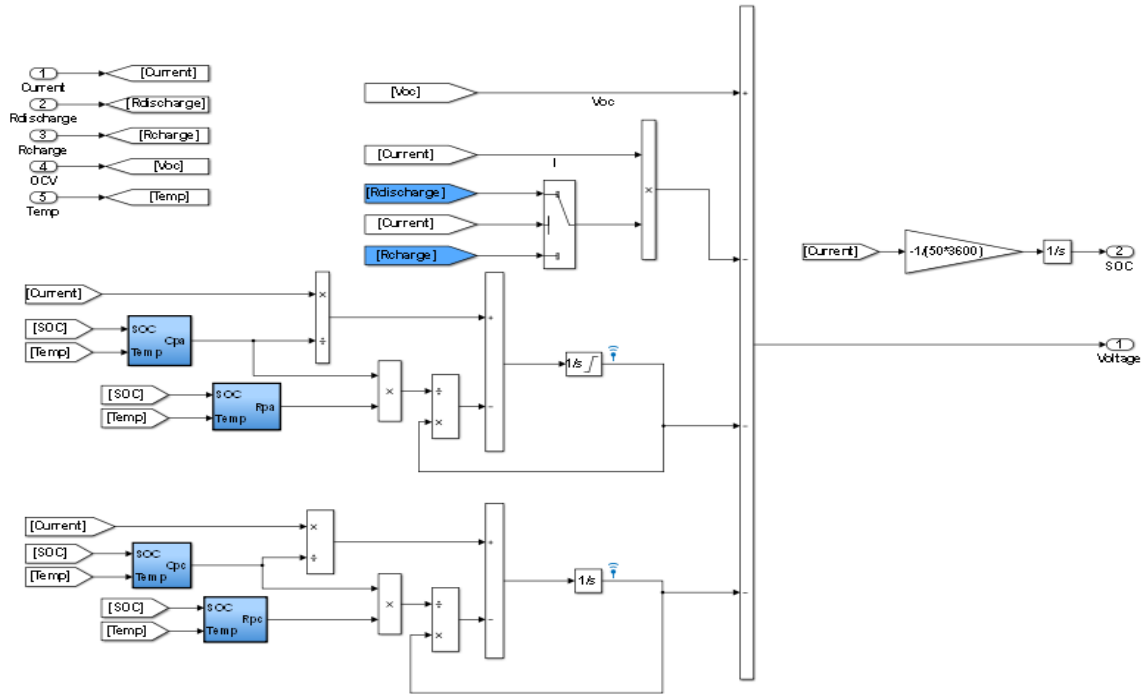


Figure 21. Dynamic component of the TTEC model

Sample Simulation Results

Figure 22 shows voltage response from the actual battery-system and simulated voltage response from the above described TTECM for a HPPC pulse at 40 °C and 0.63 SOC.

It is clearly seen that one time-constant is an order of magnitude slower than the other. The slower time-constant is associated with concentration polarization and the fast time-constant is associated with activation polarization.

Notice the concentration polarization response between 1.17×10^4 s and 1.2×10^4 s. When current is cut-off, all voltage responses show a relaxation. The concentration polarization response is clearly much slower compared to that of the activation polarization. Also notice that the magnitude of the concentration polarization is smaller than that of activation polarization

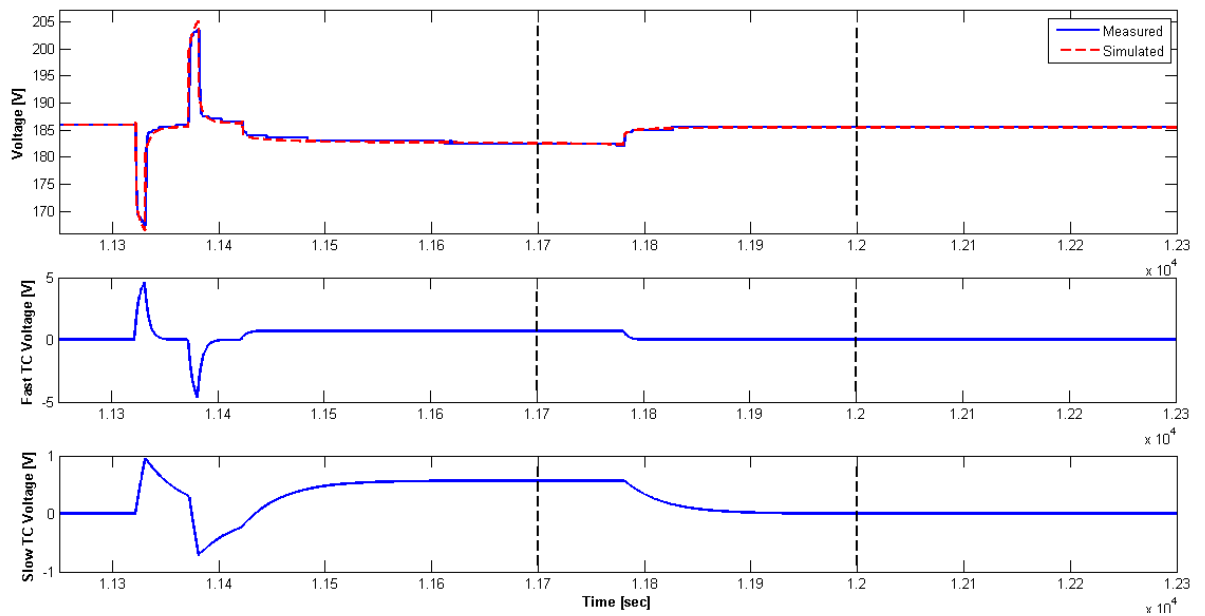


Figure 22. Terminal voltage, and response of the two RC branches to a HPPC pulse at 40 °C

Consequently, when current is cut off, the terminal voltage does go through an initial rapid relaxation because of the rapid drop in activation polarization, with an approximate time constant of 5sec. However, the final part of the relaxation is much slower, since it is driven by the Concentration polarization. This analysis shows the closing of the final 0.5 V gap between the measured terminal voltage and the OCV during the relaxation phase has a time constant of approximately 50 s due to the time-constant of the Concentration polarization.

Figure 23 below shows voltage response from the actual battery-system and simulated voltage response from the TTECM for a HPPC pulse at 20 °C and 0.83 SOC, and inferences similar to the above figure can be derived from it.

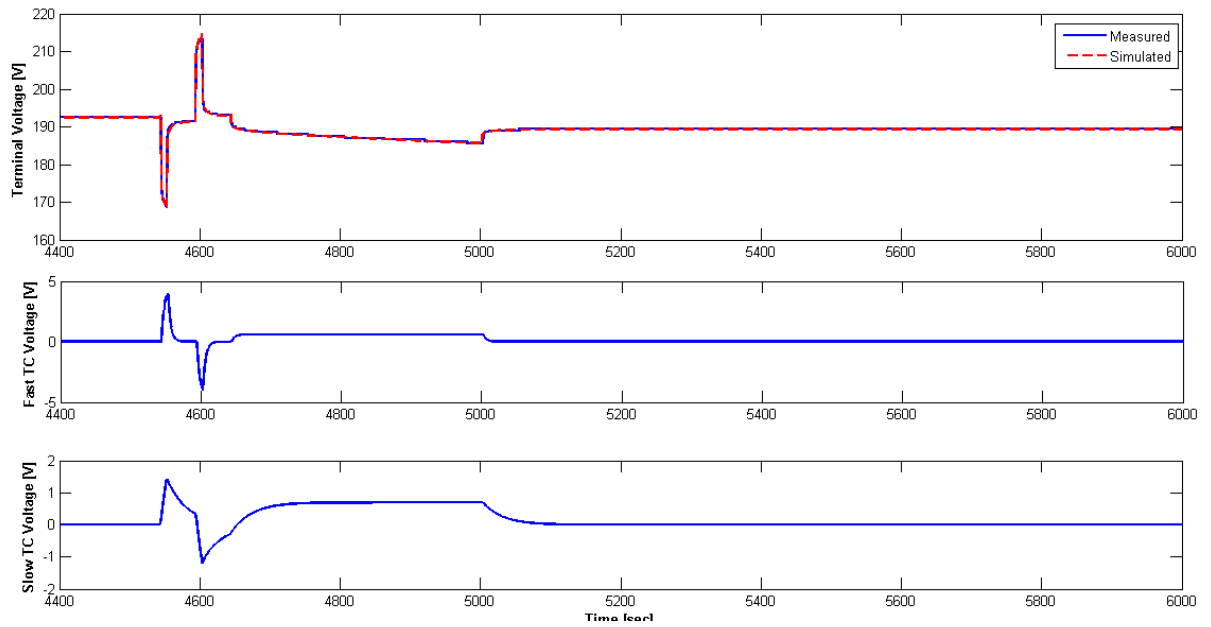


Figure 23. Terminal voltage, and response of the two RC branches to a HPPC pulse at 20 °C

2.7 Model Validation

The final phase of the model development process was validation of the model against experimental data measured from the battery-system. Specifically, the model was validated against HPPC test data and a Federal Urban Driving Schedule (FUDS) which is a typical start-stop, high power-demand, urban driving-cycle.

Figure 24, Figure 25, and Figure 26 below compare simulated voltage response of the TTECM with measured data at 40 °C, 20 °C and -20 °C respectively. While the model accurately captures the characteristics of the battery-system's response at different temperatures and SOCs, the results below show a noticeable error between the measured and simulated response. Maximum residuals of approximately 5 percent can be seen under at certain points in the validation tests.

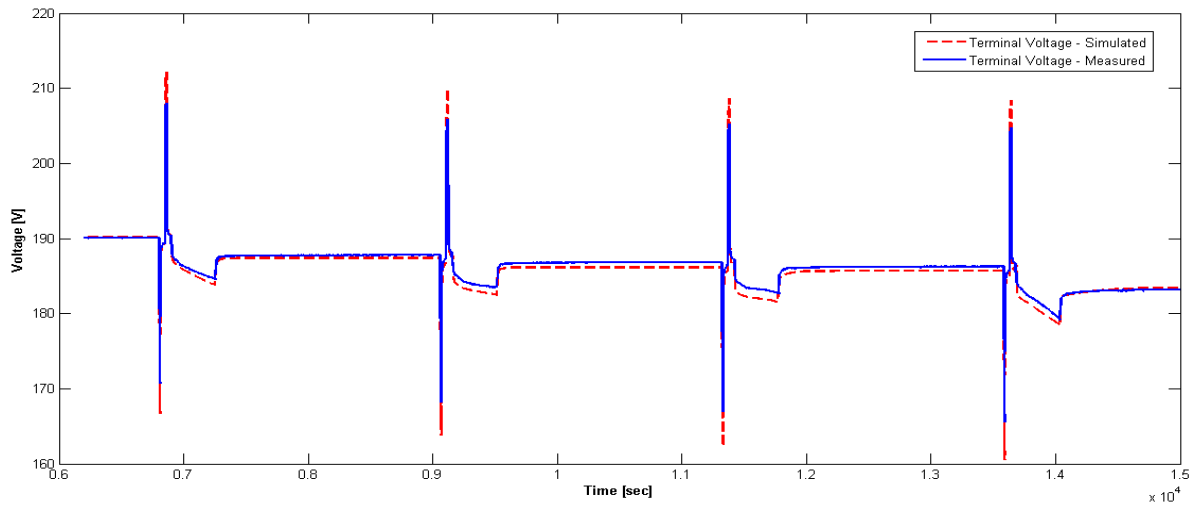


Figure 24. Validation of TTECM with HPPC test data at 40 °C

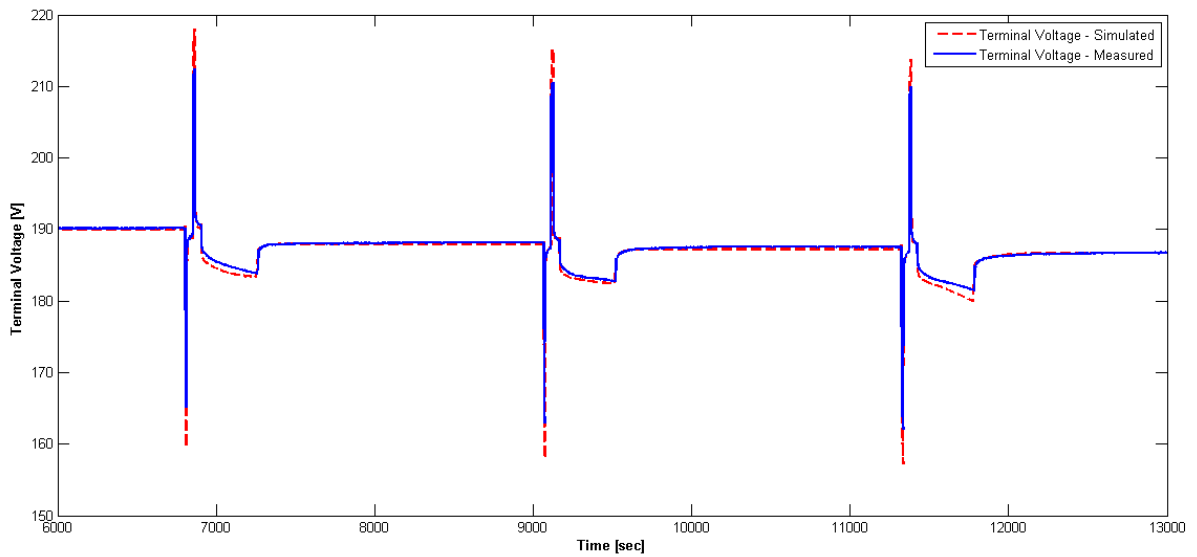


Figure 25. Validation of TTECM with HPPC test data at 20 °C

These errors can be attributed to several factors. While the actual tests were set up to maintain nearly isothermal conditions, the battery system has a very high thermal mass and slight deviations from the temperature set-point are expected. Further, the high C-rate pulses result in a small temperature increases near cell terminals and heat extraction is not fast enough to completely nullify this effect. In addition, the model is executed at a fixed temperature set-point that is enforced programmatically.

A similar effect is seen in Figure 26. The temperature set-point is $-20\text{ }^{\circ}\text{C}$ and small pulses result in quick deviation of the battery system's temperature from the set-point. This was observed during the test, on the data traces of temperature sensors on the battery system. Further, sensitivity of series resistance to temperature is much higher at low temperatures as seen from the Series resistance maps in Figure 13 and Figure 14. Thus the actual series resistance is lower than that used by the model, resulting in the error between measured and simulated responses. Having said that, the model accurately captures the nature of the response, and Residuals are at most 3 percent, even during charge/discharge pulses.

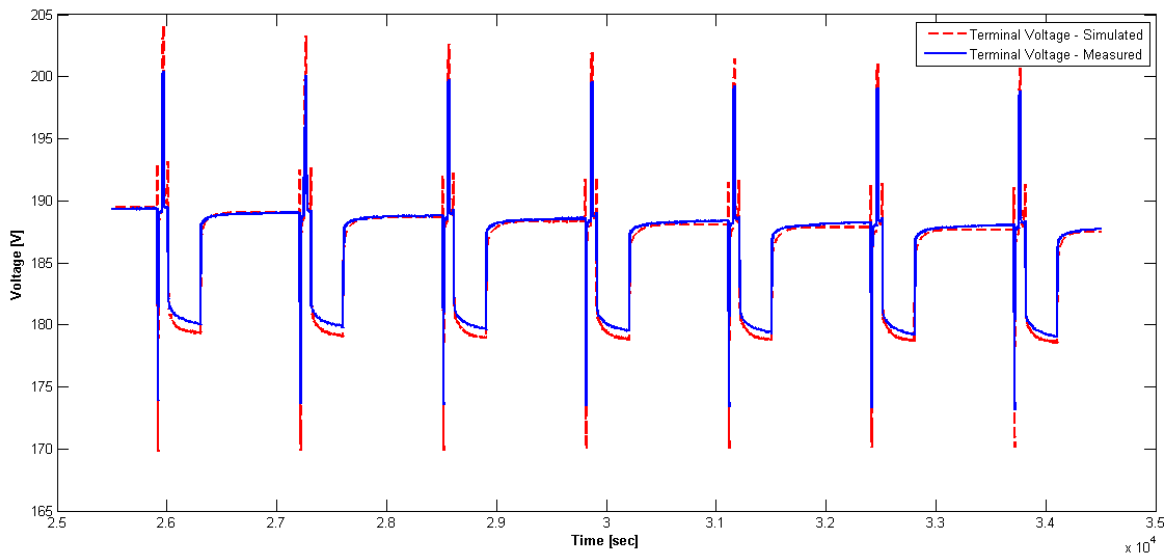


Figure 26. Validation of TTECM with HPPC test data at $-20\text{ }^{\circ}\text{C}$

FUDS is an automobile industry standard time-speed profile of urban driving originally developed by the Environmental Protection Agency (EPA). A version commonly used for plug-in hybrids and electric-vehicles is available in the Battery Test Manual for Plug-In Hybrid Electric Vehicles [10].

It is a variable power discharge regime that best represents the actual power requirements from an electric vehicle in an urban environment. It is demanding in terms of the frequency of high power-peaks and ratio of regenerative to discharge power.

The speed-time trace was converted first to a power-demand trace and then to current-demand trace by making assumptions of a typical transit-bus on which this battery-system would be deployed, and an operating point. Figure 27 shows the current trace.

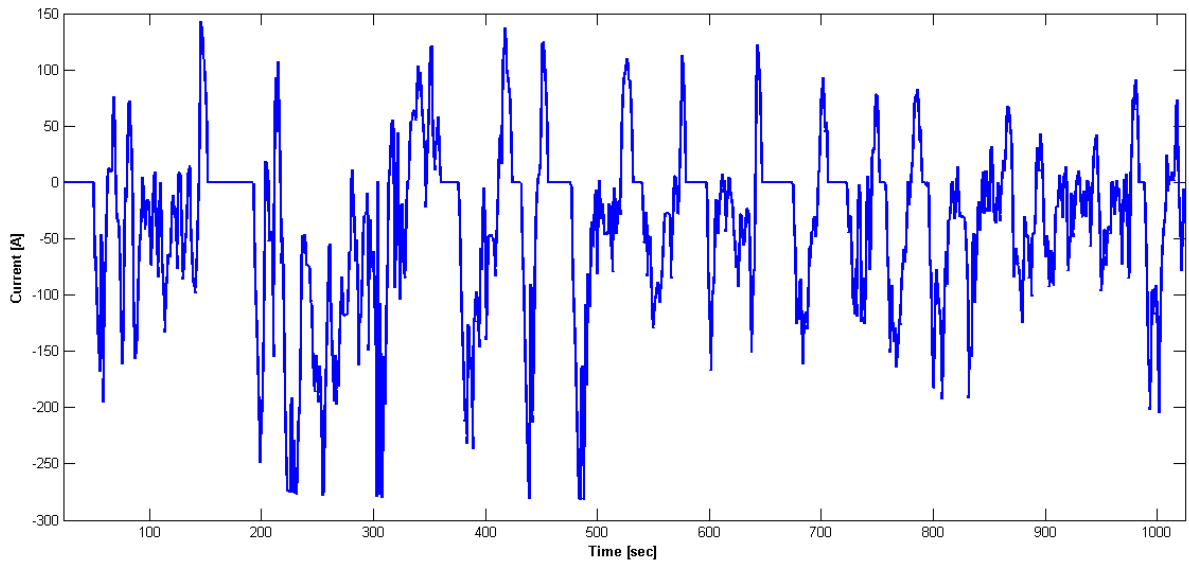


Figure 27. Federal Urban Driving Schedule (FUDS) as a current trace corresponding to a target vehicle application

Figure 28 compares the terminal voltage response of the TTECM with the measured data for the FUDS cycle. The model accurately simulates all transients and steady-states. It shows a maximum of 2.22 percent error, which is seen only during a high power discharge or charge pulse.

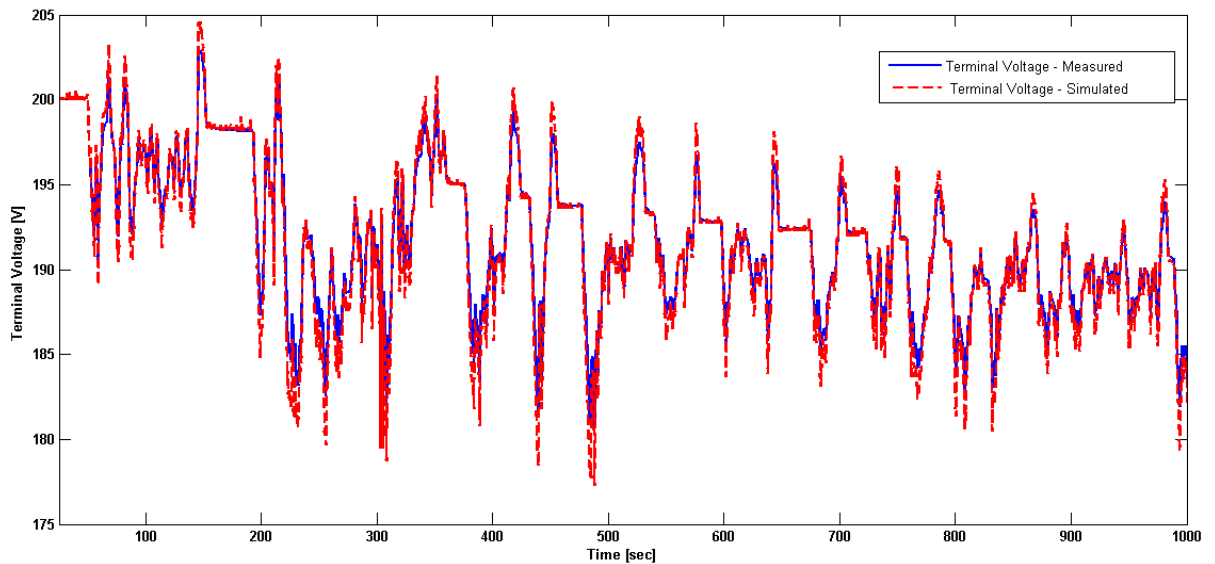


Figure 28. Validation of the TTECM with FUDS

The model developed in this chapter is currently being used by project stake-holders in their full-vehicle simulations. Further, this work uses the model developed here as a basis to design an improved SOC estimator based on Extended Kalman Filtering. The SOC estimator is validated

with this model and then verified with experimental data. It is deployable on the battery-system's monitoring hardware. This is described in the next chapter.

Lastly, since this model captures temperature dependence of the electric parameters, accurate full-vehicle simulations required either temperature data recorded from the actual system, or an accurate thermal-model of the battery system. Chapters 4 and 5 of this work detail the process of characterizing thermal dynamics within the battery system and development of a system-level thermal model that could be coupled with the electrical model.

Chapter 3. State of Charge Estimation

The transit-bus battery system is currently equipped with a management system that uses a primitive State of Charge (SOC) estimation scheme, using a combination of voltage look-up and coulomb counting. The SOC estimator is sensitive to sensor noise, drift, and initialization errors.

A key objective of this work was to develop, validate, and verify an improved online SOC estimator that to operate across the entire SOC range. This chapter describes the development of this estimator, from model, to production C code, followed by results of its simulation and software-in-Loop (SIL) and hardware-In-Loop (HIL) verification. This development work is differentiated by the fact that vast amounts of data from empirical characterization of the actual battery-system is leveraged, and the estimator is migrated to production C code, and verified in real-time. The previously discussed TTECM forms the basis for this development. In doing so, this chapter exemplifies the utility of the previously discussed modeling effort, in developing, validating, and deploying improved battery monitoring algorithms.

3.1 Approach – An Extended Kalman Filter

In order to leverage the empirical characterization data of the battery-system, the complete TTECM developed in the previous chapter needs to be used. While the parameters vary with temperature, a preliminary review of the literature shows that accounting for thermal effects significantly complicates the SOC estimator. This work thus assumes that an external thermal management system will maintain the battery temperature within 15 °C to 30 °C limits. Thus, only an isothermal case is considered. However, this is analogous to introducing modeling uncertainties, to which the estimator must be robust. Further, variation of TTECM parameters w.r.t. SOC, at a constant temperature, still introduce non-linearity.

Secondly, since the end-goal is to implement the estimator on automotive hardware it had to be implemented in discrete-time. The estimator will use digitized versions of current and voltage measurements from sensors on the battery-system. These are noisy, and the estimator must be robust to measurement noise.

The literature contains a wide variety of work on online, estimation of battery SOC. Piller et al. [12] and Pop et al. [13] review the broad categories of SOC estimation schemes, and their benefits and drawbacks. They compare results from different schemes including Coulomb Counting, Kalman Filters, and Neural Networks.

Citing conclusions from these works, and based on the practical considerations noted above, the non-linear, Extended Kalman Filter (EKF) appeared to be most appropriate.

Plett, in his three part work on EKFs for battery management systems [14], describes in detail, its implementation using several different non-linear models. He also illustrates the use of this scheme in several related application like initializing the SOC estimate, estimating available power, etc.

More recently, De Domenica et al. [15] have demonstrated implementation of EKFs for SOC estimation, but with adaptive weights. They point out that the EKF scheme does not perform equally well across the entire SOC range and that adapting the filter's weights in different parts of the SOC range gives better results.

Huria et al. [4] demonstrate a simplified EKF scheme combined with traditional current counting, based on a two time-constant ECM, that offers a computationally efficient solution for run-time implementation on vehicles.

This work implements an SOC estimator in the form of a discrete-time, non-linear, Extended Kalman Filter, with adaptive filter weights. The following sections describe its implementation, validation and verification.

3.2 Extended Kalman Filter as an SOC Estimator

The following section describes the mathematical formulation and Simulink® implementation of the SOC estimator. The TTECM model implementation is modified to only use the variation of parameters w.r.t. SOC at 40 °C only, i.e. an isothermal case. This modified version forms the basis of the estimator. Secondly, the model is discretized, to implement a discrete-time EKF. Thirdly, data from the voltage transducer is used to find the covariance of the measurement noise process and is used in the filter. The filter is first implemented in Simulink and the battery model from Chapter 2 is used to tune and validate its performance. The weight matrices Q and R matrices is varied to obtain the best filter performance in different SOC ranges [15]. The text-book by Dan Simon [16], on optimal state estimation was extensively used as a primary reference in implementing and tuning the EKF.

State Transition Function

$$\mathbf{x}^{k+1} = \mathbf{f}_k(\mathbf{x}^k, \mathbf{i}^k, \mathbf{w}^k)$$

$$U_f^{k+1} = \exp\left(\frac{-\Delta T}{\tau_f(SOC^k)}\right)V_f^k + R_f(SOC^k)\left(1 - \exp\left(\frac{-\Delta T}{\tau_f(SOC^k)}\right)\right)i^k$$

$$U_s^{k+1} = \exp\left(\frac{-\Delta T}{\tau_s(SOC^k)}\right) V_s^k + R_s(SOC^k) \left(1 - \exp\left(\frac{-\Delta T}{\tau_s(SOC^k)}\right)\right) i^k$$

$$SOC^{k+1} = SOC^k + \frac{\eta \Delta T i^k}{C_n}$$

Measurement Function

$$y^k = g_k(x^k, i^k, v^k)$$

$$V_{terminal}^k = -U_s^k - U_f^k - i^k R_o(SOC^k) + V_{OC}(SOC^k)$$

State Vector

State Vector at time step k : $x^k = (V_a^k \ V_c^k \ SOC^k)^T$ Where,

U_f^k - Voltage drop across fast RC branch

U_s^k - Voltage drop across slow RC branch

SOC^k - State of Charge of the Battery.

Model Input

i^k - Measured value of battery current at the k^{th} time step.

Model Output

$V_{terminal}^k$ - Terminal voltage at the k^{th} time step.

Model Parameters

$\tau_f(SOC^k)$ - Time-Constant of fast RC branch as function of SOC

$R_f(SOC^k)$ - Resistance of fast RC branch as function of SOC

$\tau_s(SOC^k)$ - Time-Constant of slow RC branch as function of SOC

$R_s(SOC^k)$ - Resistance of slow RC branch as a function of SOC

$R_o(SOC^k)$ - Series resistance as function of SOC

$V_{OC}(SOC^k)$ - Open Circuit voltage as a function of SOC.

ΔT - Discrete time-step size

w^k - Zero-mean Gaussian white process noise k^{th} time-step

v^k – Zero-mean Gaussian white measurement noise at k^{th} time-step

Implementation of the SOC Estimator in Simulink®

Figure 29 is an overview of the SOC estimator’s implementation in Simulink. In this setup, the TTEC model developed in the previous chapter is used along with simulated measurement noise.

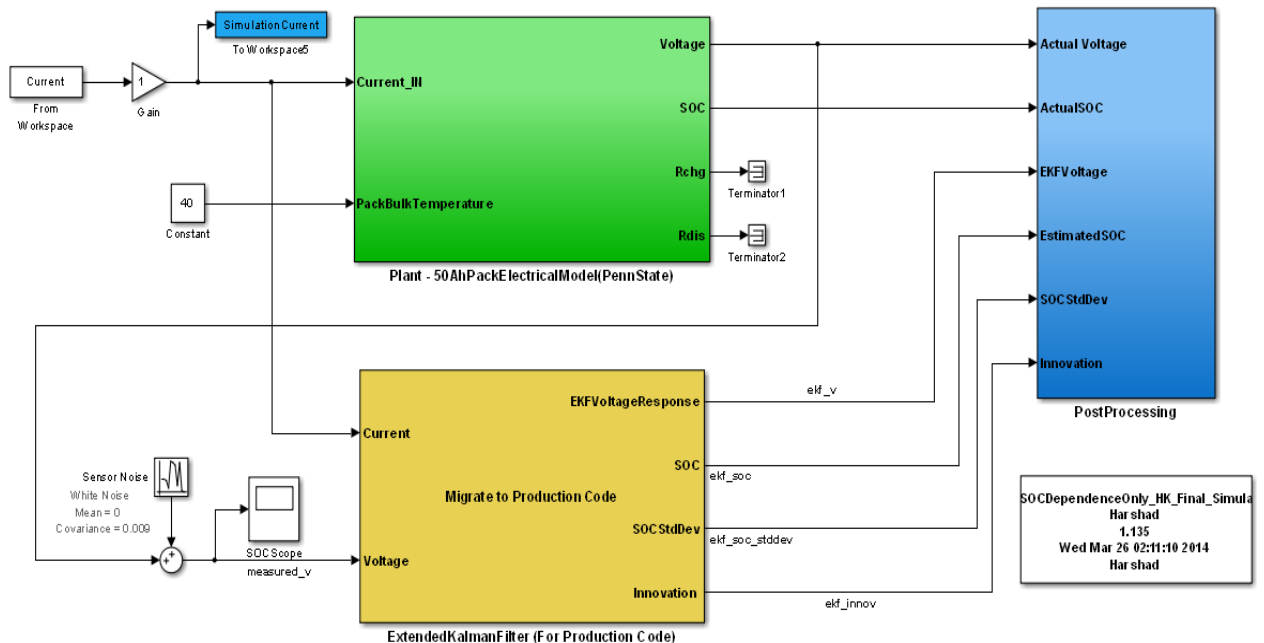


Figure 29. Overview of the Simulink® implementation of the SOC Estimator

Figure 30 shows the detailed implementation of the SOC Estimator. It shows two MATLAB Function blocks – one that implements the Time Update Stage and another that implements the Measurement Update Stage of the EKF. The filter is initialized with values of x_0 and P_0 as the initial state estimate and covariance of the state estimates respectively. P_0 is a 3×3 matrix, and x_0 is a 3×1 vector. Q and R are the weight matrices of the filter. Q is a 3×3 matrix and R is a 1×1 matrix. The weight matrices are tuned to obtain the best SOC estimation performance from the filter. Details of this are presented in the following section.

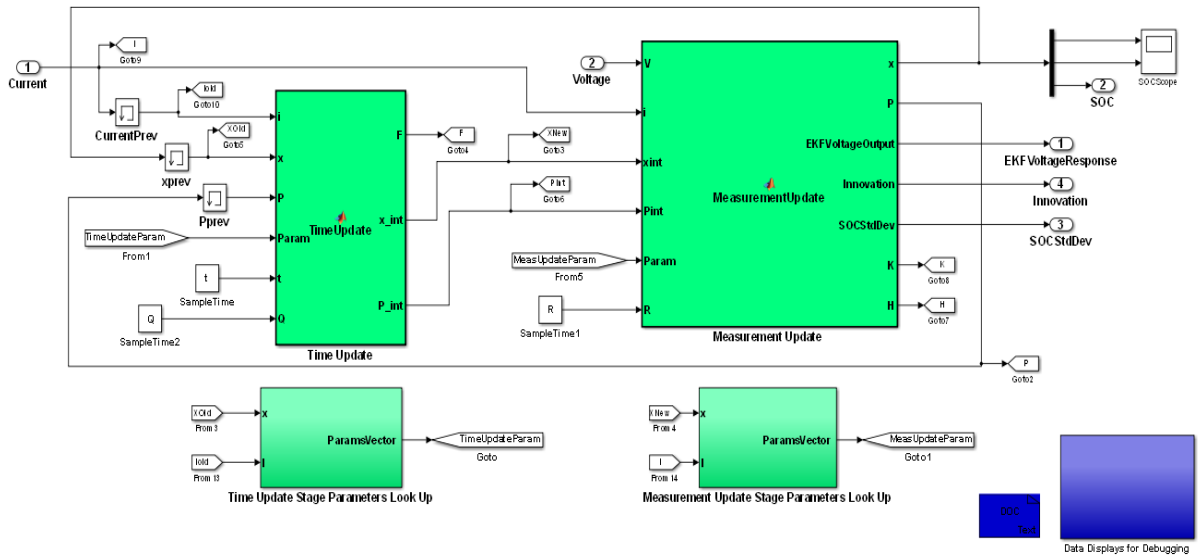


Figure 30. Detailed Implementation showing Time-Update & Measurement Update stages

At every time-step, all parameters of the discretized state and measurement equations of the battery model, are evaluated as a function of SOC, within the EKF. This is done through a series of Look-Up Tables that contain maps of different model parameters, and their derivatives, with respect to SOC. Figure 31 below is the implementation of these Look-up Tables.

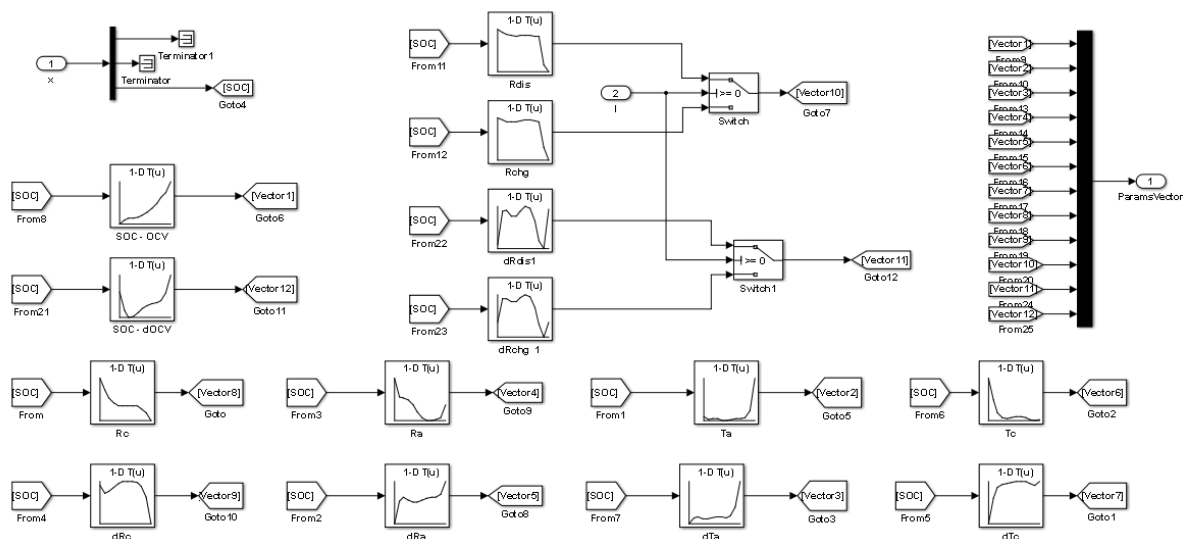


Figure 31. Implementation of parameter maps through Simulink® Look-Up Table

3.3 Migrating the SOC Estimator to Production Code

As stated previously, a key objective of this work was to develop an SOC estimator that is based entirely on empirical characterization of the battery system in our lab, and is deployable to automotive hardware.

To that end, this work goes beyond simulations, to development of production C code, SIL, and HIL verification of the estimator. This section highlights the key considerations and steps in migrating the SOC estimator from simulations to production code.

Choice of Representative Hardware – ARM Cortex-R4

The ARM Cortex R4 is a 32-bit, 160 MHz, high performance microprocessor with a separate floating-point unit. It is deployed on electronic control units (ECUs) such as the Texas Instruments TMS570, which are used in safety-critical automotive applications such as motor and transmission control, power steering, battery management, etc. [17].

This unit thus serves as the ideal “representative hardware” to demonstrate migration of the SOC estimator to production C code.

Implementation of Look-Up Tables

Look-up Tables of parameters, based on SOC, are the most computationally intensive component of the SOC estimator. They involve two phases, namely, finding the indices closest to the current SOC, followed by interpolation of the parameter values corresponding to the nearest indices. The C implementation of this must be efficient in space and time.

The Binary Search algorithm is employed to look-up indices corresponding to the current SOC. This technique is more efficient than other search methods such as Linear Search. Moreover, note that the SOC value does not vary significantly over a 1 s time-step. This characteristic of the system’s dynamics is leveraged to speed-up the index lookup. The index value from the previous time step is used to initialize the Binary Search during the current time step, resulting in decreased time complexity of the search [18]. Figure 32 shows C implementation of the Binary Search.

Interpolation of values from Look-Up Tables can be Linear or Cubic Spline. Cubic Spline interpolation is more complex in space and time compared to Linear Interpolation, since it uses three sample points per interpolation (vis-à-vis two for Linear), and involved calculations of spline coefficients. However, it guarantees continuity of derivatives at all points in the domain.

The choice of interpolation technique thus affect both accuracy and speed of the estimation process.

In this specific case, polynomial curve-fits of model parameters w.r.t. SOC guarantee continuity of the derivatives. Derivatives are calculate at specific SOC points and separate look-up tables are constructed from these sample points. Thus, the Cubic Spline interpolation's feature of guaranteeing continuity of the derivative, is not required. Furthermore, SOC estimation accuracy and speed with the two different interpolation techniques was compared in simulation and showed no significant difference. Thus, Linear interpolation is chosen as the optimum choice for the SOC estimator C code.

```
33  real T look1_pbinlpxw(real T u0, const real T bp0[], const real T table[],
34                      uint32 T prevIndex[], uint32 T maxIndex)
35  {
36      real T frac;
37      uint32 T startIndex;
38      uint32 T iRght;
39      uint32 T iLeft;
40      uint32 T found;
41
42      /* Lookup 1-D
43         Search method: 'binary'
44         Use previous index: 'on'
45         Interpolation method: 'Linear'
46         Extrapolation method: 'Linear'
47         Use last breakpoint for index at or above upper limit: 'off'
48         Remove protection against out-of-range input in generated code: 'off'
49      */
50      /* Prelookup - Index and Fraction
51         Index Search method: 'binary'
52         Extrapolation method: 'Linear'
53         Use previous index: 'on'
54         Use last breakpoint for index at or above upper limit: 'off'
55         Remove protection against out-of-range input in generated code: 'off'
56      */
57      if (u0 <= bp0[0U]) {
58          startIndex = 0U;
59          frac = (u0 - bp0[0U]) / (bp0[1U] - bp0[0U]);
60      } else if (u0 < bp0[maxIndex]) {
61          startIndex = prevIndex[0U];
62
63          /* Binary Search using Previous Index */
64          iLeft = 0U;
65          iRght = maxIndex;
66          found = 0U;
67          while (found == 0U) {
68              if (u0 < bp0[startIndex]) {
69                  iRght = startIndex - 1U;
70                  startIndex = (iRght + iLeft) >> 1U;
71              } else if (u0 < bp0[startIndex + 1U]) {
```

```

72     found = 1U;
73     } else {
74         iLeft = startIndex + 1U;
75         startIndex = (iRight + iLeft) >> 1U;
76     }
77 }
78
79     frac = (u0 - bp0[startIndex]) / (bp0[startIndex + 1U] - bp0[startIndex]);
80 } else {
81     startIndex = maxIndex - 1U;
82     frac = (u0 - bp0[maxIndex - 1U]) / (bp0[maxIndex] - bp0[maxIndex - 1U]);
83 }
84
85     prevIndex[0U] = startIndex;
86
87     /* Interpolation 1-D
88        Interpolation method: 'Linear'
89        Use last breakpoint for index at or above upper limit: 'off'
90        Overflow mode: 'portable wrapping'
91    */
92     return (table[startIndex + 1U] - table[startIndex]) * frac + table[startIndex];
93 }
94 ..

```

Figure 32. C code of the Binary Search and Linear Interpolation used by Look-Up Tables

Provision for Parameter Tuning

During the course of SIL and HIL verification of the SOC estimator, several parameters need to be tuned to improve the estimator’s performance. Specifically, Sample-time [t], Initial State Estimate [x0], Initial State Covariance Matrix [P0], and matrices Q and R, are parameters that must be tunable. Other parameters and data used by the estimator can be treated as constants and hard-coded. This distinction is clearly visible in the code snippet shown in Figure 33.

```

20  /* Block parameters (auto storage) */
21  P_ExtendedKalmanFilter_T ExtendedKalmanFilter_P = {
22  /* Variable: P0
23   * Referenced by: '<S1>/Pprev'
24   */
25   { 10.0, 0.0, 0.0, 0.0, 10.0, 0.0, 0.0, 0.0, 2.0 },
26
27   /* Variable: Q
28   * Referenced by: '<S1>/SampleTime2'
29   */
30   { 0.0, 0.0, 0.0, 0.0, 0.0, 0.0, 0.0, 0.0, 0.0, 0.01 },
31   0.5, /* Variable: R
32   * Referenced by: '<S1>/SampleTime1'
33   */
34   1.0, /* Variable: t
35   * Referenced by: '<S1>/SampleTime'
36   */
37
38   /* Variable: x0
39   * Referenced by: '<S1>/xprev'
40   */
41   { 0.0, 0.0, 0.3 }
42  };
43
44  /* Constant parameters (auto storage) */
45  const ConstP_ExtendedKalmanFilter_T ExtendedKalmanFilter_ConstP = {
46  /* Pooled Parameter (Expression: EKFTabledRchg)
47   * Referenced by:
48   * '<S5>/Rchg_1'
49   * '<S7>/dRchg_1'
50   */
51   { -0.17934022353075818, 0.00208381267938762, 0.0085322803378034,
52     -0.017150991636356139, -0.015600278268877332, 0.014197496751137351,
53     0.040028216353114487, 0.021576025366400131, -0.064451214197958961,
54     -0.19919646786541989, -0.29652807341712872, -0.17791428560637002 },
55

```

Figure 33. Distinction between SOC estimator’s tunable parameters and constants, in the production C code

Code Optimizations

Explicit care is taken to ensure that no superfluous local copies of variables are produced. Further, the block diagram of the estimator is translated to tightly wrapped C code, without unnecessary intermediate steps and equations. All parameters that are not required to be tunable, are hard-coded thus reducing static memory consumption.

Furthermore, MATLAB’s Embedded Coder product has a built in GNU Compiler Collection (GCC) ARM Cortex R4 Code Replacement Library. In this library, several mathematical operations such as *exp* and *sqrt* are optimized subroutines that leverage certain hardware capabilities of this processor. Embedded Coder automatically replaces all instances of such functions in the SOC estimator’s C code, with their equivalents from this library, thus making the code more efficient.

The final, production C code for the SOC estimator is subjected to SIL and HIL verifications using the battery-system model, and the actual battery-system hardware, respectively. This is illustrated in the following sections.

3.4 Simulations and Software-In-Loop Verification

The SOC estimator is implemented in Simulink as discussed previously. Following this, Embedded Coder is used to automatically generate ANSI C code for the SOC estimator, optimized for an ARM Cortex R4 microprocessor. At this stage, verification is required for several reasons.

Firstly, there is an inherent difference in the behavior of the estimator when it operates with the Simulink engine, and when it operates as a C executable. Thus, accuracy and performance of both, the estimator model and its C code, are explicitly verified. This is also done to ensure numerical equivalence between the two.

Moreover, the estimator's performance is tested over short, aggressive driving schedules (e.g. FUDS) as well as long duration tests (e.g. HPPC). Lastly, the estimator's performance is measured with different parameter values, to identify the best values to span the entire SOC range.

Accuracy and performance of the C code generated for the estimator is verified using the software-in-loop simulation technique available with MATLAB/Simulink. SIL allows verification of the production C code, in a simulation environment, without needing deployment to vehicle hardware. The Simulink model used for this verification is shown in Figure 34.

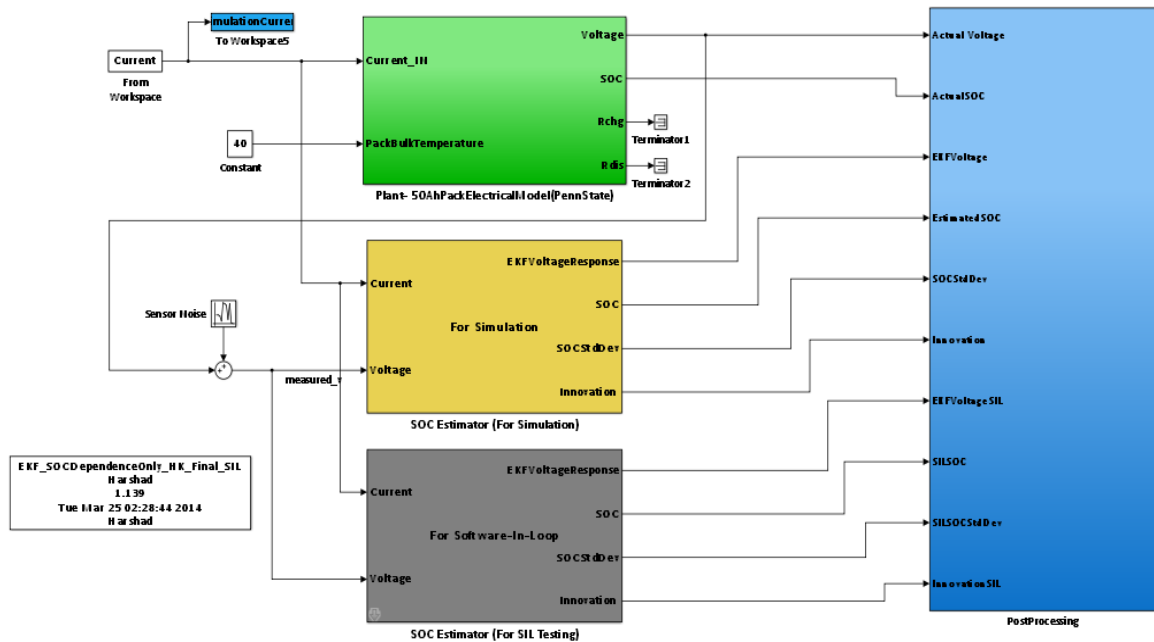


Figure 34. Simulink® model used to conduct simulation and software-in-loop verification of the SOC estimator

The *SOC Estimator (For SIL Testing)* block in the above image is a SIL block. An *.exe* executable of the SOC estimator's C code, customized for an ARM Cortex R4 processor, is first generated. It is then interfaced with the Simulink engine through the S-Function API. The plant model of the battery system, developed in previous chapters, is executed in Simulink and its voltage and current signals are passed to the *.exe* which is executed by the operating system [19]. Results from the executable are visualized and post processed in Simulink.

Filter Performance Metrics & Tuning of Weight Matrices

The SOC estimator's performance was evaluated in a manner similar to work by Plett [14], and Di Dominica et al. [15]. Several metrics were observed in the simulation and verification process. Evolution of the terminal voltage predicted by the EKF, and that of the Innovation, was monitored. Instantaneous SOC estimation error, SOC root mean squared (RMS) error over the entire test-period, and variance of SOC estimate, were key metrics of accuracy. Time taken for the SOC estimate to converge to the actual value, was also a key performance metric.

After some preliminary SIL tests, it was apparent that the estimator's performance varied in different SOC ranges, and with extent of initial SOC estimation error. This deviation can be attributed to a variety of factors. Firstly, the battery (plant) model itself executed inside the Simulink engine, through a variable-step solver that simulates continuous-time. However, the estimator is based on a discretized model and executes in discrete-time. Secondly, the battery model uses Cubic Spline interpolated parameter maps whereas the estimator uses linearly interpolated maps for computational simplicity. Through a combination of these factors, a form of modeling uncertainty is introduced into the estimator, and its extent is dependent on the SOC range the estimator is operating in.

A similar situation is illustrated by Di Dominica et al. [15]. Based on their work, weight matrices Q and R were manually tuned to improve the estimator's performance in different conditions thus giving rise to adaptive filter weights. Tuning of Q and R required adjusting trade-offs between the filter's accuracy and precision, represented by mean and standard deviation of the estimation error, respectively.

Note that Q is a 3×3 matrix. Here, Q is represented as Q*I where I is the identity matrix. Thus, values of Q are written as scalars in remainder of this chapter.

Verification with FUDS Cycle Profile

FUDS is characterized by short, aggressive, discharge and charge periods, interspersed with short rest periods. It is used to verify the estimator's ability to accurately and quickly respond during aggressive duty cycles.

Figure 35 is a test with actual initial SOC of 0.8 and an initial SOC estimate of 0.75. The SOC estimate and voltage converge to the actual profile almost immediately, with no noticeable drift during the test. Estimation error remains under 1 percent throughout, with a final RMS error of 0.0014 SOC. Note that $Q = 1e-6$ and $R = 0.009$ are used here.

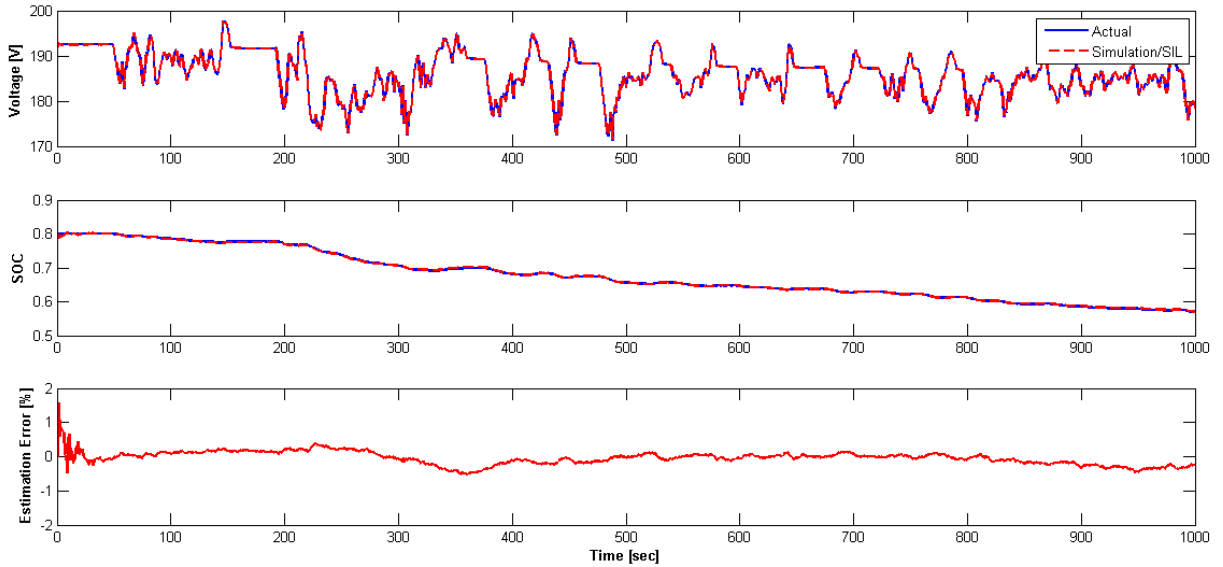


Figure 35. Comparison of actual voltage and SOC with that predicted by the SOC estimator operating as software-in-loop, using FUDS [Actual Initial SOC = 0.80, Initial Guess = 0.75]

Figure 36 is a test with the pack exercised in a lower SOC range. The actual initial SOC is 0.55 with an initial SOC estimate of 0.35. The SOC estimate and voltage converge to the actual profile after ~ 200 s, which is longer than in the previous case. However, no noticeable drift is seen during the remainder of the test. Beyond 200 s, estimation error settles to under 1 percent. A final RMS error of 0.054 SOC is seen. Unlike the previous test, higher values of Q and R were required to obtain a satisfactory response, highlighting the need to find best parameter values for broad SOC ranges. Here, $Q = 1e-4$ and $R = 0.052$ was used.

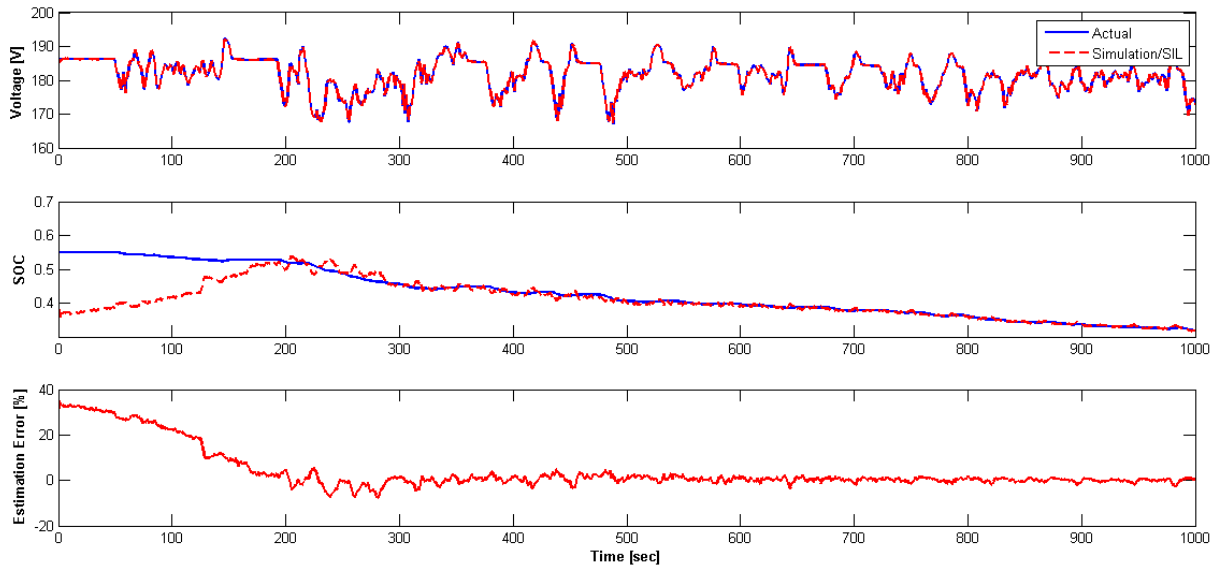


Figure 36. Comparison of actual voltage and SOC with that predicted by the SOC Estimator operating as software-in-loop using FUDS [Actual Initial SOC = 0.55, Initial Guess = 0.35]

Figure 37 shows results of the FUDS cycle executed at a lower SOC range. The actual initial SOC is 0.45 and the initial SOC estimate is 0.25 i.e. a ~50 percent error. The SOC estimate and voltage come close to the actual profile within ~200 s but take over ~600 s to completely converge. Estimation error ultimately settles to under 1 percent, but with a high RMS error on the SOC estimate.

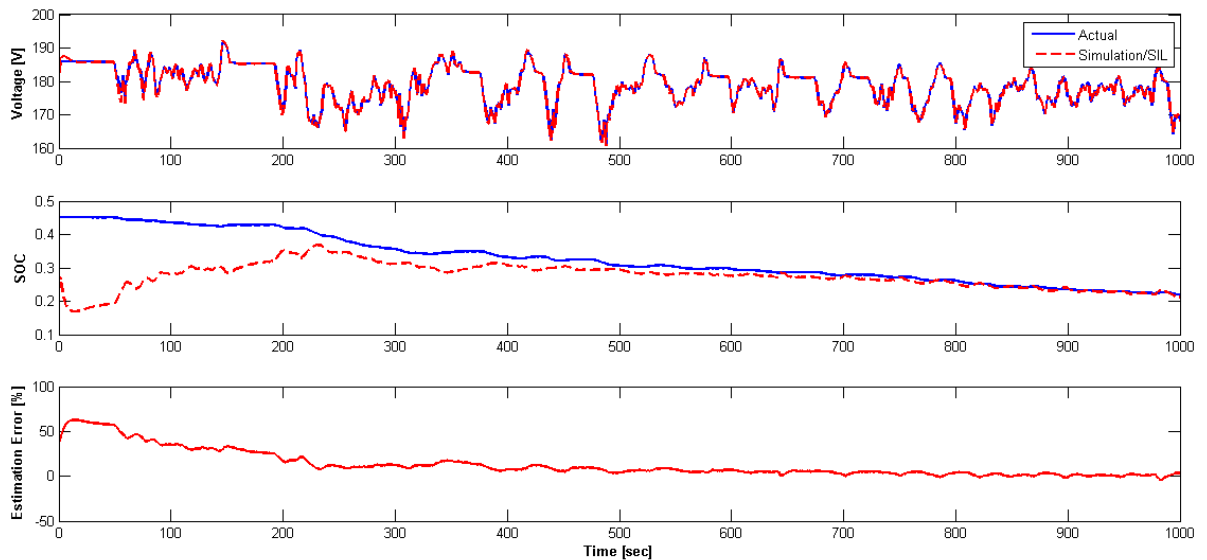


Figure 37. Comparison of actual voltage and SOC with the SOC estimator operating as software-in-loop using FUDS [Actual Initial SOC = 0.45; Initial Guess = 0.25][$Q = 1e-4$; $R = 0.052$]

The above scenario was tested with two different sets of parameters, to illustrate the sensitivity of the response, to these parameters, especially in the low SOC range. The comparison is in

Figure 38. The response described previously was at $Q = 1e-4$ and $R = 0.052$. With $Q = 1e-3$ and $R = 0.12$, the estimate converges to the actual value in under 200 s, and shows no significant drift over the test. However, the trade-off is an increased sensitivity to noise as expected. In both cases, the Estimation error settles to under 1 percent, but the convergence time is much lower in the second case. Further, the RMS error in the second case is 0.02 SOC vis-à-vis 0.08 SOC in the first.

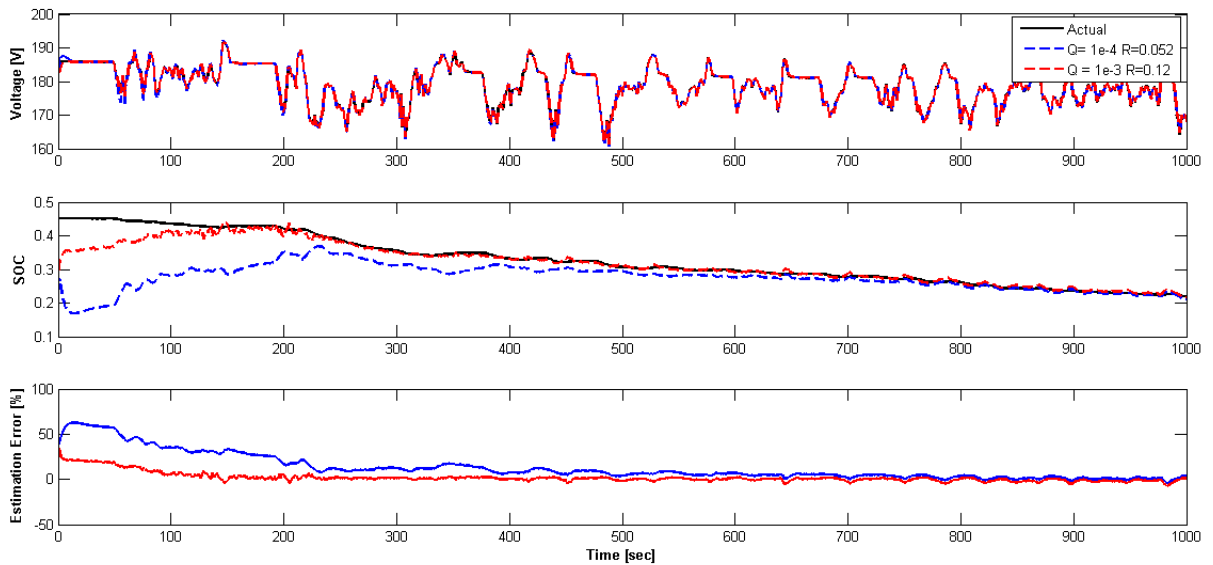


Figure 38. Comparison of SOC Estimator performance for different values of Q and R [$Q = 1e-4$ $R = 0.052$; $Q = 1e-3$, $R = 0.12$]

Verification with HPPC Test Profile

The HPPC is a prolonged test profile (~ 7 h) consisting of charge/discharge pulses, and constant C-rate discharge, followed by long rest periods. The profile spans the entire SOC range. It is used here to observe the estimator's stability and accuracy over a wide SOC range and prolonged testing

Figure 39 is a test with an initial SOC of 0.8 and an initial SOC estimate of 0.6. Voltage and SOC profiles converge to the actual profiles almost instantly. The estimates do not show any significant drift over most of the SOC range up to 0.3. Notice that at SOC below 0.3, the estimate shows increasing deviation. Around 0.1 SOC, estimation error shoots up to ~ 10 percent. Note that $Q = 1e-8$ and $R = 0.009$ during this test.

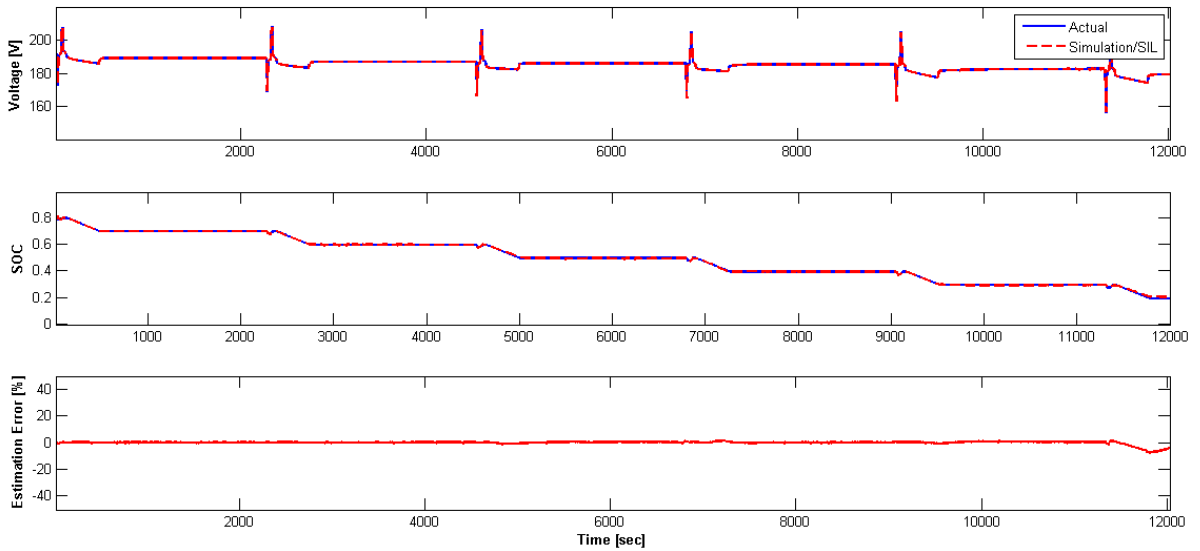


Figure 39. Comparison of actual voltage and SOC with that predicted by SOC Estimator operating as Software-in-Loop using HPPC [Actual Initial SOC = 0.8; Initial Guess = 0.6][$Q = 1e-6$; $R=0.009$]

Figure 40 below is a test with an initial SOC of 0.8 but a highly deviant initial SOC estimate of 0.2. Voltage and SOC profiles take nearly 300 s to converge to actual trace. This is achieved by using $Q = 1e-4$ and $R = 0.052$. Lower values of the Q and R result in convergence times of greater than 2000 s which is unsatisfactory. As a trade-off, with higher value of Q , state estimates have a higher variance. Further, the estimation error converges to at most under 5 percent vis-à-vis under 1 percent in the previous case. A final RMS error of over 0.1 SOC is seen.

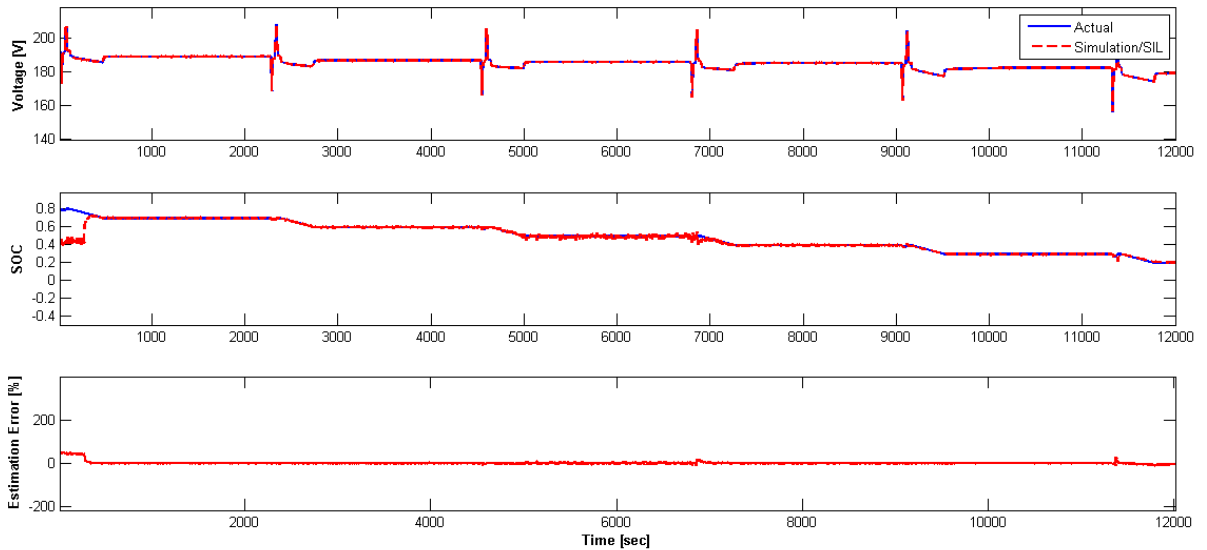


Figure 40. Comparison of actual voltage and SOC with that predicted by SOC estimator operating as software-in-loop using HPPC [Actual Initial SOC = 0.8; Initial Guess = 0.2][$Q = 1e-3$; $R=0.12$]

3.5 Hardware-In-Loop Verification

In all the simulations and SIL verifications presented above, the voltage and current measurements used by the SOC estimator are signals from the battery system model implemented in Simulink. However, there are two fundamental differences between the battery-system model in Simulink and real vehicle hardware. Firstly, the real battery-system may deviate slightly from the plant model on which the SOC estimator has been designed. Thus, the voltage response of the real battery system may be slightly different compared to simulations. Secondly, on a real battery system, specifically the one in our lab, voltage and current measurements are received by the system's controller as digital values serially transmitted over a 125 kbaud controller area network (CAN) bus. Digitization has a resolution of 0.5 V and 0.5 A for voltage and current measurements respectively. This is unlike the Simulink environment where a continuous signal is simply sampled at a certain frequency. Thus, it is important to verify the estimator's performance in a scenario as close to reality as possible.

To that end, pre-recorded voltage and current data from the real battery system's CAN bus is used as an input to the estimator software. The estimator's C code is executed in real-time on the Windows 8 kernel, using Real-Time Windows Target. The data is sent back to Simulink where it can be visualized [20]. This is thus a form of hardware-in-loop verification of the SOC estimator.

Figure 41 below demonstrates performance of the estimator operating in real-time. The battery's initial SOC is ~ 0.92 . An SOC estimate of 0.8 is used to initialize the estimator. The predicted voltage converges to the actual voltage trace in ~ 450 s and does not drift during the remainder of the test. The standard deviation of the SOC estimate is initially 0.001 and gradually settles to under 0.0002 SOC. This can be seen on the SOC estimate trace which shows aggressive jumps in the first ~ 400 s before settling down. Note that $Q = 1e-8$ and $R = 0.009$ during this test. This test helped verify the satisfactory performance of the estimator. Two key issues cause the relatively slow convergence and high estimation error during the initial part of the test. Specifically, there are deviations between the actual battery-system and the model developed in this work. Secondly, the SOC estimator uses an isothermal model. However, the actual battery system is at a slightly different temperature. There are further deviations due to model-discretization as described earlier. Consequently, a form of uncertainty is introduced into the estimator resulting in the performance seen below.

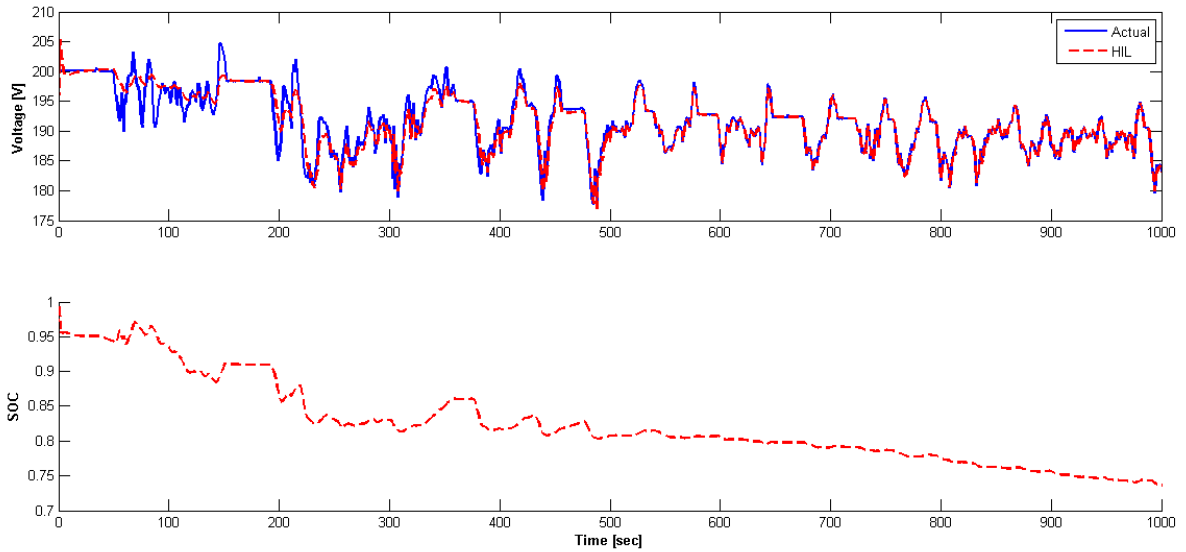


Figure 41. SOC estimator performance with digitized voltage and current measurements obtained over a CAN Bus i.e. HIL [Initial SOC Guess = 0.6; $Q = 1e-8$; $R = 0.009$]

As was done in the SIL phase, the SOC estimator’s weight matrices Q and R were tuned so as to improve performance. Figure 42 compares HIL test runs on the same CAN bus data-trace, using three different sets of weight matrices Q and R .

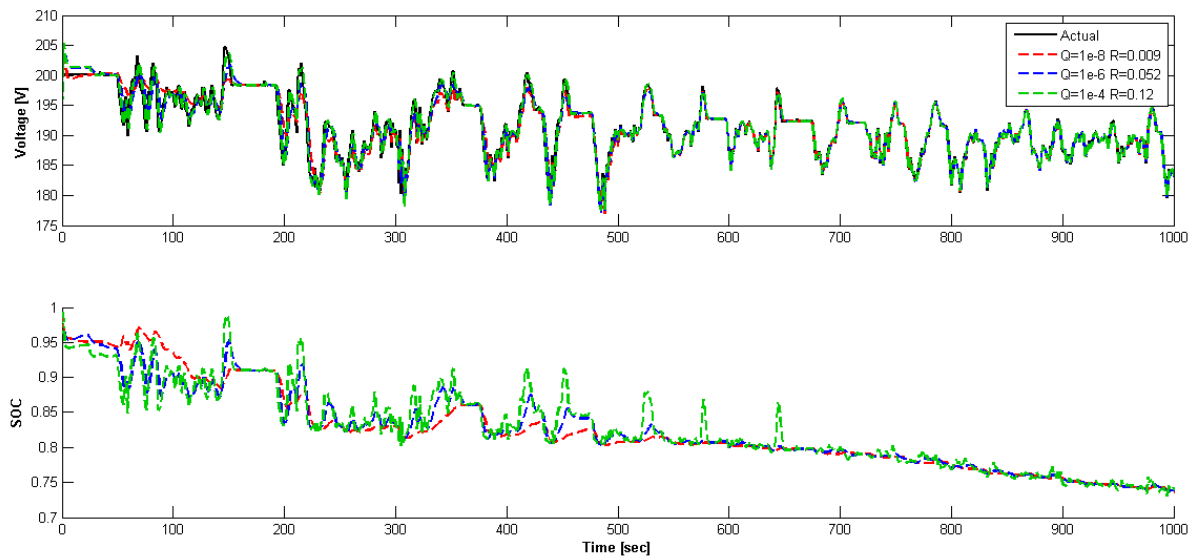


Figure 42. Comparison of SOC estimator performance for three different sets of Q and R values. Voltage and current measurements obtained in digitized form over a CAN Bus i.e. HIL

It is clear that second and third test runs, using higher values of Q and R show faster convergence of the estimator’s predicted to voltage to the actual voltage. However, as expected, the SOC estimate also tends to show higher variation in the initial phase up to ~ 400 s. Beyond 500 s, all three test runs settle to the correct SOC estimate and do not show significant drift. All

three runs show similar performance in this region. The only noteworthy difference is that the third test run clearly appears to show higher variance than the former two.

The above comparison of different weight matrices during the HIL test highlights the need for an adaptive strategy that modifies the SOC estimator's weight matrices based on the battery-systems current temperature and SOC. Adaptive weight matrices allow the filter to compensate for small deviations from the temperature set-point at which the estimator was designed, without having to incorporate thermal effects into the estimator. They also help in accounting for deviations resulting from discrete-time execution, discretized measurements, modeling approximations due to linear interpolation schemes, etc. It is possible to develop a map of the best filter weights for different operating regimes and implement these as Look-Up Tables or correlations on the battery management controller.

The next two chapters illustrate the development of the control oriented thermal model to improve fidelity of system-level simulations and serve as another input to an improved SOC estimator design.

Chapter 4. Battery System Thermal Characterization

The literature has consistently pointed out the safety-critical nature of battery thermal management. Bandhauer et al. [21] present a critical review of thermal issues specific to lithium-ion battery-systems. Further, the lithium nano-structured titanate chemistry has a high charge/discharge power capability resulting in higher heat-generation rates. Giuliano et al. [22] perform an experimental characterization of the heat-generation in li-titanate pouch cells and identify the need for their active thermal-management. This need is further strengthened by the fact the battery-system used in this work will be subjected to frequent, high-power, charge/discharge loads. Lastly, as seen in the previous chapters, temperature has a significant impact on the battery's electrical performance and the models developed in the previous chapter, capture those effects.

Thus, as stated earlier, a primary deliverable of this project was high-fidelity simulation model of the thermal dynamics of the battery-system. As a precursor, a detailed experimental characterization of the thermal dynamics across the battery-system was performed and is presented in this chapter. This was done with a two-fold objective - identifying issues with the system's current architecture; and pin-pointing dominant/critical thermal dynamics, and the best approach to modeling them.

4.1 Battery-System Layout

Figure 43 shows a top-view schematic of the battery-system used in this work. As shown, the cooling-tubes enter the cooling-plate at the top corners and exit at the bottom corners. Each module is arranged such that its terminals are located near the pack-centerline and its heat-sink is located towards the edges of the pack. Between the module heat-sinks and the edges of the pack is a strongly conductive filler material. Note that a module is in thermal contact only with the cooling-plate, and not with adjacent modules. There is an air gap between each module. Thus, heat-transfer is only expected in the lateral direction away from the pack-centerline. However, the cooling-plates are single continuous plates running along the edges of the pack.

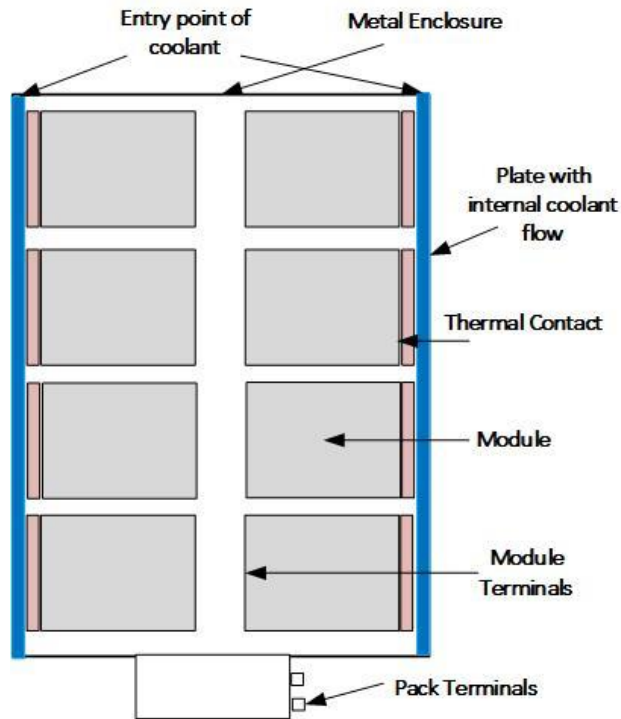


Figure 43. Physical layout of the battery-system

4.2 Test Setup & Plan

Figure 44 details the entire thermal characterization test setup. As discussed earlier, the battery pack is a liquid-cooled system with a pump, fan/radiator, and flow sensor comprising the coolant loop. A thermal insulation was installed to eliminate heat-transfer due to any mechanism other than the convective cooling through the liquid-coolant loop. Electrical load is applied as described in Chapter 2 using the AV900 power-cycling system. An array of seventy DS18B20 temperature sensors is adhered to different parts of the battery-system using a thermally conductive tape and hot-glue. Specifically, the sensors are located near key regions of interest: module terminals, module heat-sinks, and the cooling-plate. These sensors send data to an Easy PIC Pro embedded development board, which acts as a hub and broadcasts data on to a CAN bus. In Figure 44, the red dots represent CAN nodes located on the CAN bus marked in orange. The cooling system uses 50 percent ethylene glycol with water as the coolant which is circulated at a nominal flow-rate of 2 gallon per min whenever the cooling-system is operational. Axiomatic RTD temperature sensors are used to record temperature of the coolant at the battery's inlet and outlet.

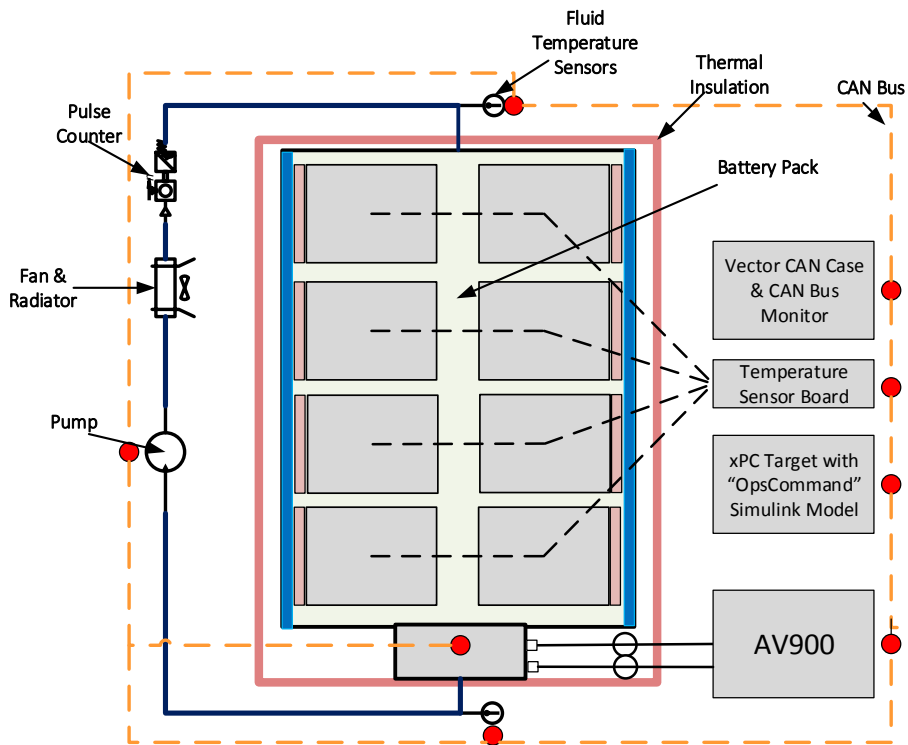


Figure 44. Experimental setup

The test plan consisted of performing of three key tests referred to here as “Pack Cycling”, “Cool-Down”, and “Rest”. In “Pack Cycling”, the battery-system was loaded using the AV900 with a 2C alternating charge-discharge pulse. Coolant was circulated through the system and temperature evolution across the pack was measured. In “Cool-Down”, the system was not loaded, and was allowed to cool down with the coolant being circulated through the system. This chapter presents results and conclusions from the first two tests.

In “Rest”, the insulated pack was first loaded for a short duration and then allowed to settle for a prolonged period of time, to reach a steady-state temperature distribution. Temperature evolution was observed in the prolonged period of settling down. This enabled understanding of the unforced thermal dynamics of the system. Analysis of the third test is presented as part of Chapter 5.

4.3 Pack Cycling Test

This test involved loading the fully insulated battery-pack with a 2 min time-period, square wave type current signal of 2C amplitude as shown in Figure 45. Fifteen counts of this square wave were applied to the pack through a test that lasted 30 min. During this test, the cooling-system was operated nominally. Data from all sensor was recorded. The results from the data

analysis helped characterize the behavior of the pack, and provided a strong basis for some of the assumptions that have been made in developing the thermal model of the following chapter.

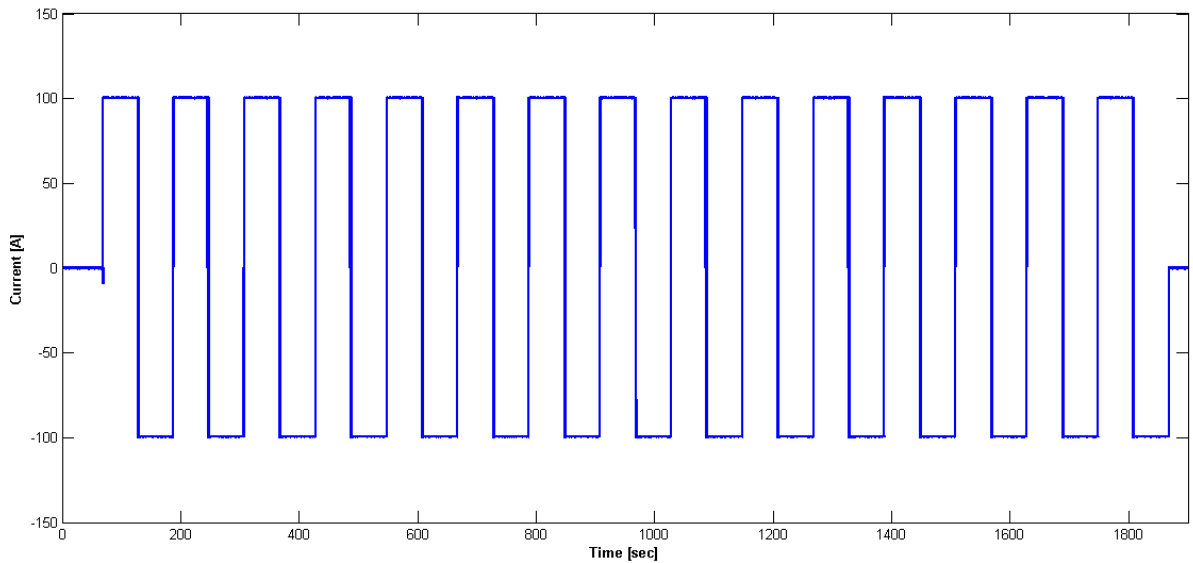


Figure 45. Load Profile used for Thermal Characterization Testing

Spatial Distribution of temperatures across the Pack

Figure 46 is a top-view representation of the pack with a spatial distribution of temperature rise overlaid upon it. Temperature rise is the temperature difference recorded by each sensor, between start and end of the test.

Note that DS18B20 sensors used to measure temperature gave measurements of their mounting points only, and not a spatial distribution. These sample points were then subjected to a 2-D Cubic Spline interpolation to generate the distribution seen in Figure 46.

Further, note that while the plot shows a continuous temperature distribution, a direct thermal contact between adjacent modules does not exist. Thus conductive heat-transfer set up by these gradients can only exist in the lateral direction from the centerline toward either edge within the individual modules.

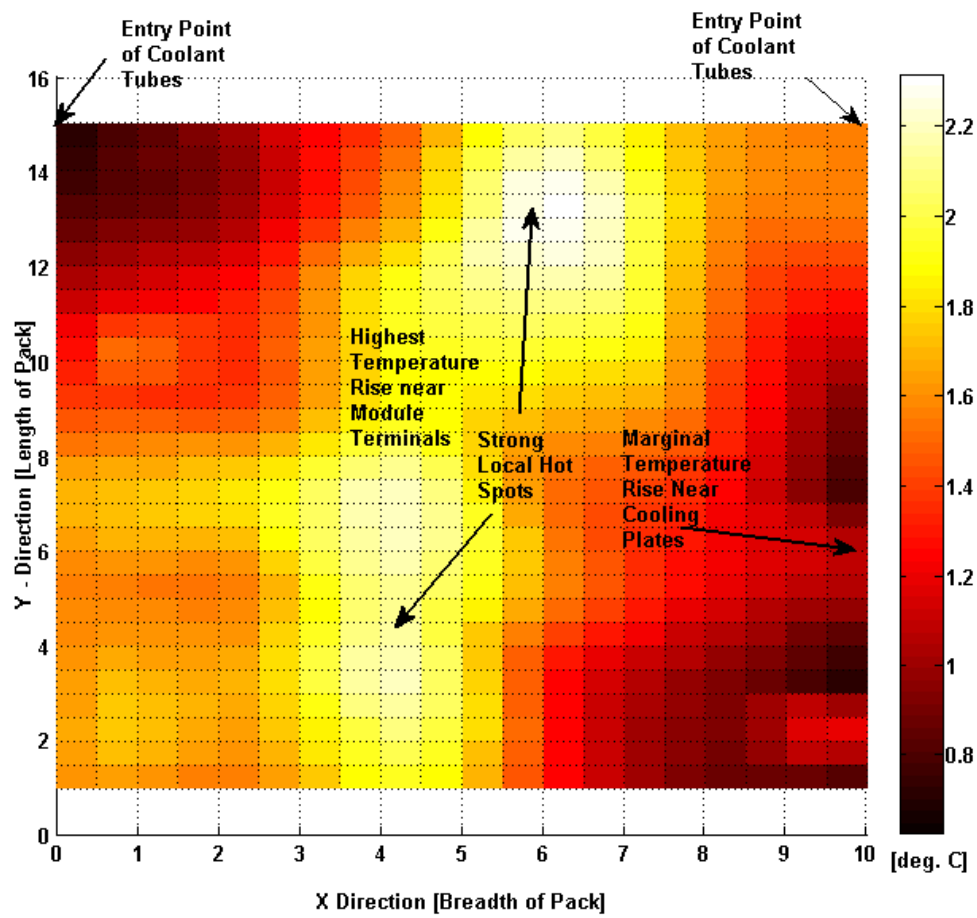


Figure 46. Spatial distribution of temperature rise between start and end Pack Cycling Test

Several key observations can be made from Figure 46. Temperature rise is highest (~ 2.2 °C) along the centerline of the pack. This indicates that a strong heat-source is located in this region. This is expected as both electrical module terminals, are located along the centerline of the pack and it is known that terminals of prismatic pouch-cells typically are the primary heat producing regions.

The lowest temperature rise is near the edges of the pack indicating that any heat conduction into this region is being nullified by heat extraction by the coolant, from the cooling-plate. However, there is a noticeable gradient in temperature rise, along the length of the pack. The least temperature rise occurs at the top corners of the image and increases downwards along the edges. The top corners are the zones where the coolant enters the cooling-plates and is at its lowest temperature and head-loss. Thus, the heat extraction is expected to be strongest here. Hence, the fact that this region has lowest temperature rise, is expected.

In keeping with the above observation, the highest temperature rise (and thus, the most adverse hot-spot formation) occurs near the lower part of the graph along the centerline. This is

the region nearest to the module terminals and farthest away from the entry of the coolant into the battery pack. All of these observations point to the need to account for different dynamics of the modules, instead of lumping the entire pack together.

Figure 47, shows surface plots of the temperature distribution across the pack at the start of the test and at the end of the test. This graph gives important insights into the rate and magnitude of temperature increase in different regions of the pack.

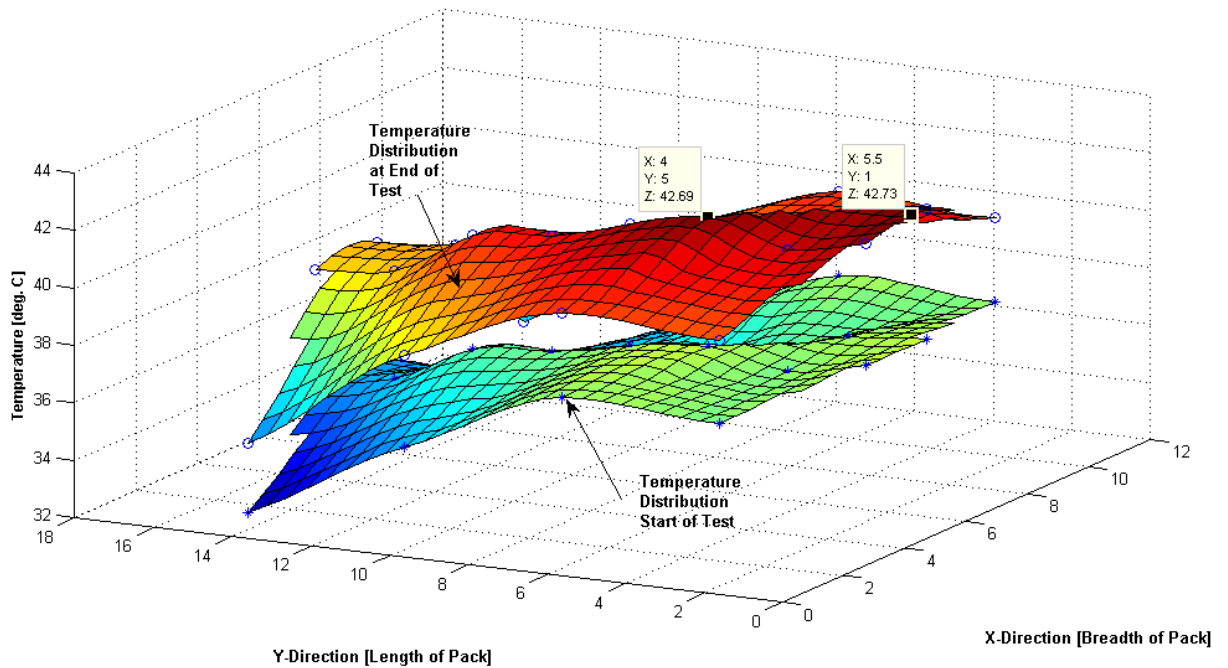


Figure 47. Internal temperature distribution at start and end of Pack Cycling Test

Temporal Evolution of temperatures in Important Regions of Pack

In order to understand the temporal evolution of temperatures in the different regions of the pack, a spatial average of temperature data from different sensors located in a particular region of interest was taken and its time-trace was plotted. This was done for the regions near the module terminals, the region inside the module near the heat-sink, the exterior region of the heat sink, the cooling-plate, and the coolant. Figure 48 shows the time-traces of these averaged temperatures.

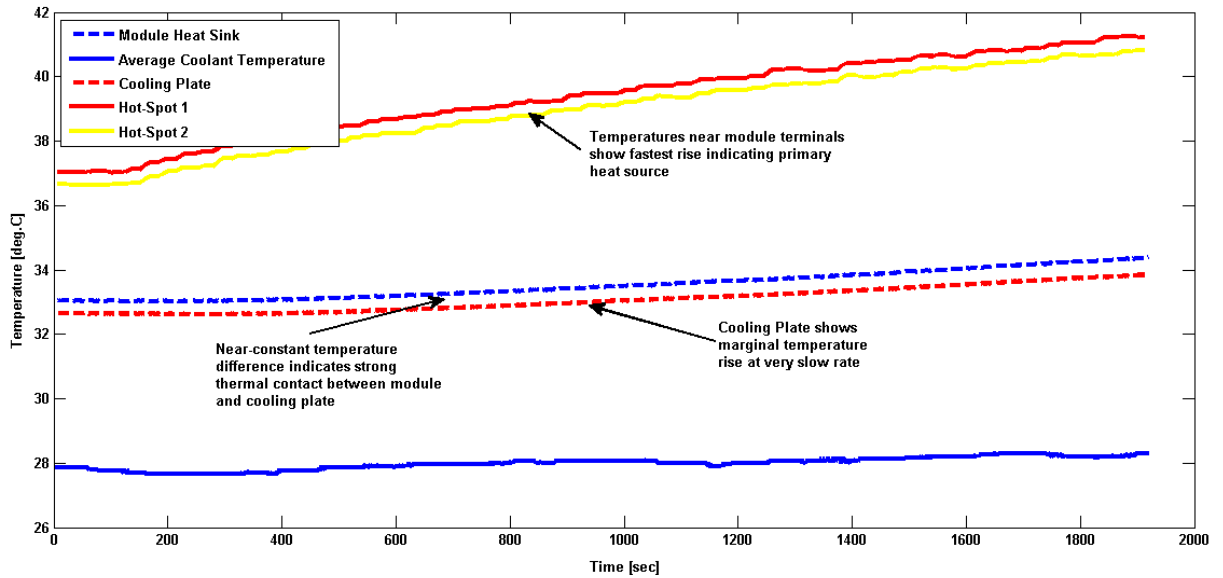


Figure 48. Temperatures in different regions of the battery-system during Pack Cycling Test

As expected, the regions near the module terminal i.e. regions along the pack centerline, showed the fastest rate of temperature increase. This is indicated by Hot-Spot 1 and Hot-Spot 2 in Figure 48.

Notably, that the temperature near the module terminals (i.e. Hot-Spot 1 and Hot Spot 2) rises almost linearly. This immediately confirms the module terminals to be the primary heat sources. It also confirms that the heat generation rate is significantly higher than the heat extraction rate due to conduction, in this region.

Most importantly, the heat-sink and cooling-plate regions show a much more gradual rate of temperature increase and a final temperature rise of ~ 1.4 °C. Figure 49 below shows a magnified version of the traces of average cooling-plate and heat-sink temperatures. Note the slight drop in heat-sink and cooling-plate temperatures in the first 200 s. There is a delay of approximately 400 s between start of the test and when the temperature of the cooling-plate starts to increase.

This points to a few key conclusions. Firstly, there is no heat-source in the immediate vicinity of the cooling-plates. Secondly, there appears to be a delay of ~ 7 min before the heat generated near the module terminals appears at the cooling-plate. This also indicates that the response-time of any thermal control action will always be greater than ~ 7 min, which is a critical thermal-management concern.

Note that the rise in temperature at the cooling-plate is relatively small, due to a strong heat extraction by convective heat-transfer to the coolant. Further, there is a nearly constant

temperature difference between the heat-sink and cooling-plate region which indicates strong conduction between the two regions. This is attributed to the fact that these regions are plates of aluminum in thermal contact with each other through highly conductive filling materials, thus validating the efficacy of the filling material.

Lastly, the average coolant temperature shows a marginal increase during the test. This indicates that the radiator system unable to extract sufficient heat from the cooling-system. While the temperature increase is only marginal in this experiment, it is expected to be significant during longer operations and may also be a cause for concern.

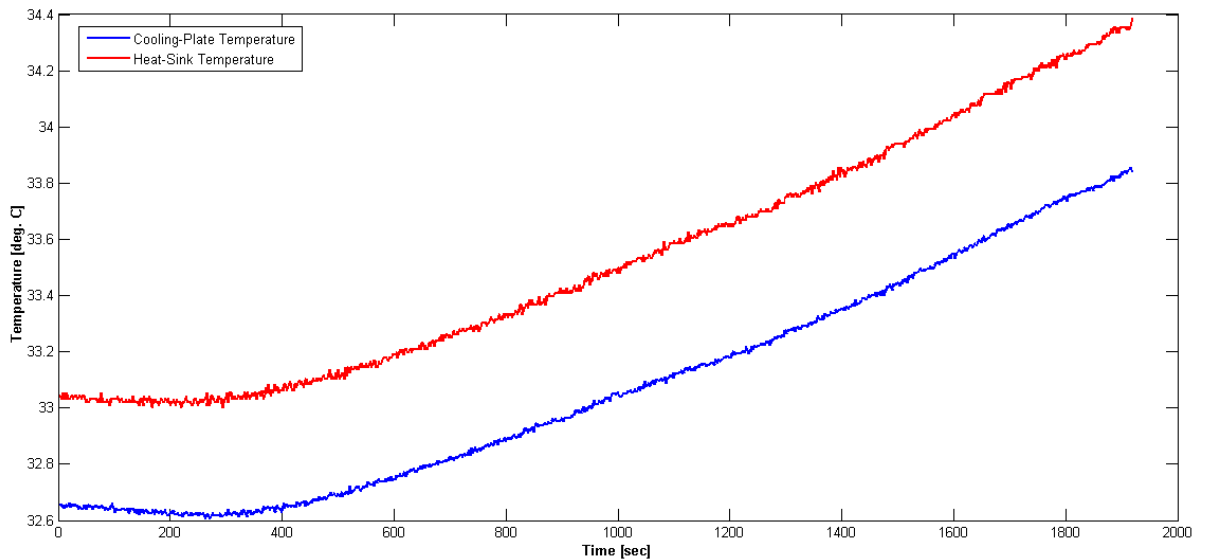


Figure 49. Evolution of heat-sink and cooling-plate region temperatures

This validates the observation that no heat-source is located in the vicinity of the cooling plate and that the dynamics of heat transfer from the hot-spots to the cooling plate are very sluggish.

4.4 Cool-Down Test

The fully insulated battery pack is first cycled for a ~5 min duration and then allowed to cool with coolant circulating in the system. The cooling-system is operated at a steady flow-rate of 2 gpm. Data recording is only started at the instant when cycling is stopped and continues for approximately 2400 s, or 40 min. As before, data from all sensors was recorded.

The primary objective of this test was to observe and capture the temperature and heat-transfer dynamics during the cool-down process. The dynamics of the cool-down process were a key factor in determining the best approach to developing the model. It was also important for

validating the efficacy of the existing cooling-system design. Analysis of the test data brought forth several important insights that were not intuitively obvious and heavily influenced the approach used to model the pack's thermal behavior

Spatial Distribution of Temperature cross the Pack

Figure 50 shows the spatial distribution of the temperature drop during the cool-down process. Several inferences can be derived from studying these spatial distributions, as described in the following section. Analogous to Figure 46, the surface plot has been generated using 2-D Cubic Spline Interpolation on the data obtained from the temperature sensor array.

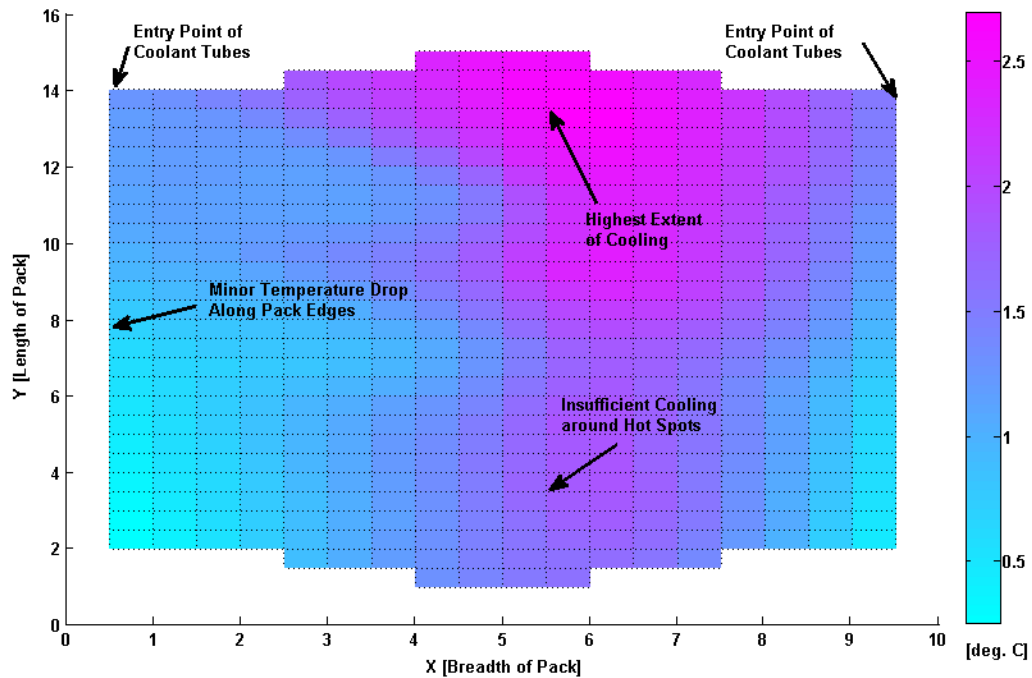


Figure 50. Spatial distribution of temperature drop during Cool-Down Test

It is clear from the above that the drop in temperature is the least near the edges of the pack closest to the cooling-system/cooling-plates. This is expected because the temperature rise in this region, during battery cycling, is much less than in other parts of the pack. Further, the drop in temperature decreases as we move lower along the edges. This is once again indicative of a reduced cooling effect in these regions, which needs to be modeled accurately.

The cooling system extracts heat from the region of the pack closer to the entry-point of the cooling tubes more effectively than from regions farther away. Most noteworthy is the difference in temperature drops between different locations on the battery pack centerline. The region along the pack centerline, but closer to entry point of cooling-tubes, shows a much higher temperature drop ($\sim 2.5\text{ }^{\circ}\text{C}$ in 40 min) as compared to points along the centerline, farther away from the cooling-tube entry point.

Thus, the extent of cool-down appears to be the lowest near the hot-spots farthest away from the entry point of the cooling tubes ($\sim 0.5\text{ }^{\circ}\text{C}$ in 40 min). This is a cause for concern during prolonged operation of the pack in urban environments, where small bursts of aggressive charging and discharging are expected, with very little cool-down time in between.

As completed for the first phase of the test, the temperature distributions are represented as a surface plot. In Figure 51, the upper surface shows the distribution at the start of the test and the lower surface shows the distribution at the end of the test.

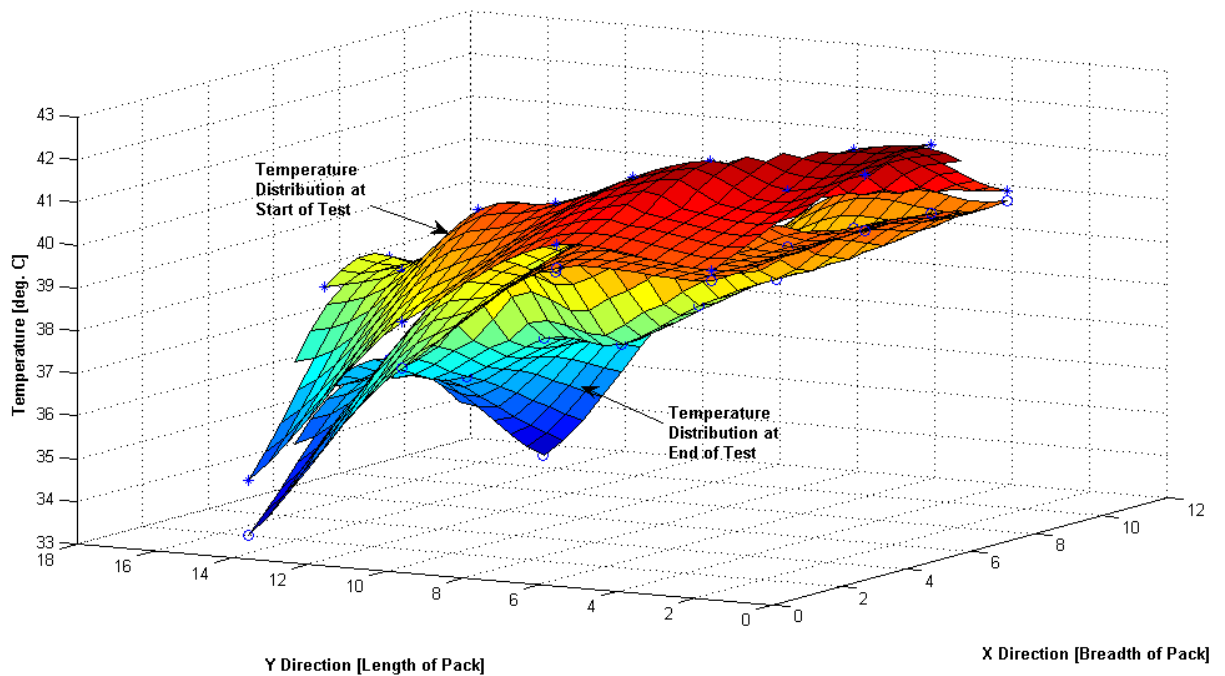


Figure 51. Temperature distributions at start and end of Cool Down Test

Temporal Evolution of temperature in Important Regions of the Pack

Analogous to Figure 48, a spatial average of temperature data from multiple sensors located in a particular region of the pack was taken and time trace was plotted, as shown in Figure 52

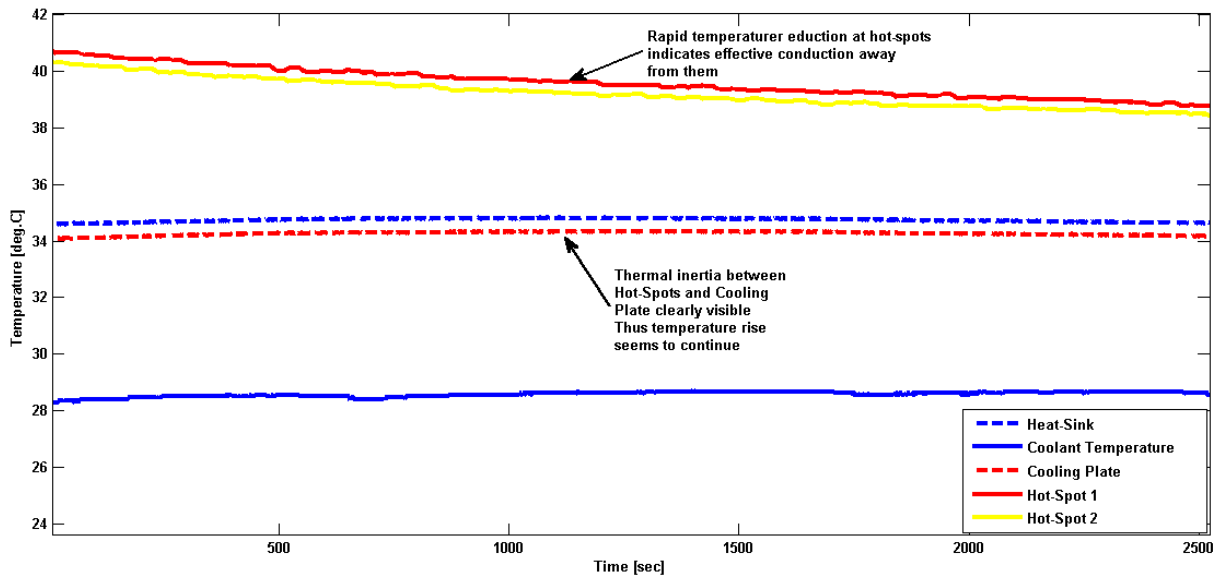


Figure 52. temperatures in different regions during Pack Cool Down

The region near the module terminals immediately shows decreasing temperatures as soon as cycling of the battery pack has been stopped. This is expected since the only heat-source here is heat-generation from the battery. During cooling, conduction from this region to the heat-sinks is predominant. Note that the temperature decreases faster initially and the rate reduces with time.

Another noteworthy observation is the temperatures of the heat-sink and cooling-plate continue to rise for nearly 15 min even after cycling has been stopped. This is due to heat conduction into this region, from module terminals. Owing to the architecture of the pack, this heat-conduction appears to be “delayed”. This conduction gradually subsides as the temperature of the hot-spots drop, heat extraction by the coolant starting dominating, and then actual cool-down of the cooling-plate begins. This observation points to a high thermal inertia and sluggish temperature response dynamics which were observed during the “Pack Cycling” tests as well. This phenomenon is clearly illustrated by the temperature traces in Figure 53.

It was critical to capture all the phenomenon discussed above in the thermal model of the battery system, so as to ensure sufficient fidelity. From the perspective of using the model as a basis for thermal management system trade-off studies and control-design, it was especially important to capture the system’s inherent thermal inertia and sluggish dynamics.

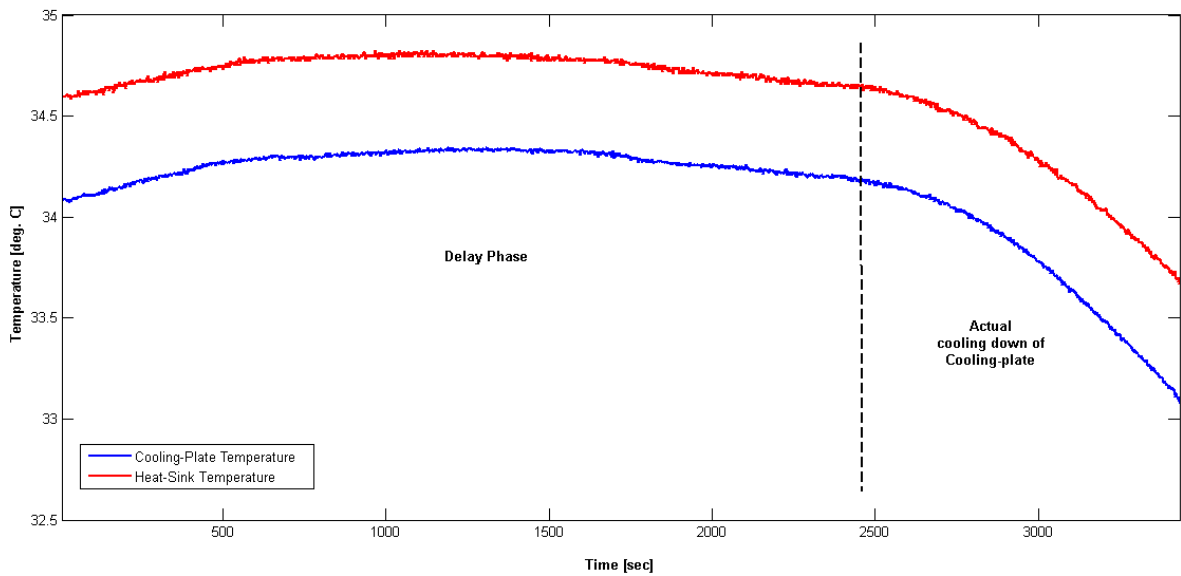


Figure 53. Temperature traces showing delayed on-set of cooling at Cooling-Plate

4.5 Measuring Convective Heat Transfer Coefficient

A key physical parameter affecting the performance of the battery pack and cooling-system is the convective heat-transfer coefficient between the cooling-plate and coolant. It was extremely important to measure and validate the expected value of this parameter to quantify efficacy of the cooling-system. Further, it was important to reliably establish this value, as it would be an important parameter in any modeling effort.

The most accurate way of calculating this parameter from measured data was to quantify heat extracted from the battery-system. This was done using temperature traces of the coolant at the battery-inlet and outlet. These measurements can be seen in Figure 54. Note that the temperature measurements appear to be in steps due to the 0.1 °C resolution of the RTD temperature Scanners used to measure temperature of the coolant.

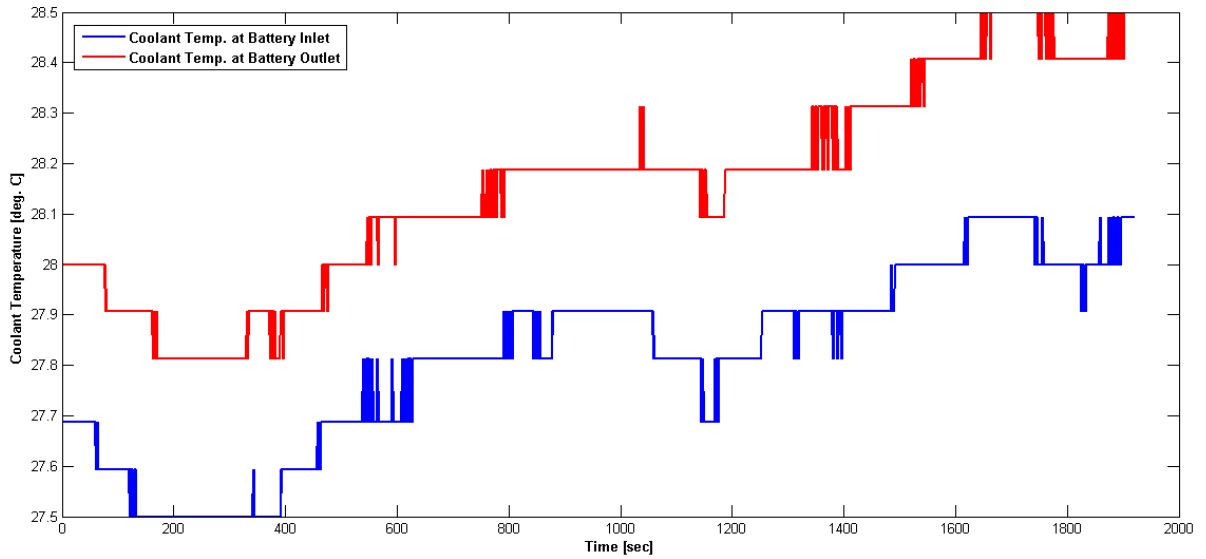


Figure 54. Coolant temperature at battery pack inlet and outlet during a Pack Cycling Test

The difference in coolant temperature between battery outlet and inlet, along with the nominal flow-rate of 2 gpm, and the specific heat capacity of 50 percent ethylene glycol with water was used to obtain the heat energy extracted by the cooling system per unit time.

Figure 55 shows a plot of the heat energy generated, extracted, and absorbed, per unit-time. The variations in the plot below are due to the jumps seen in Figure 54 due to the resolution of the temperature sensors. These jumps are amplified in the process of calculating power from the temperature measurements.

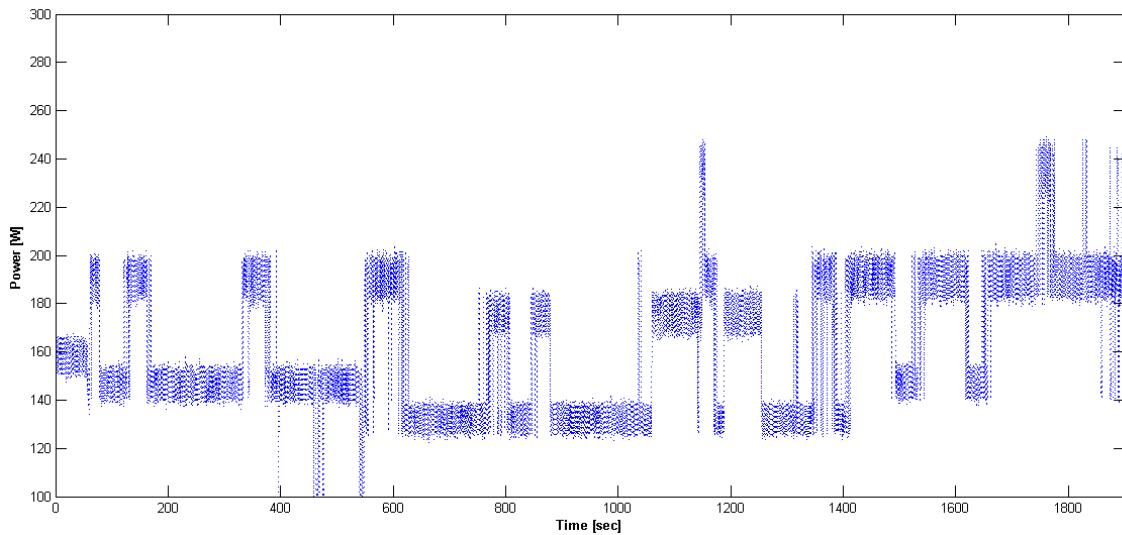


Figure 55. Comparison of thermal power generated, extracted, and absorbed during Pack Cycling Test

Using the trace of the heat extracted per unit-time from the above figure, the temperatures of the coolant, and those of the cooling-plate at the entry and exit of the coolant, and information about the geometrical construction of the cooling tubes, the value of convective heat-transfer coefficient was extracted. The following equation was used for this computation:

$$h_{conv} = \frac{\rho \cdot f \cdot Cp \cdot (T_{out} - T_{in})}{A_s T_{LMTD}} \text{ where } T_{LMTD} = \frac{\Delta T_o - \Delta T_i}{\ln\left(\frac{\Delta T_o}{\Delta T_i}\right)}$$

ρ – Coolant Density

f – Coolant Flow Rate

Cp – Coolant Heat Capacity

$(T_{out} - T_{in})$ – Coolant temperature Rise

A_s – Area of heat-exchange

T_{LMTD} is the log-mean temperature Difference (LMTD). Here, the terms ΔT_o and ΔT_i are the differences in temperature between the coolant and the cooling-plate, at the battery-system outlet and inlet respectively. This is the standard equation for modeling and computing heat transfer from a fluid from the walls of a heat exchangers. An important caveat is that this equation and the LMTD approach is only applicable in steady-state. In this specific case, note that the cooling-plate temperature undergoes a very minor increase over the 30 min duration of the test. The dynamics of the heat-transfer from the cooling-plate to the coolant are much faster than those of evolution of the cooling-plate temperature. Thus, the heat-transfer to the coolant can be approximated as nearly steady-state and this approach can be applied.

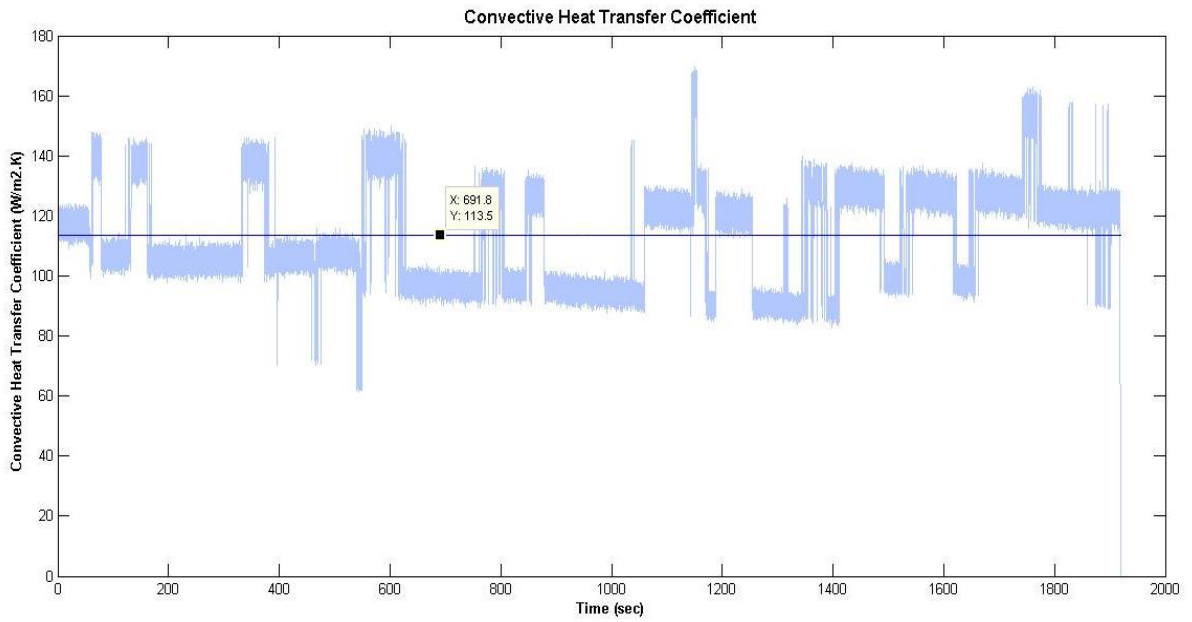


Figure 56. Heat Transfer Coefficient

Figure 56 above represents the convective heat-transfer coefficient vs. time. As before, the variation is introduced due to the characteristics of the temperature sensors used and the fact that online filtering of the sensed temperature data was not performed during the test.

The nominal value of the convective heat-transfer coefficient, at a flow-rate of 2gpm, is 113.5 W/m²K. This value is used in the model development described in Chapter 5, along with the insights and conclusions derived from the thermal characterization illustrated in this chapter.

Chapter 5. Battery System Thermal Model

The goal of the model is to capture all heat-transfer dynamics within the pack through a first-principles model simulate the measured temperature dynamics with a high level of fidelity. Note that this model was developed with the objective of coupling with the electrical model developed in Chapter 2, for use in system-level or full-vehicle simulations. It was also developed to form a basis for evaluating different cooling-system configurations and for thermal management control-system design. The extensive thermal characterization of the battery-system, illustrated in the previous chapter, is leveraged in developing this model.

5.1 Modeling Heat Generation

Based on the observations and analysis of spatial distribution and temporal evolution of temperatures during pack-cycling, and cool-down, it is clear that the region near module terminals is the primary heat-source within the system. This is expected since this is the regions where all terminals of the cells within each module are connected together. Recent work by Murashko et al. [23] on 3-D thermal modeling of a li-ion pouch experimentally demonstrates that majority of the heat generation takes place at the pouch cell terminals where the current emerging from a flat electrode converges into a small electrode terminal. The modules are essentially a stack of pouch cells connected in series, and thus, the region near the module terminals is the primary heat-source. This is indicated in the Figure 57.

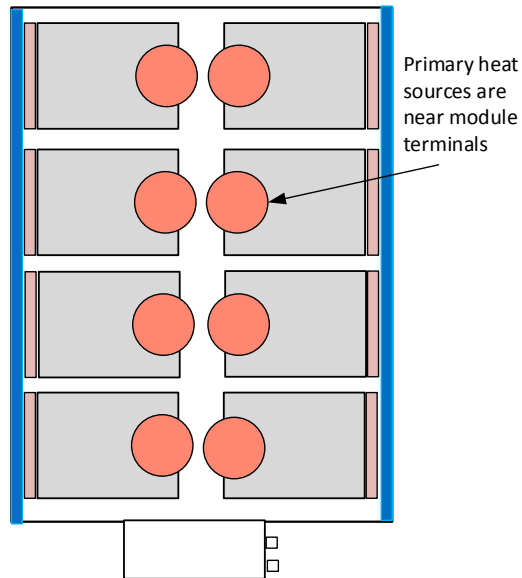


Figure 57. Location of heat-sources as concluded from thermal characterization

Heat energy balance in a Li-ion battery was originally formulated by Bernardi et al. [24]. Over the years, the literature has extensively used a simplified formulation of that energy balance formulation, expressed as the following equation. Most article in the literature, and those cited in this work, use this form of the energy balance equation as the basic starting point owing to its simplified form and adequate match with experimental data [25].

$$Q_{gen} = I^2 ESR - IT \frac{dOCV}{dT}$$

Specifically, Giuliano et al. [22] have demonstrated the validity of this equation to determine heat-generation rate for a stack of li-titanate pouch cells. While the cell-chemistry involved in that work is not identical to the one used by Giuliano et al., it provides a strong basis to use this heat-generation model here.

The reversible, entropic heat component of the heat-generation rate can be evaluated using current, pack temperature at the present time-instant, and a Look-Up Table of the $dOCV/dT$ w.r.t. SOC and temperature. The Look-Up Table was obtained from the OCV vs. SOC vs. temperature plot shows in Figure 8 in Chapter 2.

The irreversible heat-loss, due to polarization and Series resistance of terminals, bus-bars, etc. is calculated using equivalent series resistance (ESR) of the battery system, w.r.t. SOC and temperature. Murashko et al. [23] demonstrate the additional fidelity in modeling heat-generation, achieved by accounting for ESR variations with SOC and temperature. This approach was thus used, leveraging the experimental data obtained in this work.

The ESR map is generated from the HPPC test data discussed in Chapter 1. From the test data, it was apparent that ESR values for charge and discharge were different. Thus, two maps i.e. ESR Charge and ESR Discharge w.r.t. SOC and temperature were developed. These were calculated by using the standard definition of ESR as per the US DOE Battery Test Manual for Plug-In Hybrid Electric Vehicles [10]. The model of heat-generation is implemented in Simulink as shown in Figure 58.

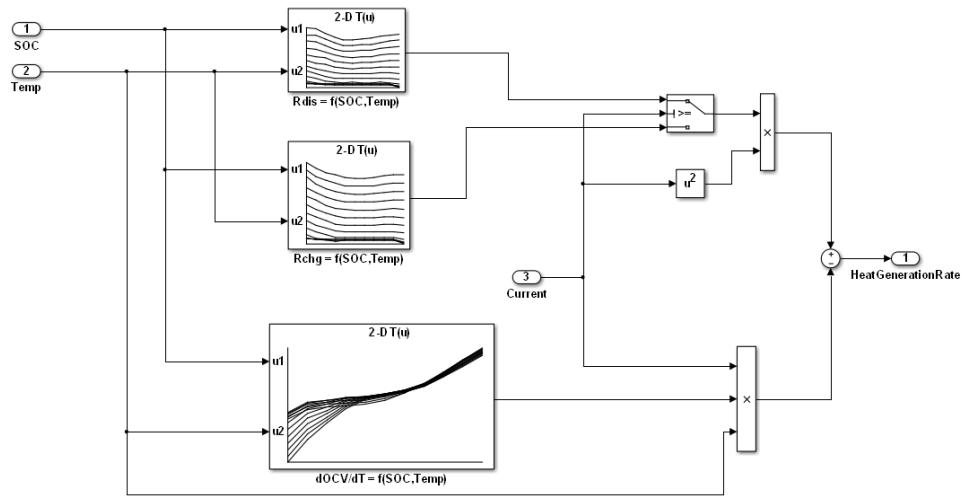


Figure 58. Simulink implementation of heat-generation model

5.2 Modeling the Heat-Transfer Dynamics

While the heat-transfer across the battery-system is a transient process, transient models are numerically complex and involve parameters which cannot be estimated readily from real test-data. Thus, very often, transient heat-transfer dynamics are often captured using lumped capacitance models.

Lumped capacitance models are only valid under certain conditions on the configuration's Biot Number. Without complete knowledge of the materials used in the module construction, accurately determining Biot Number proved difficult. Another approach to evaluate validity of a lumped capacitance model was considered. Specifically, a lumped capacitance model can be used if time-constants associated with the "lumps" are much faster than those associated with the heat-transfer between the lumps.

A test was run where the insulated battery pack was cycled without the cooling system on, and then left till it reached a thermal steady-state, without the action of the cooling system. Temperature evolution of a single module terminal and its corresponding cooling-plate location was analyzed. From Figure 59 it is clear from both the module-terminal and cooling-plate temperature traces, that a first-order response curve can be fit to these traces with high accuracy. This response is characteristic of a two-node lumped model with conduction heat-transfer between the two nodes and accurate models the heat-transfer within a single module.

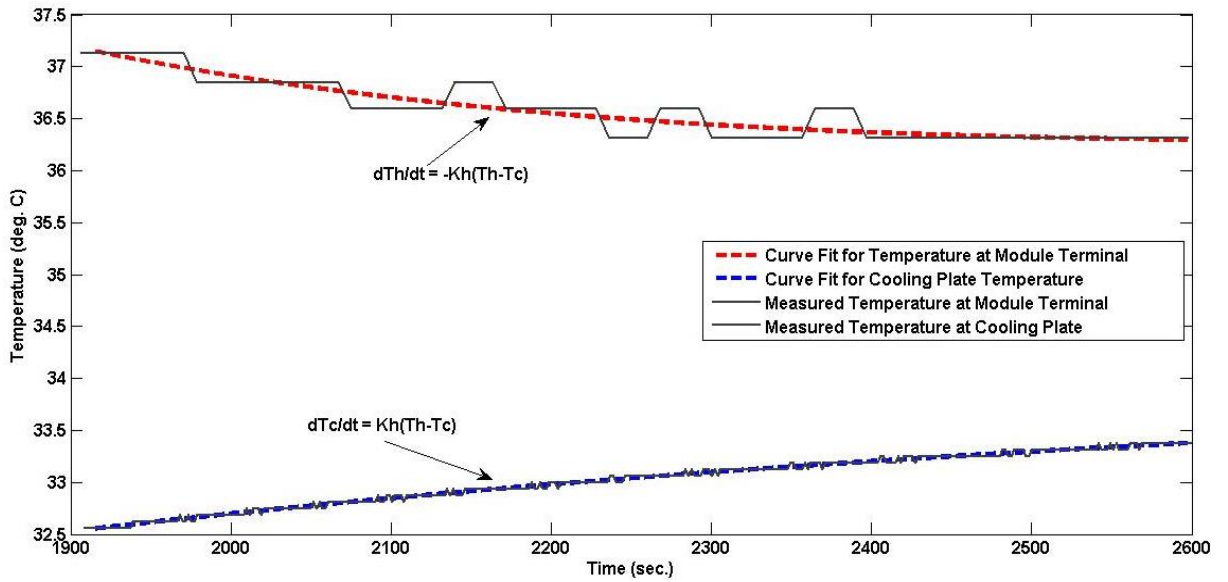


Figure 59. temperature response of Module Terminal and Cooling Plate during unforced cooling

Thus the following differential equations represent these first-order responses.

$$\frac{dT_c}{dt} = (T_h - T_c) \frac{Kc}{Cap_c}$$

$$\frac{dT_h}{dt} = -(T_h - T_c) \frac{Kh}{Cap_h}$$

Thus, a single module can be modeled as a lumped-capacitance model, with one node located at the module terminals, and the other located at the corresponding cooling-plate, with conduction as the only mode of heat-transfer between them

Now, this lumped-capacitance model can be further augmented with two additional components. Heat generated at the module terminals is essentially internal heat-generation within the first lump. Further, at the cooling plate, heat is extracted by convective heat-transfer to the coolant. As observed Chapter 4, evolution of temperatures at the cooling-plate are orders of magnitude slower compared to those of heat-transfer to the coolant. Thus the heat-transfer to the coolant can be treated as a steady-state process, with a constant wall temperature heat-exchange. Figure 60 shows a schematic of the heat-transfer for a single module.

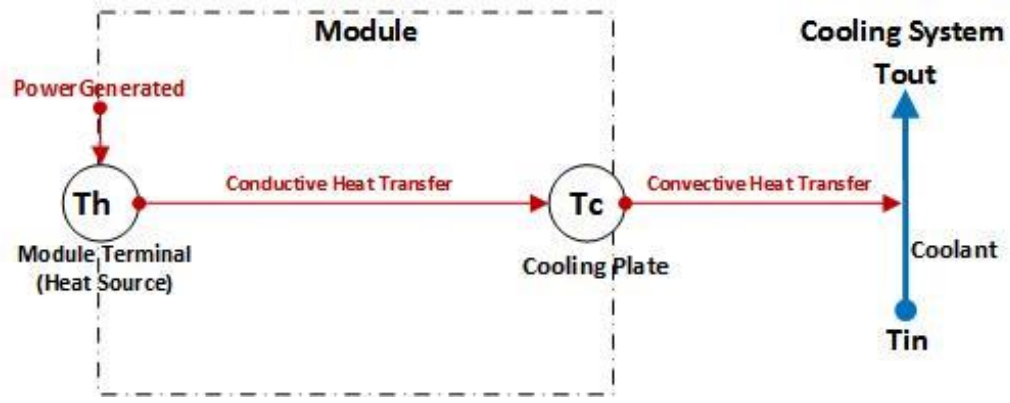


Figure 60. Lumped-Node Thermal Model of a Single Module

Thus, the governing equations for this model are as shown below:

$$\dot{Q}_{gen} = I^2 ESR - IT \frac{dOCV}{dT}$$

$$\frac{dT_h}{dt} = \frac{\dot{Q}_{gen}}{Cap_H} - (T_h - T_c)K_H$$

$$\frac{dT_c}{dt} = (T_h - T_c)K_C - \frac{\dot{Q}_{rem}}{Cap_C}$$

The heat-transfer to the coolant is modeled using the following equations of heat-removal from walls of an internal channel, at steady-state:

$$(T_c - T_{out}) = (T_c - T_{in}) e^{\left(\frac{-h_{conv}As}{\rho C_p f}\right)}$$

$$\dot{Q}_{removed} = h_{conv}As(T_{out} - T_{in})$$

T_h and T_c are the temperatures at the module-terminal and cooling-plate region of that module, respectively. These two are the critical temperatures that need to be modeled. This is because the module-terminal is a critical hot-spot, and the cooling-plate region affects heat-extraction from the battery-system. An average value of these can be used as the nominal temperature of the module.

\dot{Q}_{gen} is the heat-generated per unit-time by the respective module. \dot{Q}_{rem} is the heat extracted per unit-time by the coolant from a single module. K_H and K_C are representative of the conduction coefficient between the module-terminal and cooling-plate, normalized by the “local” heat-capacity at the module-terminal and cooling-plate respectively. Cap_H and Cap_C are the “local” heat-capacity terms at the module-terminal and cooling-plate respectively. h_{conv} has a nominal value of 113.5 W/m²K as established in the previous chapter. As is the heat-exchange

area within the cooling-plate. ρ , C_p , and f are the coolant's density, specific heat-capacity, and flow-rate, respectively.

From the characterization described in Chapter 4, it is clear that a thermal gradient exists along the cooling-plate. It is also evident that heat-extraction by the coolant is not uniform along the length of the pack, but decreases as the coolant travels further away from its entry point. This phenomenon can be captured by modeling coolant-flow through the entire cooling tube, along with its different thermal interactions along the way.

Note that heat-transfer dynamics are symmetric w.r.t. centerline of the pack. Thus it is possible to capture all relevant effects by only modeling one half of the pack. Figure 61 is a schematic illustrating this model.

The cooling-plate is divided into four different regions, each having a uniform temperature. The interaction of the coolant with each region is modeled as steady state internal flow with a constant wall-temperature boundary condition. This model seems to be a valid approximation as justified earlier. Temperature of coolant at the outlet of one region is used for the inlet of the next, thereby capturing the decreasing heat-extraction effect.

This schematic forms the basis of the model used to simulate the heat-transfer dynamics at the pack-level.

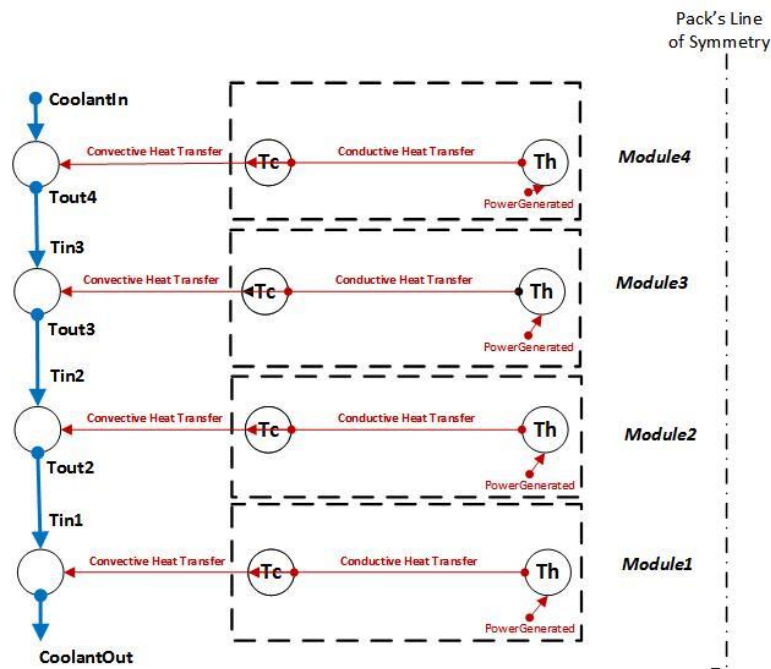


Figure 61. Battery-Pack level thermal model

5.3 Simulink Model and Parameter Estimation

For each module, and its interaction with the coolant, four parameters, namely K_C , K_H , Cap_C , and Cap_H must be known for accurate modeling and simulation. Thus a total of 16 parameters were needed to be evaluated. To do this, the model was implemented in Simulink and parameter estimation was performed using empirical data sets.

Simulink Model

Figure 62 shows an overview of the thermal model. It has three sub-systems, namely the Cooling System, the Heat-Generation sub-system, and the Battery Pack. The model uses measured data-traces of current, coolant input temperature, and SOC, as inputs. It provides time-traces of the coolant output temperature, and temperatures of the module-terminal (hot-spots) and cooling-plate regions of each of the four modules considered in the model. The model has to be initialized with initial temperatures of the coolant output and of each of the module-terminal (hot-spot) and cooling-plate regions. Figure 63 through Figure 66 show detailed implementations of each subsystem of the model.

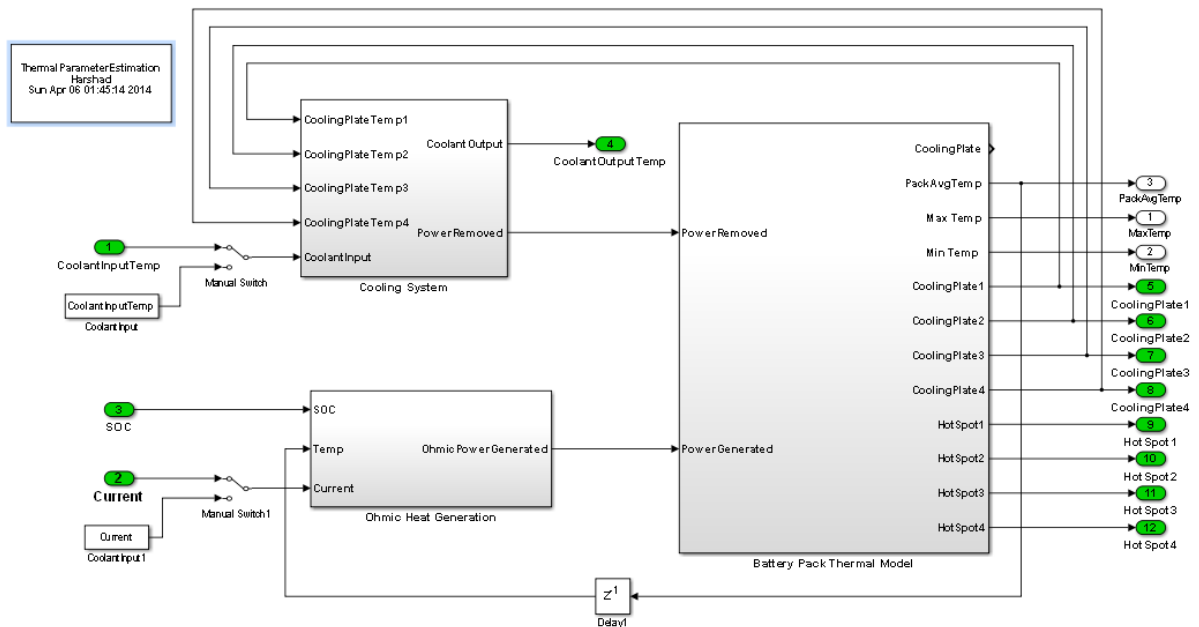


Figure 62. Overview of the thermal model setup for parameter estimation

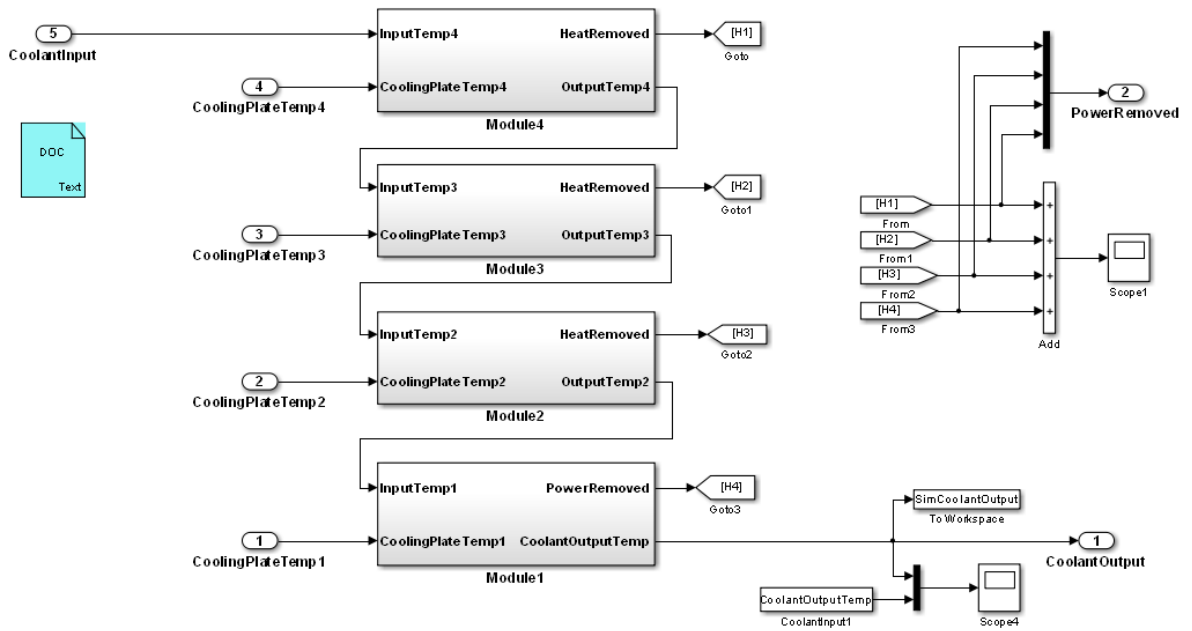


Figure 63. Model of heat-exchange between the 4 four regions of cooling-plate, and coolant

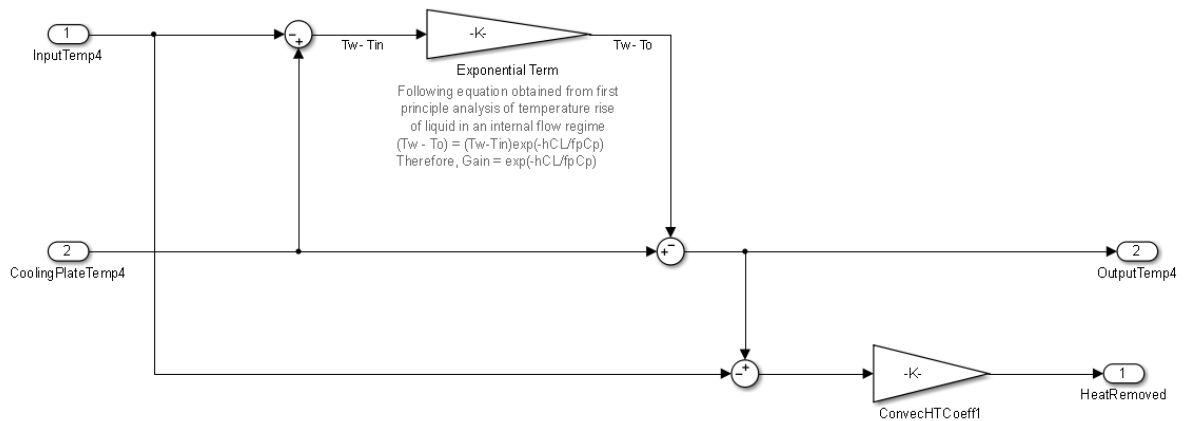


Figure 64. Model of heat-exchange to coolant, in an internal flow with constant wall temperature

with the Sum Squared Error of the simulated and measured temperatures as the Cost Function. The Trust-Region technique, built into the *lsqnonlin* function in Simulink [11], was used to solve the minimization problem.

As stated earlier, a total of 16 parameters had to be estimated. Further, owing to slow speed of thermal dynamics, each data-set was nearly 40 min long. This collectively resulted in a slow estimation process. To resolve this issue, MATLAB’s Parallel Computing Toolbox was used to parallelize the estimation process. This tool speeds up the estimation process by reducing the time taken to evaluate the Trust Region. This is done by concurrently executing multiple simulations during each estimation iteration, on the multiple parallel MATLAB “workers” [26].

Figure 67 shows the measured and simulated temperature response of the module-terminal and cooling-plate region for one of the four modules. It also shows the evolution of the Cost Function. This particular estimation task takes 35 iterations to complete. The estimation is terminated when the change in the Cost Function is under 0.1 percent.

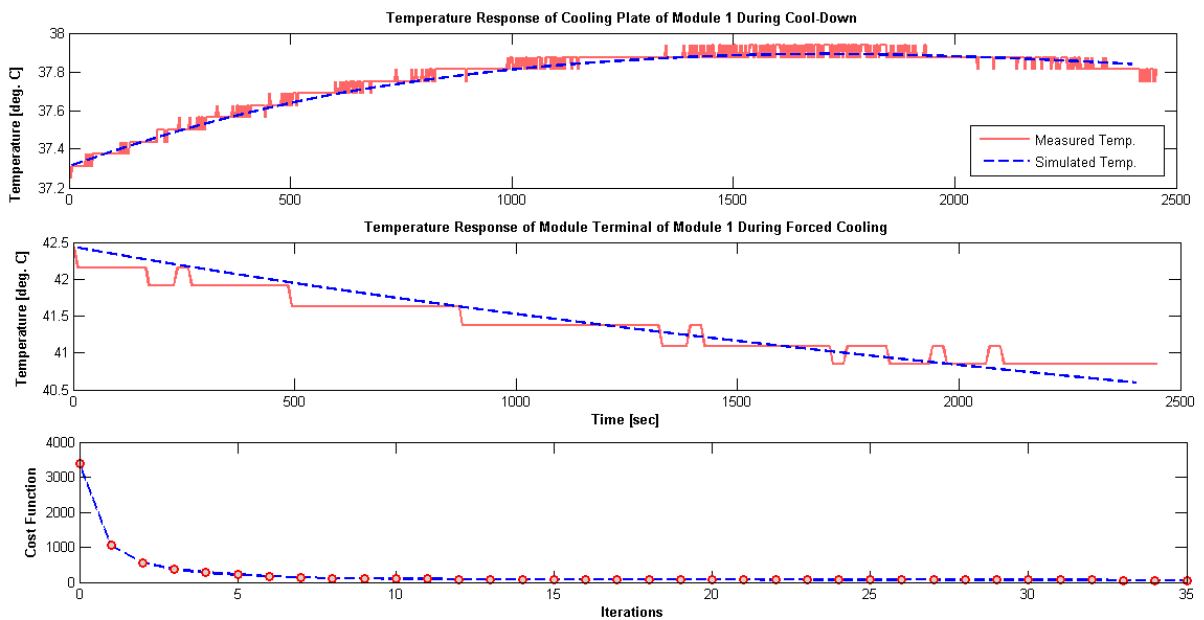


Figure 67. Sample temperature traces and Cost Function from one of the parameter estimation tasks

5.4 Model Validation

The model is validated against test-data recorded during the experiments. To do this, current, SOC, and coolant input temperature profiles recorded during the experiments were used as inputs. The model simulated the evolution of temperatures at all critical locations. The simulated profile was plotted against the measured temperature profile.

The follow are some comparative plots. Figure 68 shows a comparison of the measured and simulated temperature response during the transition phase when Pack Cycling is stopped and it undergoes forced-cooling due to the operational cooling-system.

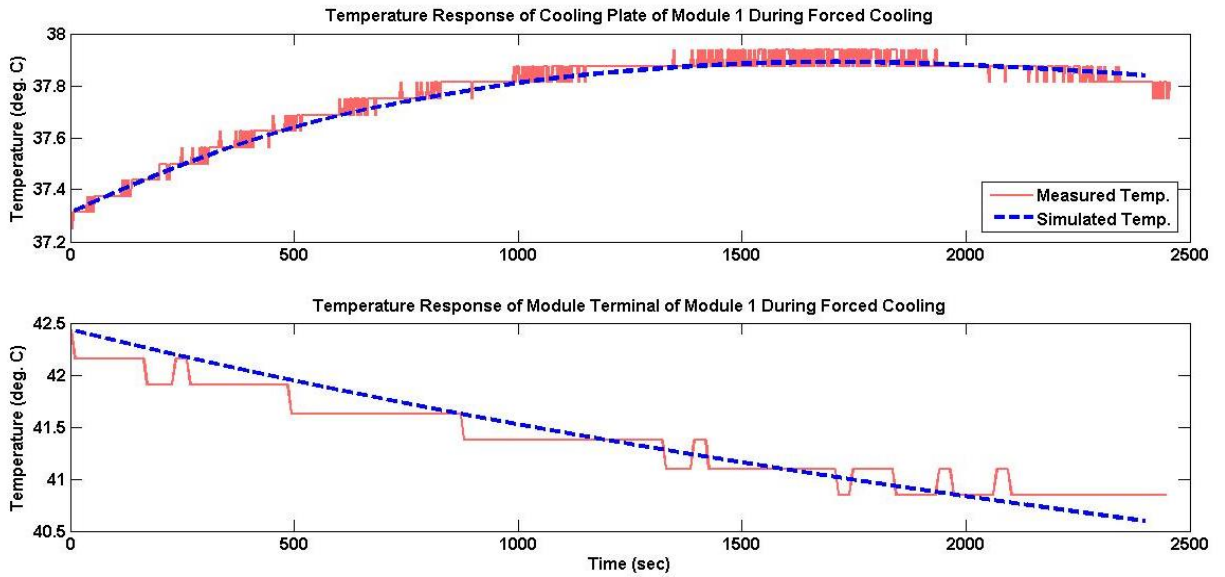


Figure 68. Comparison of Measured and Simulated temperature Responses During Forced Cool-Down

Analogously, the Figure 69 below shows a comparison of measured and simulated temperature response at the module terminal and corresponding cooling plate during Pack Cycling.

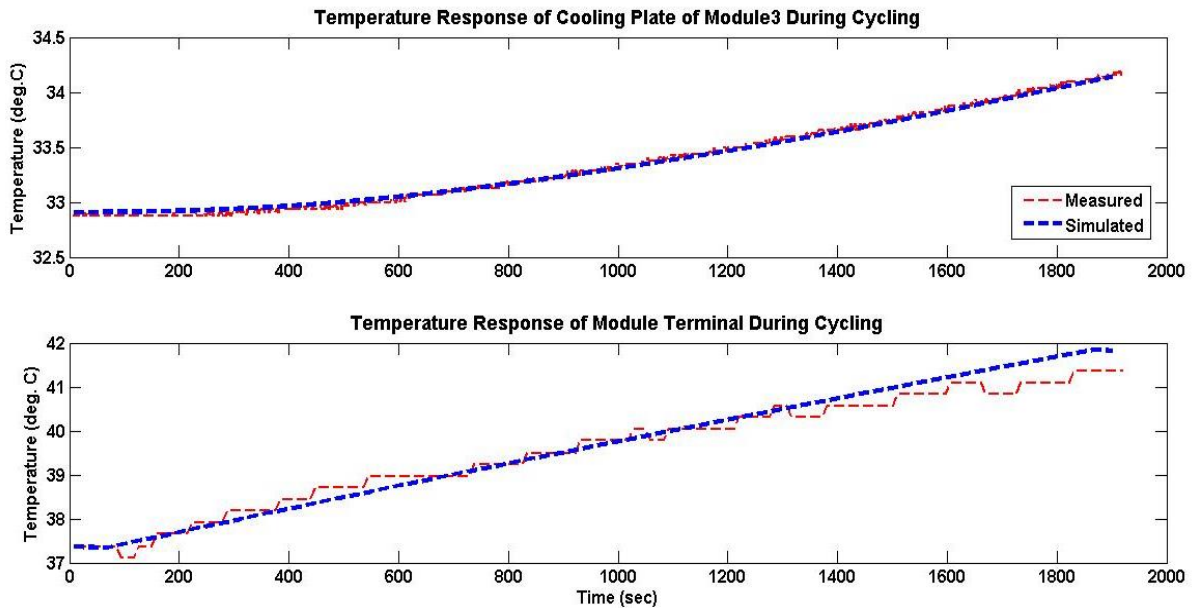


Figure 69. Comparison of measured and simulated temperature response at Module 3 during Pack Cycling

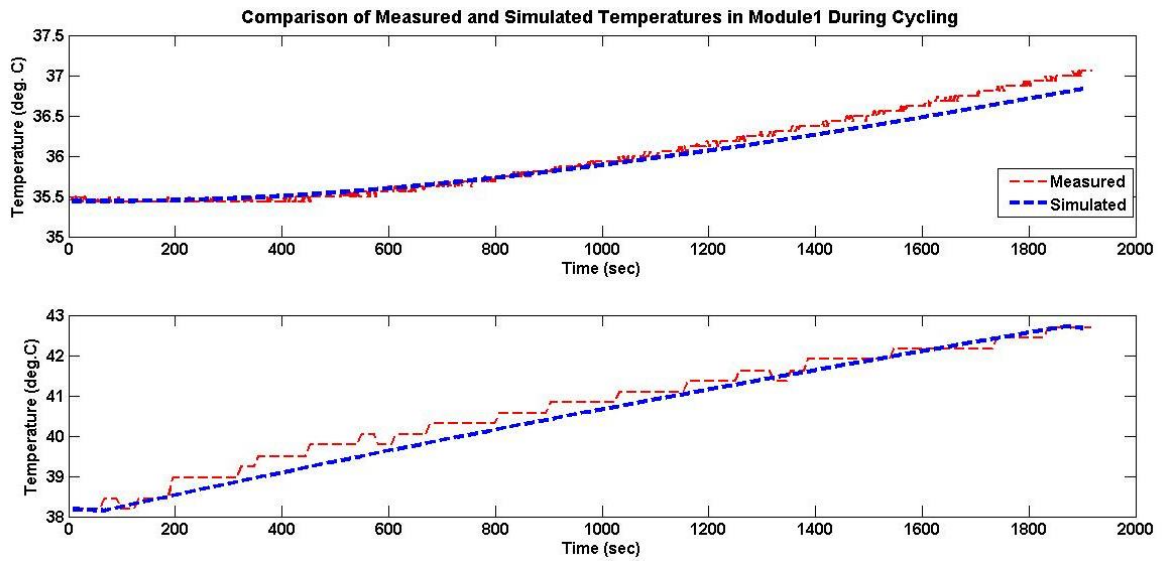


Figure 70. Comparison of measured and simulated temperature response at Module 1 during Pack Cycling

It is clear from both graphs that the model is able to simulate transient temperature responses at all critical locations of the battery system with a high degree of fidelity, while maintaining low computational complexity. This model can thus form the basis of a large number of trade-off studies and development of advanced thermal management systems.

This model is currently being used by the project stake-holder in combination with the electrical model described earlier, to execute high-fidelity, full-vehicle and powertrain simulations. The model provides a basis for the project stake-holder to quickly perform trade-off studies on much needed changes to the cooling-system configuration. It has also enabled the development of an active thermal management controller, as opposed to the passive one currently deployed on the system.

Chapter 6. Conclusions

As stated in the introduction, the primary goals of the project were to develop empirically based, high-fidelity models of the electrical and thermal behavior of transit-bus battery-system. All the work done under the two verticals of electrical and thermal models, is ultimately unified into a single model that jointly simulates the battery-system in its entirety. This unified model is shown in Figure 71.

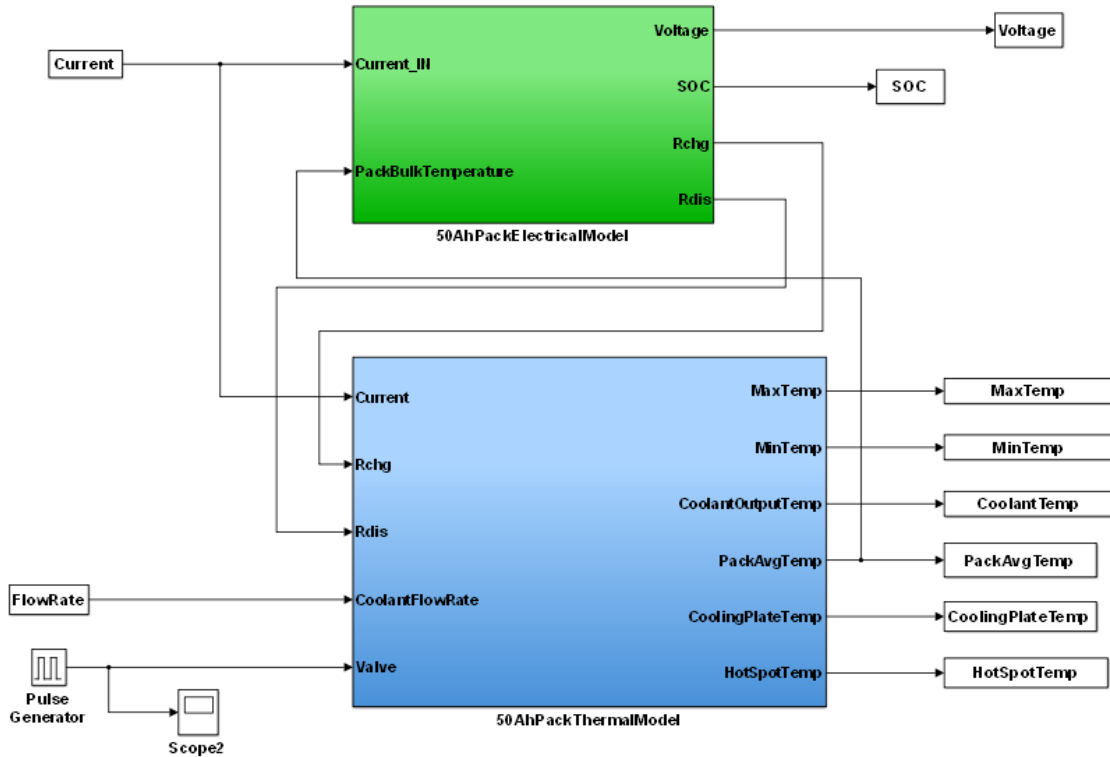


Figure 71. Unified electrical and thermal model used in full-vehicle simulations, control-design, etc.

This unified model is currently being used by the developers of the plug-in electric transit bus to perform system-level drive-cycle simulations. Moreover, it is being used to simulate the bus' performance under extreme operating condition, and to design control strategies for the same. It is also being used for trade-off studies on different aspects of the system's thermal controls.

Figure 72 and Figure 73 show results from a demo simulation. The battery-system is subjected to a HPPC load profile for approximately 2.5 h. The system is assumed to be at a steady-state uniform initial temperature of 30 °C. As a demo of a cooling-system trade-off study, the battery-system is cooled by initially circulating the coolant through a chiller operating at a low-end temperature of -6 °C for the first 25 min. The temperatures drop quickly during the initial phase when the cooling system is active, and then gradually start to rise. The temperature trajectories

at the cooling-plate and module-terminals, as well as the voltage response, are all as expected. This demo simply exemplifies the utility of this model in systems development and control design.

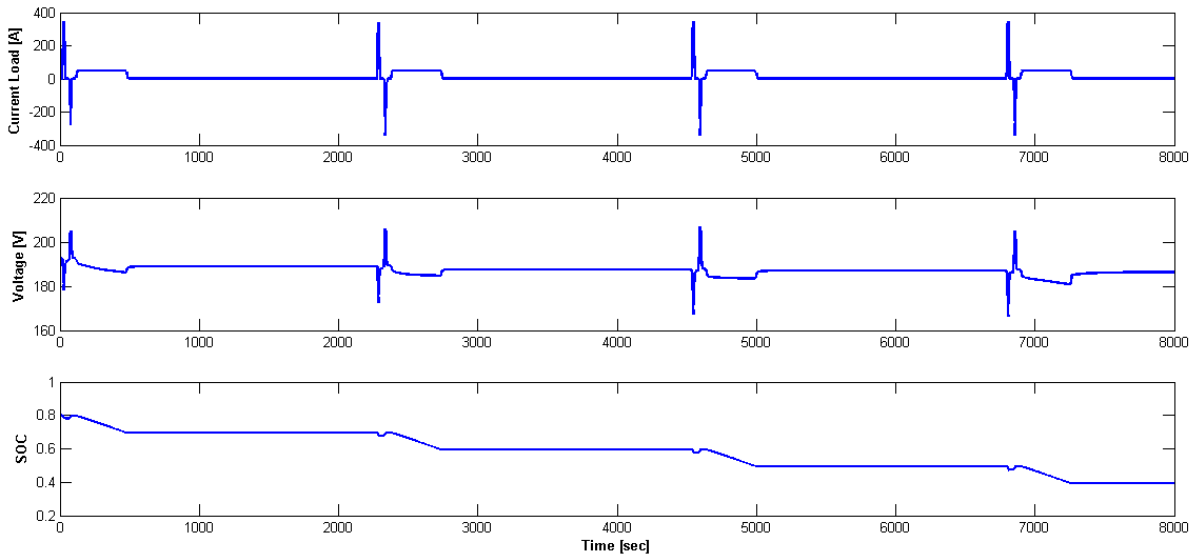


Figure 72. voltage and SOC results from a simulated HPPC test on the Unified Model

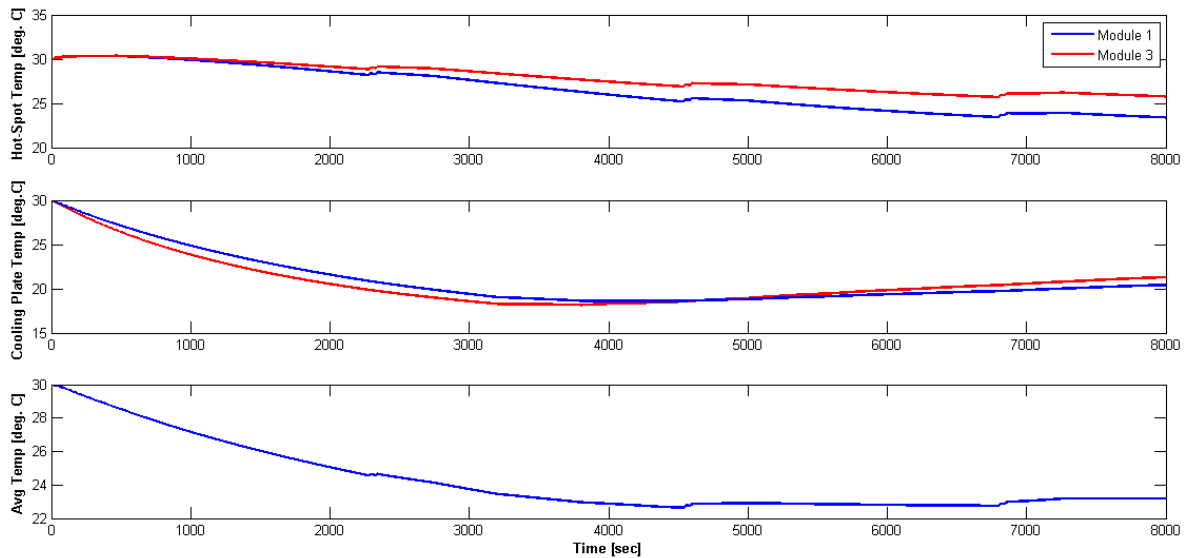


Figure 73. temperatures of Module 1 and Module 3 from a simulated HPPC test using the Unified Model

In conclusions, I hope to have left the reader with a concrete understanding of the entire process of developing high-fidelity simulation models of automotive battery-systems, and their utility in system-development and control-design.

Bibliography

- [1] M. Doyle, T. Fuller and J. Newman, "Modeling of galvanostatic charge and discharge of the lithium/polymer/insertion cell," *Journal of the Electrochemical Society*, pp. 1526 - 1533, 1993.
- [2] R. X. a. J. F. Hongwen He, "Evaluation of Lithium-Ion Battery Equivalent Circuit Models," *Energies*, pp. 582-598, 2011.
- [3] T. Huria, M. Ceraolo, J. Gazzarri and R. Jackey, "High Fidelity Electrical Model With Thermal Dependence for Characterization and Simulation of High Power Lithium Battery Cells," in *Electric Vehicle Conference, IEEE International*, 2012.
- [4] T. Huria, M. Ceraolo, J. Gazzarri and R. Jackey, "Simplified Extended Kalman Filter Observer for SOC Estimation of Commercial Power-Oriented LFP Lithium Battery Cells," *SAE Technical Paper*, 2013.
- [5] R. Jackey, G. Plett and M. Klein, "Parameterization of Battery Simulation Models Using Numerical Optimization Methods," in *SAE Technical Paper - SAE World Congress*, 2009.
- [6] R. Jackey, M. Saginaw, P. Sanghvi, J. Gazzari, T. Huria and M. Ceraolo, "Battery Model Parameter Estimation Using a Layered Technique: An Example Using Lithium Iron Phosphate Cell," *SAE Technical Paper*, 2013.
- [7] B. Saha and K. Goebel, "Modeling Li-ion Battery Capacity Depletion in a Particle Filtering Framework," in *Annual Conference of the Prognostics and Health Management Society*, 2009.
- [8] AeroVironment, "AV-900 Datasheet," 2009.
- [9] ESPEC North America Inc, "Panelized Walk-In temperature and Humidity Chamber Specifications," 2012.
- [10] Idaho National Laboratory, US Department of Energy, *Batter Test Manual for Plug-In Hybrid Electric Vehicles*, 2010.
- [11] The MathWorks, "Least-Squares Algorithm," 2013. [Online]. Available: <http://www.mathworks.com/help/optim/ug/least-squares-model-fitting-algorithms.html#brrzgus>.

- [12] S. Piller, M. Perrin and A. Jossen, "Methods of State of Charge Determination and their applications," *Journal of Power Sources*, 2001.
- [13] V. Pop, H. Bergveld, P. Notten and P. Regtien, "State-of-the-art of battery state-of-charge determination," *Measurement Science and Technology*, 2005.
- [14] G. Plett, "Extended Kalman Filtering for Battery management Systems of LiPB based HEV battery packs. Part3. State and Parameter Estimation," *Journal of Power Sources*, 2004.
- [15] D. Di Domenico, E. Prada and Y. Creff, "An Adaptive Strategy for Li-ion Battery SOC Estimation," in *IFAC World Congress*, Milano, Italy, 2011.
- [16] D. Simon, *Optimal State Estimation - Kalman, H-infinity, and Nonlinear Approaches*, Wiley, 2006.
- [17] Texas Instruments, "Hybrid and Electric Vehicle Solutions," 2013.
- [18] MathWorks, Inc, "n-D Look Up Tables," 2013. [Online]. Available: <http://www.mathworks.com/help/releases/R2013a/simulink/slref/ndlookuptable.html>.
- [19] MathWorks, Inc., "Software In Loop Simulations," Mathworks, Inc, 2013. [Online]. Available: <http://www.mathworks.com/help/releases/R2013a/ecoder/software-in-the-loop-sil-simulation.html>.
- [20] I. MathWorks, "Real-Time Simulations Using Real-Time Windows Target," MathWorks, Inc., 2013. [Online]. Available: <http://www.mathworks.com/help/releases/R2013a/rtwin/low-sample-rate-simulation.html>.
- [21] T. Bandhauer, S. Garimella and T. Fuller, "A Critical Review of Thermal issues in Lithium-Ion Batteries," *Journal of The Electrochemical Society*, pp. R1-R25, 2011.
- [22] M. R. Giuliano, S. Advani and A. Prasad, "Thermal Analysis and Management of Li-Titanate Batteries," *Journal of Power Sources*, vol. 196, no. 15, 2011.
- [23] K. Murashko, J. Pyrhonen and L. Laurila, "Three-Dimensional Thermal Model of Lithium Ion Battery for Hybrid Mobile Working Machines: Determination of the Model Parameters in a Pouch Cell," *IEEE Transactions on Energy Conversion*, vol. 28, no. 2, 2013.
- [24] D. Bernardi, J. Newman and E. Powlikoski, "A General Energy Balance for Battery Systems,"

Journal of Electrochemical Society, vol. 132, no. 1, 1985.

- [25] N. Nieto, L. Diaz, J. Gastelurrutia, I. Alava, F. Blanco, J. Carlos Ramos and A. Rivas, "Thermal Modeling of Large Format Lithium-Ion Cells," *Journal of the Electrochemical Society*, pp. A212-A217, 2012.
- [26] A. Rahmoun, H. Biechl and A. Rosin, "State of Charge Estimation of Li-ion Batteries Based on Equivalent Circuit Diagrams and the Application of a Kalman Filter," in *Electrical Power Quality and Supply Reliability Conference*, 2012.
- [27] X. Tang, X. Mao, J. Lin and B. Koch, "Li-ion Battery Parameter Estimation for State of Charge," in *American Control Conference*, San Francisco, CA, USA, 2011.